August 2025

THE IMPACT OF MUNICIPAL SOLID WASTE INCINERATION BOTTOM ASH ON THE RHEOLOGY OF SLAG BASED ALKALI ACTIVATED MATERIAL FOR 3D PRINTING

Shiva Preethi Sompalli

TU Delft

The Impact of Municipal Solid Waste Incineration Bottom Ash on the Rheology of Slag Based Alkali Activated Material for 3D Printing

By

Shiva Preethi Sompalli

In partial fulfilment of the requirements for the degree of Master of Science in Civil
Engineering at the Delft University of Technology
to be defended publicly on Thursday 21 August 2025

Student number:	5387302	
Project duration:	August 2023 – August 2025	
Thesis committee:	Prof. Dr. Guang Ye	Chairman
	Dr. ir. Branko Šavija	Committee member
	Dr. ir. Yuguang Yang	Committee member
	Dr. ir. Boyu Chen	Daily Supervisor

To my parents, the guardians of my dreams

Contents

List of Figures

List of Tables

Summary

The construction industry faces dual challenges of developing sustainable materials while advancing innovative manufacturing technologies. In recent years, Alkali-activated materials (AAMs) have become viable alternatives to ordinary Portland cement, offering reduced carbon emissions and the ability to incorporate industrial by-products. The increasing scarcity of traditional supplementary cementitious materials, particularly fly ash due to coal power plant closures, necessitates finding alternative precursors. Municipal solid waste incineration bottom ash (MSWI BA), a by-product of waste-to-energy processes currently landfilled in large quantities, presents an opportunity to address both material scarcity and waste management challenges.

Concurrently, 3D concrete printing technology is revolutionizing construction practices by enabling automated, formwork-free fabrication of complex geometries. However, successful implementation of this technology requires materials with precisely controlled rheological properties that balance conflicting requirements: sufficient fluidity for pumping and extrusion, yet adequate stiffness for shape retention after deposition. These rheological properties are fundamentally governed by early-age reaction kinetics, which control the rate of structural build-up and stiffening. Developing a mixture that meet these stringent printability requirements while incorporating waste materials represents a significant challenge. This research addresses this challenge by investigating the feasibility of incorporating MSWI BA as a sustainable replacement for fly ash in 3D printable alkali-activated mortars.

This study aims to investigate the impact of municipal solid waste incineration bottom ash (MSWI BA) as a sustainable alternative to fly ash on the printability and early-age behaviour of slag-based alkali-activated materials for 3D printing applications. To achieve this aim, the research followed a systematic three-phase approach: mix development and optimization, investigation of MSWI BA effects on rheology and early-age reaction kinetics, and environmental impact assessment through life cycle analysis.

The first phase involved development of two 3D printable mortar through systematic optimization for printability. Initially, a reference mix was established using blast furnace slag (BFS) and fly ash (FA) as precursors. Subsequently, a target mix was developed where fly ash was replaced with MSWI BA while maintaining comparable printability performance. The optimization process evaluated buildability through slump tests, flowability through slump flow measurements, extrudability through mini-extrusion tests, setting time through Vicat testing, and mechanical strength development through compressive and flexural tests.

The optimized reference mix composition comprised 80% BFS and 20% FA with a water-to-binder ratio of 0.38, alkali content (Na_2O/b) of 5%, activator modulus (SiO_2/Na_2O) of 0.5, and sand-to-binder ratio of 1.5. The target mix comprised 80% BFS and 20% MSWI BA, maintaining identical alkali content, activator modulus, and sand-to-binder ratio to the reference mix, with only the water-to-binder ratio increased to 0.40 to achieve comparable workability. This 5% increase in water content was necessitated by the angular morphology and significantly finer particle size of MSWI BA compared to the spherical fly ash particles.

Both formulations successfully met all printability requirements and exceeded mechanical strength targets for 3D printing applications. The BA-based mix exhibited extended initial setting time and slightly delayed early strength development. These observations suggested fundamentally different reaction kinetics that warranted deeper investigation.

In the second phase, to understand the fundamental mechanisms governing the observed behavioural differences between the two developed printable mixes, comprehensive analysis of rheological evolution and reaction kinetics was conducted. The yield stress evolution monitored via slugs test revealed that the FA-based reference mix exhibited rapid structuration with brittle discontinuity occurring at 80 minutes, while the BA-based target mix maintained plastic deformation capability throughout the 140-minute test period, confirming the extended printable window suggested by the setting time results.

Pore solution analysis and spectroscopic analysis revealed the fundamental mechanisms responsible for the distinct rheological behaviours. The BA system consistently showed lower elemental concentrations and slower consumption rates of key elements (Na, Si, Ca and Mg) in the pore solution, indicating reduced precursor dissolution and slower reaction kinetics. This was attributed to both the dilution effect from higher water content and, more significantly, the release of heavy metals (such as Cr, Zn and Pb) from MSWI BA that form hydroxide precipitates on slag particle surfaces, hindering slag dissolution. Fourier Transform Infrared Spectroscopy (FTIR) provided complementary evidence of slower reaction kinetics, showing that the BA system maintained persistent low-polymerized silicate oligomers throughout the test period, while the FA-based reference system underwent rapid polymerization. These negatively charged oligomers sustained electrostatic repulsion between particles, delaying the formation of a percolated network and extending the printability window.

In the third phase, the environmental impact assessment through life cycle assessment (LCA) demonstrated that both AAM formulations achieved approximately 68% reduction in shadow costs compared to ordinary Portland cement mortar. The BA-based mix showed equivalent environmental performance to the FA-based reference, with MSWI BA contributing less than 5% to the total environmental impact. This negligible burden, combined with landfill diversion benefits, strongly supports MSWI BA utilization.

This research successfully demonstrates that MSWI BA can effectively replace fly ash at 20% of total binder content in 3D printable slag-based alkali-activated mortars. The key achievement is that while MSWI BA incorporation slows reaction kinetics, this characteristic provides operational advantages through extended printable window without significantly compromising on buildability or final mechanical performance. The slower kinetics maintain electrostatic stabilization for longer periods, delaying rheological transitions that limit printing operations. This extended printable window is particularly beneficial for large-scale 3D printing applications where longer processing times enhance operational flexibility.

The successful development of MSWI BA-based printable mortars advances both sustainability objectives and additive manufacturing capabilities. By valorising a waste material while maintaining performance requirements, this research contributes to circular economy principles in construction. The extended printable window offered by BA incorporation particularly benefits large-scale 3D printing operations where longer processing times are desirable. These findings provide a foundation for expanding the use of waste-derived materials in advanced construction technologies, addressing material scarcity while reducing environmental impact.

Acknowledgements

I would like to express my sincere gratitude to everyone who has supported, guided, and encouraged me throughout the course of my thesis and my master's journey.

This work was supported by funding received from the European Union's Horizon Europe research and innovation programme under grant agreement No 101058162 (AshCycle).

First and foremost, I extend my heartfelt thanks to Prof. Dr. Guang Ye for serving as chairman of my thesis committee. His valuable guidance, expertise, and insightful perspectives have significantly enriched the quality of this work. I am also grateful to my committee members, Dr. ir. Branko Šavija and Dr. ir. Yuguang Yang, for their time, insightful feedback, diverse viewpoints, and expert guidance. I truly appreciate their commitment and willingness to support my work throughout this process.

I owe special thanks to my daily supervisor, Dr. ir. Boyu Chen, for her exceptional guidance and support throughout this research. Our thoughtful discussions have been instrumental in developing my ideas and overcoming challenges. Her remarkable patience, combined with her willingness to assist me at every step of the way, has been invaluable. I am deeply grateful for her dedication and mentorship, which have been essential to bringing this thesis to completion.

The successful execution of the experimental phase of this research was made possible by the technical expertise of Maiko van Leeuwen, John van den Berg, Ton Blom, Arjan Thijssen, Ir. ing. Michèle van Aggelen, and Ing. Marco Poot. Their guidance in the laboratory and assistance in overcoming practical challenges were instrumental to this project. I would also like to extend my sincere thanks to Farnaz Aghaneyk for her support in this research.

Finally, my deepest gratitude belongs to my parents, family, and friends for their constant love and unwavering support. Their encouragement through all the ups and downs, and their belief in me, have been my greatest source of strength throughout this academic journey. Completing this thesis has been both a challenging and rewarding experience, and I am sincerely thankful to all who have contributed to making it possible.

Shiva Preethi Sompalli
Delft, August 2025

List of Abbreviations

3D	Three-Dimensional
3DCP	Three-Dimensional Concrete Printing
AAM	Alkali-Activated Material
ATR-FTIR	Attenuated Total Reflectance – Fourier Transform Infrared Spectroscopy
BA	Bottom Ash
BFS	Blast Furnace Slag
C-A-S-H	Calcium-Aluminosilicate-Hydrate
C-N-A-S-H	Calcium-Sodium-Aluminosilicate-Hydrate
CC	Contour Crafting
ECI	Environmental Cost Indicator
EPD	Environmental Product Declaration
ESI	Effective Saturation Index
FA	Fly Ash
FTIR	Fourier Transform Infrared Spectroscopy
GEMS	Gibbs Energy Minimization Selektor
GGBS	Ground Granulated Blast Furnace Slag
H-B	Herschel–Bulkley
ICP-OES	Inductively Coupled Plasma Optical Emission Spectroscopy
LCA	Life Cycle Assessment
LDH	Layered Double Hydroxides
MSWI	Municipal Solid Waste Incineration
MSWI BA	Municipal Solid Waste Incineration Bottom Ash
N-A-S-H	Sodium-Aluminosilicate-Hydrate
N-C-A-S-H	Sodium-Calcium-Aluminosilicate-Hydrate
OPC	Ordinary Portland Cement
PSD	Particle Size Distribution
SC3DP	Shotcrete-Based Three-Dimensional Printing
SCM	Supplementary Cementitious Materials
SDC	Smart Dynamic Casting
SEM	Scanning Electron Microscopy
SI	Saturation Index

1

Introduction

1.1 Research Background

The construction industry is at a critical juncture where sustainability has become a primary concern. The construction industry faces sustainability challenges due to energy-intensive traditional methods and significant waste generation. Conventional concrete, made from ordinary Portland cement (OPC), is highly energy-intensive and carbon-intensive. Additionally, the industry generates significant waste, especially from formwork, exacerbating its environmental impact and highlighting the need for more sustainable practices [1].

Additive manufacturing, also referred to as three-dimensional (3D) printing, presents viable pathway for addressing these challenges. 3D printing in construction provides high efficiency, reduced labour costs, and less waste compared to traditional methods. The conventional process, which involves the shaping of concrete with formworks, is costly. These formwork expenses can constitute a major portion, often exceeding half of construction budgets, with non-standard designs demanding close to 80-90% [2]. In contrast, 3D printing eliminates the need for formwork entirely, significantly cutting these costs. Additionally, it reduces labour costs by 50-80% and on-site material wastage by 30-60% [2], [3], [4], [5]. By allowing for precise material application, this technology minimizes excess use of resources, thereby reducing the overall environmental footprint of construction projects [6].

Moreover, 3D concrete printing enables freeform building, offering architects greater geometric freedom without high costs. This innovation enhances productivity and speeds up construction timelines, leading to further cost savings [7]. However, successful implementation of 3D printing technology requires materials with specific rheological properties that balance conflicting requirements: sufficient fluidity for pumping and extrusion, yet adequate yield stress for shape retention and buildability. Understanding the fundamental mechanisms governing these rheological properties, particularly during the critical early-age period, is essential for optimizing printable material formulations [1], [3].

Global waste production is anticipated to approach 3.40 billion tons by the year 2050, outpacing population growth [8] and creating significant environmental challenges. In 2016 alone, solid waste management generated 1.6 billion tons of CO_2-equivalent emissions, accounting for about 5% of global emissions [8]. A major contributor to these emissions is cement production, which is responsible for about 8% of global CO_2 emissions [5]. Addressing this, replacing Portland cement with alkali-activated materials (AAM) could reduce CO_2 emissions by 40-80% [9].

Currently, Industrial by-products such as blast furnace slag and coal fly ash are predominantly used as supplementary cementitious materials (SCM) and also in alkali-activated materials (AAM) as precursors. However, their availability is projected to decline over the next three decades, necessitating the exploration of alternative industrial by-products for a low-carbon transition in the cement industry [9]. Therefore, reusing Municipal Solid Waste Incineration Bottom Ash (MSWI BA) as a precursor in AAM can further mitigate environmental burdens associated with waste disposal and enhance the sustainability of construction materials [10].

However, the incorporation of alternative precursors like MSWI BA introduces complexities in material behaviour that must be thoroughly understood. The different particle morphology, chemical composition, and reactivity of MSWI BA compared to conventional fly ash can significantly influence the early-age reaction kinetics and rheological evolution of alkali-activated systems, ultimately affecting their printability window and performance.

This research emphasizes understanding the fundamental mechanisms by which MSWI BA influences the early-age behaviour of slag-based alkali-activated materials for 3D printing applications. By investigating the interplay between reaction kinetics and rheological evolution, this study seeks to establish the scientific basis for utilizing MSWI BA as a sustainable alternative to fly ash while maintaining the critical performance requirements for 3D printing technology. The integration of waste valorisation with advanced manufacturing techniques represents a synergistic approach to addressing both environmental challenges and the evolving needs of the construction industry.

1.2 Research Gap

Despite growing interest in sustainable construction materials and additive manufacturing technologies, several critical knowledge gaps exist regarding the utilization of MSWI bottom ash in 3D printable alkali-activated materials:

- **Limited understanding of MSWI bottom ash behaviour in 3D printable systems.** While MSWI bottom ash has been studied as a supplementary cementitious material in conventional applications, its specific influence on the rheological properties required for 3D printing remains limited. The fundamental mechanisms governing how MSWI bottom ash affects buildability, flowability, and extrudability in alkali-activated systems need comprehensive investigation to enable its practical implementation in additive manufacturing.

- **Insufficient knowledge of early-age reaction kinetics and microstructural evolution.** The critical printability window in 3D concrete printing is determined by early-age material behaviour, yet the influence of MSWI bottom ash on reaction kinetics during this crucial period is not well understood. The interplay between precursor dissolution, gel formation, and rheological structuration in MSWI BA-containing systems requires detailed characterization to optimize printing parameters and ensure consistent performance.

- **Lack of established correlations between chemical reactions and rheological evolution.** The relationship between early age reaction kinetics, and rheology evolution in MSWI BA-based alkali-activated materials has not been systematically studied. Understanding these fundamental correlations is essential for predicting and controlling the printability, which directly impacts the feasibility of 3D printing operations.

1.3 Research Aim and Objectives

The aim of this research is to investigate the impact of municipal solid waste incineration bottom ash as a sustainable alternative to fly ash on the printability and early-age behaviour of slag-based alkali-activated materials for 3D printing applications.

The following are the objectives of this research:

1. To develop a reference 3D printable alkali-activated mortar blend comprising fly ash (FA) and blast furnace slag (BFS) without admixtures, and to evaluate MSWI BA as a replacement for FA that meets printability requirements.
2. To understand the effects of MSWI BA on rheology and early-age reaction kinetics of the developed 3D printable slag-based alkali-activated mortars.
3. To evaluate the environmental impact of MSWI BA incorporation in 3D printable slag-based alkali-activated mortars through life cycle assessment (LCA).

1.4 Research Scope

The research scope is defined to ensure that the results are consistent and reliable. The following points outline the scope of the research:

- Only extrusion-based 3D concrete printing method is used.
- Only mortar samples are studied, limiting the investigation to the mortar level.
- The maximum aggregate (sand) size used in the mortar mix is limited to 2 mm to accommodate the restrictions imposed by the 3D printing setup.
- No admixtures are used in the sample preparation to isolate the effects of MSWI BA.
- Sand-to-binder ratio was fixed at 1.5 using CEN standard sand according to EN 196-1 for all mortar-level investigations.
- The investigation focuses on early-age properties (0-140 minutes) relevant to printing operations, though mechanical properties are evaluated up to 28 days.
- The mortar samples are sealed and cured in a fog room at 20°C and 99% relative humidity before measurements are taken.

1.5 Research Methodology

The methodology for this research is divided into three distinct stages, each with specific objectives and tasks to build progressive understanding of the impact of MSWI BA as a sustainable alternative to fly ash on the printability of slag-based alkali-activated materials, as shown in the Figure *1.1*.

Stage 1: Development of 3D Printable AAM with MSWI BA

This stage focuses on the systematic development of 3D printable alkali-activated mortar mixture. The primary objective is to establish mix design that incorporates MSWI BA as a replacement for fly ash while satisfying multiple printability criteria including buildability, flowability, extrudability, open-time and mechanical performance.

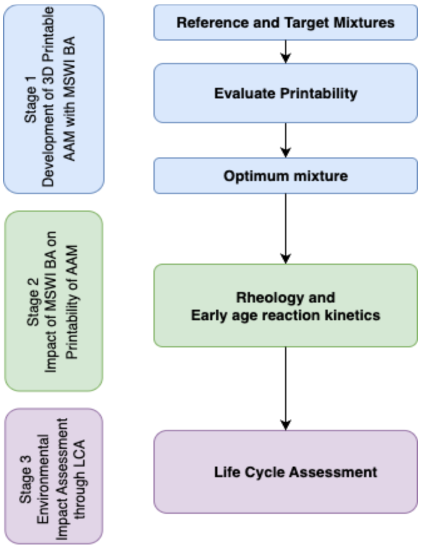

Figure 1.1 Research Methodology.

Stage 2: Impact of MSWI BA on Printability of AAM

This stage investigates the underlying physicochemical mechanisms through integrated analysis of rheological behaviour and early-age reaction kinetics, revealing how MSWI BA modifies the fundamental processes governing printability.

Stage 3: Environmental Impact Assessment through LCA

This stage evaluates the environmental impacts of utilizing MSWI BA in 3D printable alkali-activated materials through comprehensive life cycle assessment. The analysis determines the environmental implications of replacing fly ash with MSWI BA by quantifying and comparing across multiple impact categories.

2

Literature Review

2.1 Introduction

This chapter provides a comprehensive overview of the different 3D printing technologies used in construction, particularly focusing on the classification of these techniques based on their formwork requirements. This chapter also highlights the advantages and limitations of some of the existing 3D printing techniques. It delves into the behaviour of concrete in extrusion-based 3D printing, discussing the critical rheological properties required for successful printing.

Furthermore, the chapter discusses the materials used in extrusion-based 3D concrete printing, focusing on alkali-activated materials (AAMs) such as Ground Granulated Blast Furnace Slag (GGBFS), Fly Ash (FA), and Municipal Solid Waste Incinerated Bottom Ash (MSWI BA). These materials, known for their lower environmental impact compared to traditional Portland cement, are examined in terms of their chemical composition, reactivity, and suitability for 3D printing. The reaction mechanisms of these AAMs are also explored, providing insights into how these materials interact during the printing process to form durable, sustainable structures.

2.2 Introduction to 3D Printing

3D concrete printing (3DCP) refers to the additive manufacturing process using cement-based materials to create structures layer by layer. This innovative construction technique offers several advantages, including enhanced design flexibility, reduced material waste, shorter construction times, lower labour requirements, increased safety on-site, and significant cost savings [2].

The concept of additive manufacturing, including 3D printing, dates back to the mid-1980s with the initial patents focusing on polymer-based materials. Over time, this technology has evolved to encompass a broader range of materials and expanded to industries such as aerospace, automotive, biomedical, consumer, and food [11]. The potential to apply 3D printing in the construction sector, particularly with concrete, was first explored by Joseph Pegna in 1997. Further advancements were made in the early 2000s by Professor B. Khoshnevis from the University of Southern California, who significantly contributed to the development of 3D concrete printing technologies [12].

2.2.1 Classification of Printing Technologies

Various terms are used to describe 3D printing, including additive fabrication, computer-aided fabrication, digital fabrication, and rapid prototyping [12]. There are several types of 3D printing technologies currently in use, particularly in the construction industry [7]. The primary types of concrete printing techniques suitable for construction are shown below, categorized simply based on their formwork requirements. The Figure *2.1* provides a comprehensive classification of digital and additive fabrication methods for cement materials, specifically focusing on 3D concrete printing (3DCP). The techniques are divided into two main categories based on the need for formwork as: "No Formworks" and "Non-Conventional Formworks."

1. **No Formworks:** This category includes methods that do not require traditional formwork. They are extrusion-based printing, selective binding particle bed 3D printing and shotcrete 3D printing.

a. **Extrusion-based Printing:** Extrusion-based concrete printing is based on the fused deposition modelling for polymers, which is the most common form of 3DCP [12], involving the deposition of concrete in a layer-by-layer fashion without the need for formwork or vibration processes [3]. There are two methods that come under extrusion-based 3D printing, they are contour crafting and concrete printing.

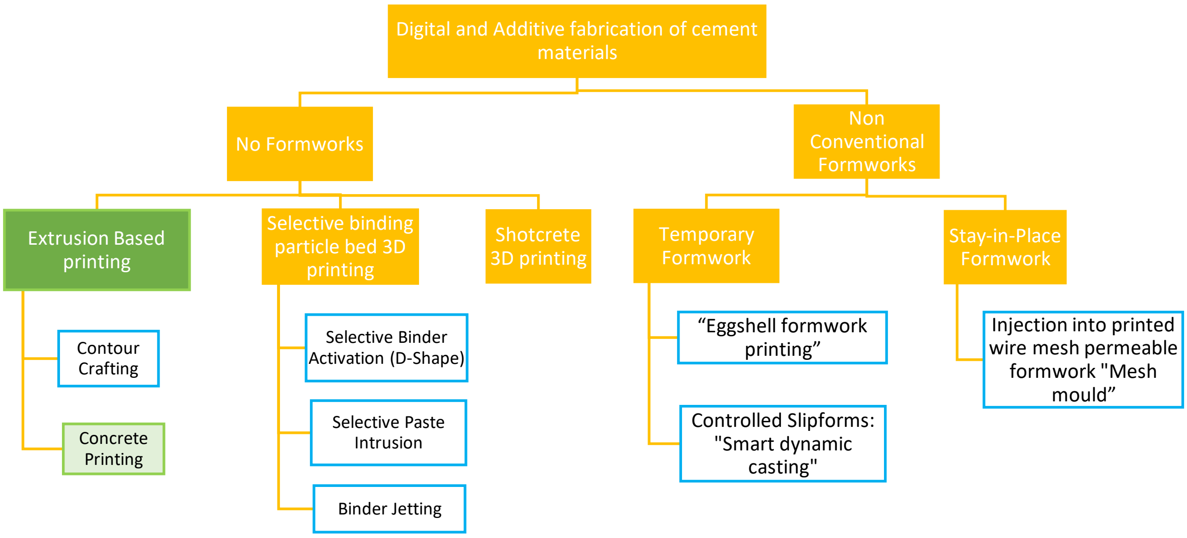

Figure 2.1 Classification of additive manufacturing techniques.

i. **Contour Crafting**: Contour Crafting (CC) is a type of the extrusion-based 3D printing. The printer initially creates the outer edges of the component to establish a closed section, into which concrete is subsequently poured for further construction (as shown in Figure *2.2*). Contour Crafting allows for the use of different materials within the same component [3].

ii. **Concrete Printing**: Concrete Printing operates on similar principles of extrusion and deposition like CC but differs in execution. Instead of first printing the outside edge, the printer constructs the entire geometry of each layer simultaneously (as shown in Figure *2.3*) [3].

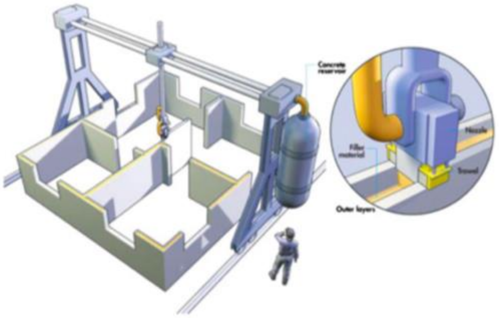

Figure 2.2 Construction of a single-family home using contour crafting [12].

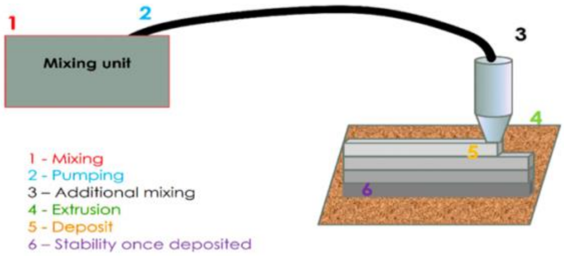

Figure 2.3 Concrete printing process [12].

b. Selective binding particle bed 3D printing:

This 3D printing approach uses ink deposition on powder beds or aggregate layers. The ink can contain various components such as water, cement paste, additives, or organic materials, depending on the specific method employed [11]. This category includes three methods (shown in Figure *2.4*):

i. **Selective cement activation:** Also known as the powder-based D-Shape technique, this method uses a powder bed containing cement or mineral binders combined with aggregates [12]. These aggregates can range from fine sand to coarse gravel based on the printing resolution. The activation is done by injecting a solution made up of water and admixtures [12].

ii. **Selective paste intrusion**: In the second method, selective paste intrusion, the suspension made from mineral binder or cement paste is directly injected on to a bed of aggregates[12]. The Selective cement activation and selective paste intrusion are sometimes collectively referred as powder-based technology [7].

iii. **Injection of the binder:** This method combines elements of the previous techniques, which involves applying the binder directly to a layer of sand and an activator [12]. Typically, a liquid binder, usually a resin, is applied to a particle bed that also contains a hardener [12]. The particle beds used in this method are finer compared to those used in the other techniques [12].

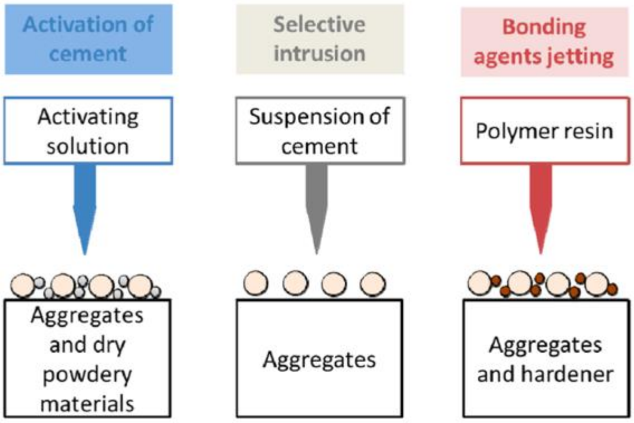

Figure 2.4 Methods of selective binding particle bed 3D printing [12].

c. Shotcrete 3D Printing:

The shotcrete-based 3D printing (SC3DP) approach was introduced in the year 2017 by the Digital Building Fabrication Laboratory at Braunschweig University of Technology, offering an alternative to extrusion-based methods [13], [14]. This method replaces extrusion with shotcrete for depositing concrete layers. In SC3DP, concrete is delivered through a hose and sprayed with high-pressure compressed air from the nozzle tip onto a surface to build up layers and form structures as shown in Figure 2.5 [14].

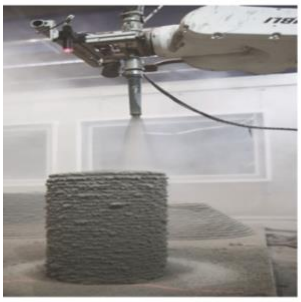

Figure 2.5 Shotcrete 3D printing [14].

2. **Non-Conventional Formworks:** This category involves methods that utilize alternative forms of formwork.

a. **Temporary Formwork**: This involves the use of formwork that is removed after the concrete has cured.

i. **Eggshell formwork printing:** The "Eggshell" fabrication process allows for the efficient production of nonstandard concrete structures. This method uses 3D-printed concrete formwork to enhance geometric flexibility. By continuously casting fast-hardening concrete, the lateral pressure from the fresh material is significantly reduced. This reduction allows for the use of a thin 1.5-mm thermoplastic shell as formwork without the need for additional support. The shell can be easily removed after the concrete element is completed due to its thermoplastic properties as shown in Figure *2.6* [15].

ii. **Controlled Slipforms - Smart dynamic casting:** Smart Dynamic Casting (SDC) is an innovative digital construction technique developed at ETH Zurich in the year 2010, drawing inspiration from the traditional slip-forming method long used for creating large vertical structures such as water towers and bridge piers [12], [16]. In this automated process, a dynamic formwork, which is much smaller than the final structure, is continuously moved and filled with concrete. Fresh concrete is poured from the top of this small dynamic formwork and exits from the bottom in a partially hardened state (as shown in Figure *2.7*). This state provides sufficient strength for the concrete to support its self-weight and the load above it, while still being soft enough to be moulded into the desired shape [17].

Figure 2.6 Construction of concrete column with three branches using the eggshell fabrication process [15].

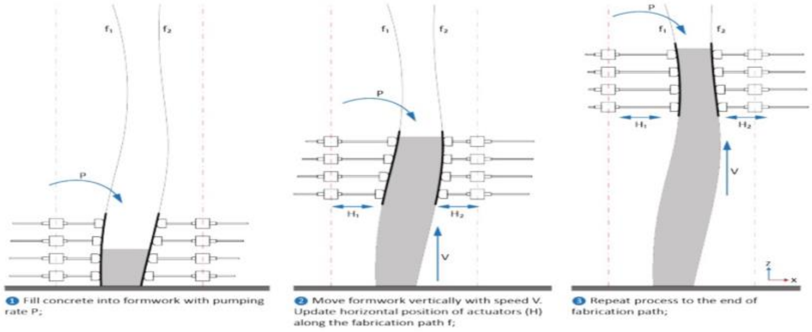

Figure 2.7 Schematic of SDC control system fabrication parameters: concrete pumping rate into formwork (P), vertical formwork lifting speed (V), and horizontal actuator positioning along fabrication paths (H) [18].

b. **Stay-in-Place Formwork**: This includes formwork that remains as a part of the finished structure, providing additional support or insulation.

i. **Injection into printed wire mesh castings (Mesh Mould):** The Mesh Mould project at ETH Zurich, initiated in 2012, features another innovative technique that involves utilizing a welding robot [12], [19]. This method has recently evolved to enable 3D printing of functional stay-in-place formwork [17]. The welding robot continuously bends and welds Ø4.5 or Ø6.0 mm conventional rebars [19] in vertical layers, creating a steel wire mesh. This robotically fabricated mesh serves as both the permeable formwork and the structural reinforcement for the concrete as shown in Figure *2.8* [17].

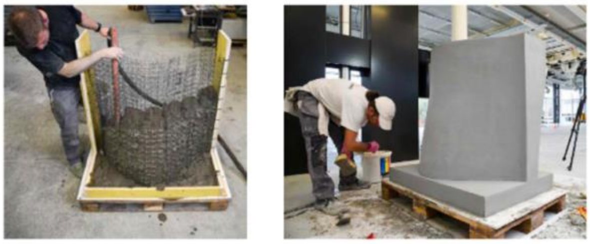

Figure 2.8 Concreting process of a mesh mould wall [19]

2.2.2 Comparison of 3D Printing Techniques Without Formwork

A Comparison is drawn among different techniques that do not require formwork. Those include the two extrusion-based 3D printing methods, contour crafting and concrete printing, as well as the powder-based D-Shape technique and shotcrete 3D printing. Each of these techniques has its own challenges and limitations with respect to process, speed, scale of construction, strength, performance requirements of materials, etc.

In Contour Crafting (CC), the printed layers can either be left with a layer-by-layer texture or smoothed using two trowels attached to the printhead on both sides. Unlike CC, Concrete Printing does not use finishing trowels, leaving the layered surface as is. The concrete printing method typically operates at a slower pace and is often more suitable for printing off-site. Contour Crafting allows switching of printing materials but has low construction speed relative to concrete printing. However, both of these extrusion-based methods can have low bond strength between layers [2], [3].

Powder-based D-shape printing uses a spreading process to achieve high strength but suffers from lower resolution, requires massive powder materials, and has a limited scope of usable materials. Shotcrete-based 3D Printing (SC3DP) uses a shotcreting process to form layers, overcoming the weak interlayer bonding and construction difficulties of extrusion-based methods. It can easily build vertical and overhanging structures with reinforcement meshes but faces challenges like material loss due to rebound and dust generation. The SC3DP needs complex mixture design for pumpability and shootability, which can be more challenging to achieve than extrusion-based 3D printable mixtures [14].

The Table *2.1* highlights the advantages and limitations of the existing 3D printing techniques without the requirement of formwork.

Table 2.1 Comparison of 3D printing techniques without formwork [3], [14].

Methods	**Contour Crafting**	**Concrete Printing**	**D-Shape**	**Shotcrete 3D printing**
Process	Extruding	Extruding	Spreading	Pneumatic
Speed	Low	High	Medium	High
Dimensions	Large-Scale	Large-Scale	Medium Size	Large-scale
Advantages	Trowel-finished smooth surfaces [3]. Embedded conduit capability [3]. Possibility to switch printing materials [3].	High strength and building speed.	High strength	High strength and building speed. Better interlayer bond. Vertical elements and overhangs can also be built. Real-size reinforcement (mesh form) can be used [14].
Disadvantages	Low construction speed due to trowelling and low bond strength between layers caused by intervals [3].	High performance requirements for 3D printed concrete such as setting and hardening time [3].	Low resolution. High amount of powder required. Excess powder removal needed. Limited material options for powder-bed systems [3].	Lower resolution and sometimes requires formwork. Challenging mixture design. Fibres and coarse aggregates not been attempted for SC3DP. Material waste from rebound. High dust levels on the construction site [14].

2.3 Concrete Behaviour for Application in Extrusion based 3D Concrete Printing

The field of physics that is concerned with the material deformation and flow behaviour under applied stress is called Rheology [2]. This discipline focuses on the relationship between shear stress, shear rate and time [20]. The rheological characteristics of materials are determined by the relationship between shear stress and shear rate, known as the flow curve [20]. These flow curves vary significantly among different materials, with some exhibiting linear relationships while others show more complex non-linear behaviour. To understand these diverse material behaviours, researchers have developed various rheological models that describe how materials flow under different stress conditions [20].

In concrete rheology, key models include the Bingham, Herschel-Bulkley (H-B), modified Bingham, and thixotropic models [21]. The Bingham model approximates a linear relationship between shear stress and shear strain rate but requires a high enough shear strain rate and does not account for shear-thickening behaviour. To address this, the Herschel-Bulkley model (H-B model) was introduced, which can describe both shear-thickening and shear-thinning behaviour. The modified Bingham model combines features of both the Bingham and H-B models, providing more consistent results for non-linear rheological behaviour [21].

While the H-B and modified Bingham models offer advantages, they are more complex, making the Bingham model preferred for its simplicity. However, the H-B and modified Bingham models are used in cases where the Bingham model is insufficient. Another important model is Roussel's thixotropy model, which measures the flocculation rate, aiding in the development of modern concrete like self-compacting concrete [21].

Concrete, a fundamental material in construction, exhibits unique properties in its fresh and hardened states. In its fresh state, concrete behaves as a non-Newtonian fluid, meaning it can act as a solid under certain conditions and as a liquid under others. Specifically, concrete shows solid-like behaviour when the applied shear stress is below a certain threshold, known as the critical yield stress. Conversely it transitions to liquid-like behaviour, when the shear stress exceeds this critical yield stress. The resistance to flow, known as viscosity, is a key characteristic of fresh concrete. Concrete's behaviour is thixotropic, meaning it exhibits a time-dependent change in viscosity; it flows when shear stress is applied and regains its structure when the stress is removed [22] [6].

Newtonian fluids, named after Sir Isaac Newton, have a constant viscosity and follow a linear relationship between shear stress and shear rate, like water and oil [23]. In contrast, non-Newtonian fluids have a viscosity that changes with applied stress, showing a non-linear relationship [24]. These non-Newtonian fluids can behave in two distinct ways depending on how their viscosity changes with shear rate. In shear-thinning fluids, viscosity decreases as shear rate increases. Conversely, the shear-thickening fluids experience an increase in viscosity when shear rate increases.

The Bingham model is commonly used to describe the rheological behaviour of non-Newtonian fluids like concrete [20], [25]. This model is characterized by two fundamental parameters. The first is yield stress, which is the minimum stress required to initiate flow [6], [25]. The second is plastic viscosity, which represents the slope of the stress versus strain rate curve beyond the yield stress [6], [25]. Unlike Newtonian fluids, Bingham fluids don't start flowing until a certain yield stress is applied. Once this stress is reached, they flow similarly to Newtonian fluids, with a linear relationship between shear stress and shear rate [23]. The Bingham model provides a framework to understand and predict these behaviours [6], [25] and can be represented as [21]:

$$\tau = \tau_0 + \dot{\mu}\gamma$$

where the τ is shear stress (Pa), τ_0 is yield stress (Pa), $\gamma^{\cdot}$ is shear strain rate (s^{-1}) and μ is plastic viscosity ($Pa \cdot s$).

For non-linear behaviour, the Herschel-Bulkley model provides better representation [21]:

$$\tau = \tau_0 + a\gamma^{\cdot b}$$

where a is consistency factor ($Pa \cdot s^b$) and b is the flow index (dimensionless). When b = 1, it reduces to the Bingham model; b < 1 indicates shear-thinning, and b > 1 indicates shear-thickening behaviour as shown in Figure 2.9. This model is particularly relevant for alkali-activated materials and forms the basis for the slugs test analysis employed in this study.

Below the yield stress, the mixture behaves like an elastic material and doesn't flow. Some materials that don't flow under gravity are called yield stress materials, though this depends on the duration of observation [20].

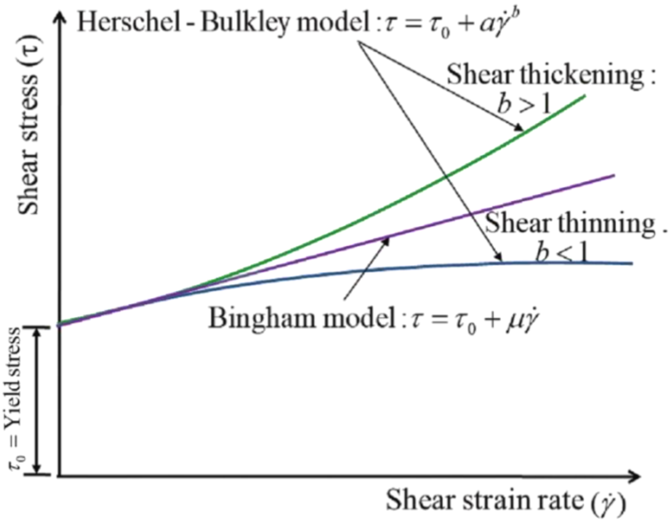

Figure 2.9 Herschel-Bulkley and Bingham models [21].

Yield stress, the critical point where the material starts to flow, comes in two forms: static and dynamic. This distinction becomes particularly important in 3D printing applications. Static yield stress is the peak shear stress required to initiate flow from a rest state, while dynamic yield stress is the stress needed to maintain this flow [21]. This behaviour, combined with the time-dependent increase in yield stress and viscosity due to hydration kinetics, makes handling fresh concrete complex [6].

The process of 3D concrete printing (3DCP) places additional demands on the fresh state properties of concrete. The broad adoption of 3D concrete printing (3DCP) is hindered by practical challenges in understanding and characterizing the fresh state properties of printable materials [22]. In additive manufacturing (AM), the term printability refers to the need for specific conditions to be fulfilled for the successful fabrication of the desired print. These conditions vary depending on the material, and in additive manufacturing of concrete (AM), the emphasis is on properties that are not as crucial in conventional concrete construction involving casting in formwork [26]. Each step in the 3D printing process corresponds to a different aspect of printability: pumpability during the delivery phase, extrudability during the extrusion phase, open time across both delivery and extrusion phases, and buildability and shape retention during the building phase [22].

For effective 3D concrete printing, concrete must exhibit a balance between pumpability, extrudability, buildability and initial setting time [26]. Pumpability refers to the mix's ability to be transported through a pipe under pressure [6]. Extrudability is the concrete's ability to pass through a nozzle without segregation, forming a continuous filament [6]. For easy pumping and extrusion, the concrete needs low plastic viscosity and low dynamic yield stress for the material flow [25]. Finally, buildability ensures that the extruded layers gain sufficient strength quickly to support subsequent layers, requiring high static yield stress and rapid setting [6]. The rheology of printable mixtures must be optimised to achieve a balance between these conflicting requirements [25] as depicted in the Figure *2.10*.

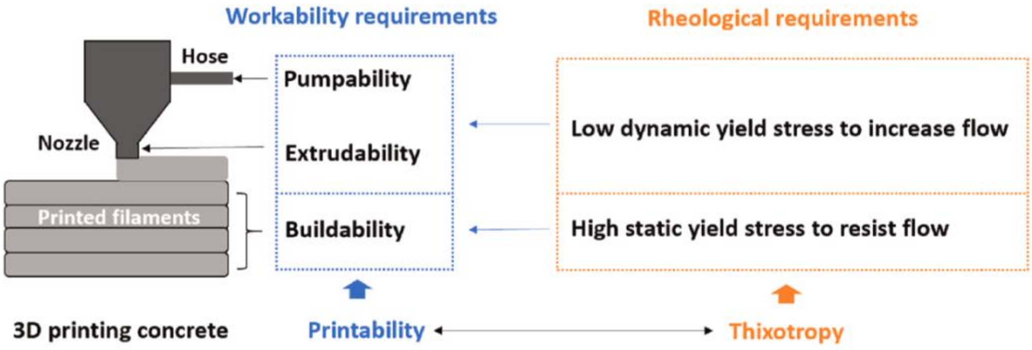

Figure 2.10 Conflicting rheological requirements in 3d concrete printing processes [25].

In conclusion, the properties of concrete in its fresh state are crucial for 3DCP. Achieving the right balance of these conflicting requirements is essential for the successful application of 3DCP, requiring a deep understanding of the material's behaviour under varying stresses and over time [6]. This research focuses on extrusion-based concrete printing, optimizing the concrete mix for flowability, extrudability, and buildability.

2.4 Theoretical Background on Micromechanical Interactions

The rheological behaviour of alkali-activated materials is governed by micromechanical interactions between the particles in the suspension. These interactions begin immediately after mixing and are influenced by both physical forces and chemical reactions. Together, they determine how a percolated particle network forms over time. This network affects key rheological properties such as yield stress and viscosity.

As depicted Figure *2.11* in the micromechanical behaviour is governed by five principal categories of forces: hydrodynamic, colloidal, Brownian, inertial, and gravitational [20]. However, in the context of 3D-printable alkali-activated materials, where particle sizes generally exceed nanometre dimensions and solid volume fractions are high, Brownian and gravitational forces play minor roles. Inertial effects typically remain negligible at low shear rates, and hydrodynamic forces are minimal at practical operational shear rates. Consequently, colloidal interactions dominate the rheological characteristics of these alkali-activated systems [20], [27].

Colloidal forces comprise van der Waals attraction, electrostatic repulsion, and steric interactions. In freshly mixed AAMs, attractive van der Waals forces, effective at short particle distances, tend to promote flocculation. Conversely, electrostatic forces can be attractive or repulsive. Repulsion arises from anions that stabilise particle suspensions [28], while attraction develops when cations (Ca^{2+}, Na^{+}) bridge between anions, promoting flocculation [29]. On the other hand, Steric hindrance involves polymer chains from superplasticisers adsorbing onto particle surfaces, creating a physical barrier that prevents particle aggregation [30]. This effect is absent here due to the lack of polymeric admixtures. Hence, van der Waals attraction and electrostatic repulsion, as highlighted in Figure *2.11*, predominantly control the early-age rheological behaviour investigated in this study.

Furthermore, rheological changes in AAMs can be both reversible and irreversible. Reversible changes are physical, arising from temporary particle rearrangements or shear-induced deflocculation, and can be recovered upon shearing. Irreversible changes stem from chemical reactions, including precursor dissolution, ion interactions, and the formation of reaction products such as C-(N)-A-S-H gels. These products create more rigid interparticle bridges, permanently enhancing the structural integrity and stiffness of the paste over time. Hence, the initial colloidal interaction-driven flocculation gradually transitions to a chemically rigidified particle network as the system evolves [20], [29].

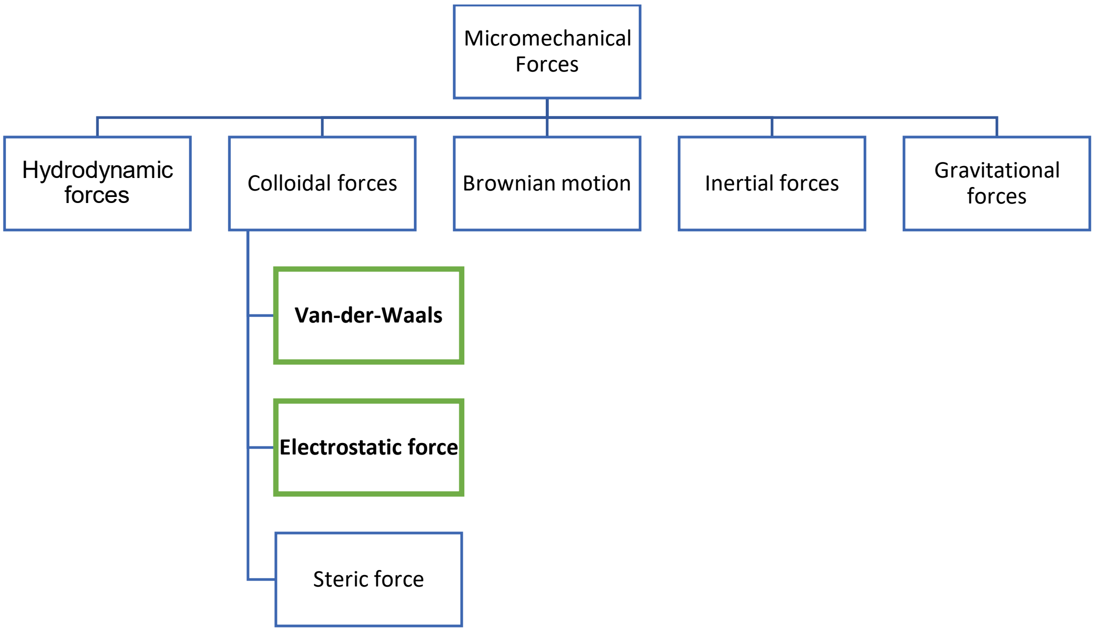

Figure 2.11 Micromechanical forces influencing the rheological behaviour of alkali-activated materials.

2.5 Materials used in Extrusion based 3D Concrete Printing

In recent years, the scope of materials used in extrusion-based 3D printing has broadened significantly, driven by the need for sustainable and high-performance alternatives in construction and manufacturing. Among these materials, alkali-activated materials (AAMs) have emerged as a promising class of binders [31], offering a lower carbon footprint compared to traditional Portland cement [31]. AAMs are produced by chemically activating aluminosilicate precursors with alkaline solutions. These materials are created by chemically activating aluminosilicate precursors, typically sourced from industrial by-products, using alkaline solutions. Ground granulated blast furnace slag (GGBFS), coal fly ash, and municipal solid waste incineration bottom ash (MSWI BA), which were once considered waste materials, are now being repurposed as valuable precursors in the development of innovative construction materials.

2.5.1 Blast Furnace Slag

Blast-Furnace Slag (BFS) is a by-product of iron manufacturing process [32], formed when iron ore, coke, and limestone are heated together in a blast furnace at around 1500°C [33]. This process produces both molten iron and molten slag. Typically, 200-400 kg of slag is generated per ton of iron [33]. Blast-Furnace Slag is primarily composed of silicates and alumina silicates of calcium and other bases, forming in a molten state alongside the iron [33]. Depending on the cooling method, BFS can be classified into three types: granulated, air-cooled, and expanded. Granulated Blast Furnace Slag (GBFS) is produced by rapidly cooling the molten slag with high-pressure water jets [33].

GGBFS is generally off-white or near white in colour and has good cementitious properties [33]. GGBFS has both glassy and crystalline phases, with the glassy phase is responsible for its cementitious properties. For effective performance, GGBFS should contain at least 80% glass content, with an ideal glass content exceeding 90%. According to BS 6699:1992, the glass content should not be less than 67% [33].

The composition of GGBFS remains fairly constant due to the consistent quality of pig iron, which is a priority for blast furnace operations [34]. BFS is primarily composed of silica (SiO_2), alumina (Al_2O_3), calcia (CaO), and magnesia (MgO), which together constitute up to 95% of its overall composition [33]. The reactivity of GGBFS tends to increase when the levels of CaO, Na_2O, and Al_2O_3 are higher, and when the levels of SiO_2, FeO, TiO_2, MnO, and MnS are lower. Usually, the reactivity of slag is also improved by increasing its fineness [34]. The slag has a higher fineness than cement but a lower specific gravity [35]. Generally, greater fineness leads to better strength development, though it's often limited by economic factors and performance constraints such as setting times and shrinkage. The specific surface area of slag typically ranges from 375 to 450 m²/kg, though this can vary by country [33].

2.5.2 Fly ash

Fly Ash (FA) is a byproduct generated from coal combustion, typically collected at the top of boilers in coal-fired power plants. During and after burning, mineral particles in the coal liquefy, evaporate, and solidify. Rapid cooling of these particles in the post-combustion zone forms spherical, amorphous FA grains due to surface tension [36].

Fly ash is classified into two main chemical types worldwide, primarily for its use in the cement industry: Class C and Class F. Fly ash is made up of fine, powdery particles that are mostly spherical, either solid or hollow, and primarily amorphous. According to the ASTM C618 standard, the ash with the combined weight of more than 70% of silica (SiO_2), alumina (Al_2O_3), and iron oxide (Fe_2O_3) is classified as Class F, while the ash with 50% to 70% of these components is classified as Class C [37]. Class C fly ash has over 15% calcium oxide (CaO), while Class F fly ash contains less than 5% CaO [38]. Class C is produced from younger lignite or sub-bituminous coal, and Class F comes from older anthracite and bituminous coal [38]. Class F is pozzolanic, because it has silica compounds that react with calcium hydroxide at ambient temperature to form cementitious compounds [38], [39].

FA appearance varies from tan to black in colour, depending on the amount of unburned carbon present [36]. The particles are normally spherical and can be either solid or hollow, with an amorphous (glassy) nature [36]. The particle sizes range from less than 1 µm to 150 µm. FA has a specific gravity ranging between 2.1 and 3.0, and a specific surface area from 170 to 1000 m²/kg [36].

FA improves workability, reduces hydration heat, and minimizes thermal cracking in cementitious materials at early ages, while also enhancing mechanical strength and durability in later ages. The spherical shape of FA creates a ball bearing effect, which significantly improves workability, particularly at higher replacement levels [36].

2.5.3 Municipal Solid Waste Incinerated Bottom Ash

The residue collected from the bottom of a municipal solid waste incinerator is known as municipal solid waste incinerated bottom ash (MSWI BA) [40]. When one metric ton of municipal solid waste (MSW) is incinerated in a waste-to-energy plant, it typically produces 200–250 kg of MSWI bottom ash (BA) and 10–30 kg of MSWI fly ash (FA) [41].

Because of its heterogeneous composition and high risk of excessive leaching, freshly produced MSWI bottom ash is unsuitable for use as a mineral resource to produce construction materials. Quality-upgrade treatments, such as plant-scale treatments and lab-scale treatments, are done on fresh MSWI bottom ash to make it suitable for application as SCM and AAM precursor [40].

Organic matter, HMs, and a variety of other elements (for example, As and Sb) are hazardous components of MSWI ash, which pose environmental risks. Incorporating MSWI ash into cement or concrete can reduce its contribution to environmental injustice caused by building and waste management. Pre-treating the MSWI ash before its use in cementitious materials is essential to lower its toxicity and ensure safe integration, making it a vital step in promoting environmental justice in construction and waste management [41].

Bottom ash is porous and grey in colour. The main elements found in bottom ash are silicon (Si), iron (Fe), aluminium (Al), and calcium (Ca), and their content depend on the particle size. The primary component of MSWI bottom ash is SiO_2, while CaO and Al_2O_3 also make up significant portions, each accounting for about 10% [42]. The chemical composition of MSWI bottom ash is similar to coal fly ash as shown in Figure *2.12* [40].

The amorphous phase is the main reactive phase in MSWI bottom ash (MBA), and its chemical composition affects the formation of reaction products [9]. The reactivity of MSWI bottom ash, like coal fly ash and BFS, likely depends on the levels of CaO, Al_2O_3, and SiO_2 in its amorphous phase. The reactivity of MSWI bottom ash as an SCM and AAM precursor may be comparable to that of Class F coal fly ash, making it a promising alternative [40].

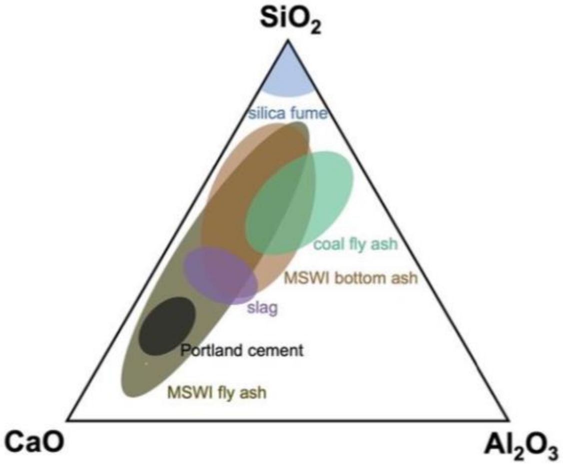

Figure 2.12 Composition of MSWI BA, GGBFS and FA [41].

2.6 Reaction Mechanism of Alkali Activated Materials

Alkali-activated materials (AAMs) are created from two primary components: the activator and the precursor, with the precursor typically being a powdered, amorphous mineral [43]. The microstructure of AAMs is largely influenced by the calcium content in the precursors, which leads to different reaction mechanisms. Based on the chemical composition of the precursors, AAMs can be classified into the following groups [44]:

Low-Calcium Systems: These systems use precursors that are rich in aluminosilicates and contain little to no calcium oxide. Class F fly ash (FA), according to ASTM C618, is the most representative precursor for low-calcium systems, producing alkali aluminosilicate (N-A-S-H) gel with a highly crosslinked, disordered pseudo-zeolitic structure [43], [44].

High-Calcium Systems: These systems use precursors rich in calcium oxide, sometimes along with aluminum oxide, and have a Ca/(Si+Al) ratio greater than 1. Blast furnace slag (BFS) is the most representative precursor for high-calcium systems [31], leading to the formation of calcium aluminosilicate hydrate (C-A-S-H) gel with a tobermorite-like structure [43], [44].

Blended Systems: Hybrid systems that combine both high and low calcium precursors can result in the coexistence of both sodium-aluminosilicate-hydrate (N-A-S-H) and Calcium-aluminosilicate-hydrate (C-A-S-H) gels in the final reaction product [44].

BFS-based AAMs generally exhibit a short setting time, rapid slump loss, and high structural build-up rate. In contrast, FA-based AAMs, particularly those using Class F fly ash, require higher curing temperatures (60–85°C) to activate due to FA's low reactivity at ambient temperatures. However, once cured at high temperatures, FA-based AAMs show good mechanical properties and durability. Hybrid systems blending BFS and FA are often used to achieve a balance between these characteristics by combining the complementary benefits of both materials and compensating for their drawbacks [44].

The reaction mechanism of BFS and FA alkali-activated system by NaOH and Na2SiO3 can be divided into five stages based on isothermal calorimetry studies as shown in Figure *2.13* according to [45]:

(I) **Initial Stage**: Rapid dissolution of precursors, with BFS dissolving faster than FA due to weaker Ca-O-Si, Mg-O-Si, and Al-O-Al bonds compared to Al-O-Si bonds in FA. This produces the initial heat evolution peak [45].

(II) **CASH Gel Formation**: Calcium-aluminosilicate-hydrate (CASH) gel forms on both BFS and FA surfaces, marked by the second heat peak. FA particles act as nucleation sites, preventing Si-rich layer formation on BFS that could inhibit further dissolution [45].

(III) **Formation of Shells on BFS Particles**: In the third stage, reaction products accumulate on BFS surfaces, forming shells that slow further BFS dissolution while FA continues reacting slowly [45].

(IV) **Formation of NASH Gel**: In the fourth stage, high ion concentrations around FA particles promote sodium-aluminosilicate-hydrate (NASH) gel formation. NASH and CASH gels interact through ion exchange and restructuring. [45].

(V) **Formation of Shells on FA Particles**: In the fifth stage, a shell forms on the surface of the FA particle, eventually halting further dissolution. Over time, if the reaction continues long enough, a thermodynamically stable CASH gel will form, leading to a steady state in the process [45].

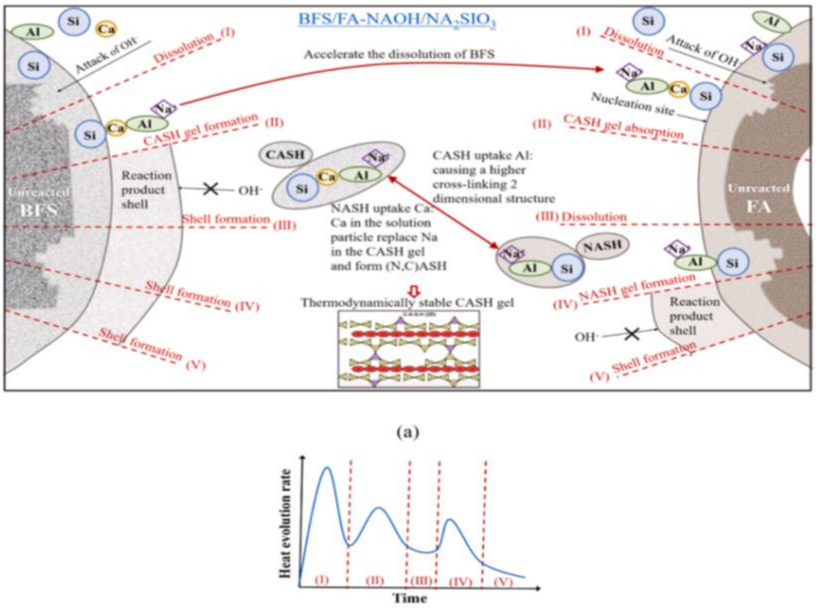

(a)

(b)

Figure 2.13 (a) Reaction mechanism of BFS and FA blended AAMs; (b) theoretical heat evolution curve of BFS and FA blended AAMs [45].

2.7 Conclusion

In conclusion, this chapter has provided a thorough exploration of the various 3D concrete printing techniques currently employed in the construction industry, with a particular focus on the extrusion-based method known as Concrete Printing. This chapter has outlined the classification of 3D concrete printing technologies, emphasizing the advantages and limitations of each.

A significant portion of the chapter was dedicated to understanding the rheological behaviour of concrete, which is crucial for the successful application of extrusion-based 3D printing. Additionally, the chapter explored the use of sustainable materials, specifically AAMs composed of BFS, FA, and MSWI BA, for enhancing the environmental benefits of 3D concrete printing. These insights will guide the subsequent research focused on optimizing the concrete mix for extrusion-based 3D printing, particularly when using AAMs.

3

Materials and Methods

3.1 Introduction

This chapter presents an overview of the materials used in this study for the development of alkali-activated mortar intended for 3D printing applications. It includes a detailed characterization of their physical and chemical properties. It further details the mix design formulation, sample preparation and the experimental methods employed. The experimental program in this study primarily focuses on understanding the properties of mixtures in the fresh state, as these largely govern the printability of alkali-activated mortar.

3.2 Materials and Methods

3.2.1 Materials

The precursors used in this study include Blast Furnace Slag, Fly Ash, and Municipal Solid Waste Incineration Bottom Ash. BFS was sourced from Eco2Cem Benelux B.V., Class F coal fly ash was supplied by Vliegasunie B.V and pretreated MSWI BA was provided by a local supplier. These materials were analysed for their particle morphology, particle size distribution, and chemical composition, and their characteristics are presented and discussed in this section.

3.2.2 Particle Morphology

The material characteristics, such as particle geometry, including particle shape and size distribution, play a significant role in determining rheology [46]. The morphologies of BFS, FA, and BA were captured using a scanning electron microscope (SEM) at an accelerating voltage of 15 kV and 5000× magnification. These SEM images provided detailed insights into the shape and surface texture of each material.

The SEM image of BFS in Figure *3.1* shows that BFS particles are angular and irregular in shape. This high angularity, combined with fine particle size and rough surface texture contributes to increased interparticle friction and a higher surface area. These characteristics enhance the reactivity of BFS but simultaneously reduce workability of the slag-based mixes [47], [48], [49].

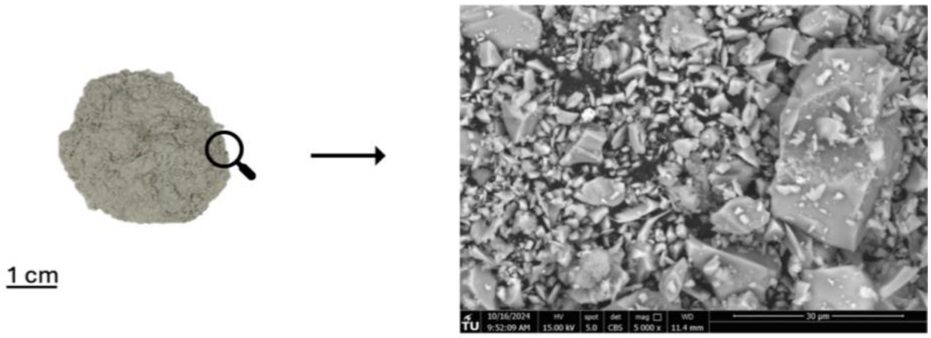

(a) (b)

Figure 3.1 (a) Raw BFS powder and (b) SEM image of BFS.

Fly ash particles, as shown in Figure *3.2*, are predominantly spherical. In the SEM image, the fine solid particles are called as microspheres, and hollow spherical particles are referred to as cenospheres. In addition to these, larger particles known as plerospheres can also be observed. These are also hollow spheres, but are larger and encapsulate smaller microspheres, forming a “sphere-in-sphere” structure due to combustion processes involving differential melting and gas evolution [50], [51], [52]. Their smooth surfaces create a ‘ball-bearing’ effect, reducing interparticle friction [46], [53]. This is known to improve the material’s workability at the same water-binder ratio [53].

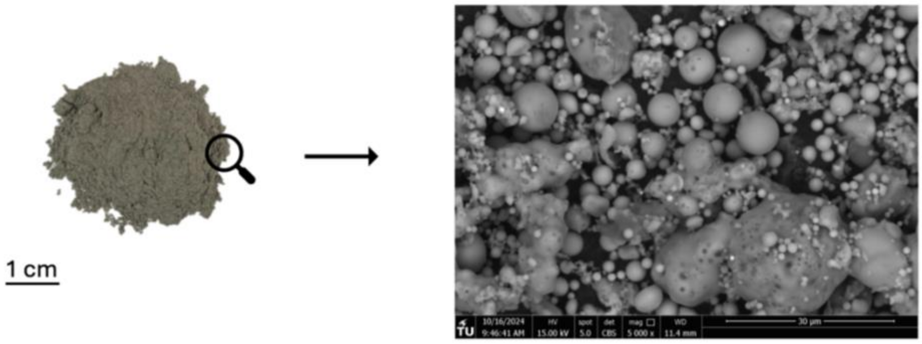

(a) (b)

Figure 3.2 (a) Raw FA powder and (b) SEM image of FA.

The SEM image of BA in Figure *3.3* reveals that the particles are highly irregular and angular with sharp edges and rough, uneven surfaces marked by fractures. The irregular and angular shape is typical for mechanically ground materials. This variability in size and shape highlights the complex morphology of BA.

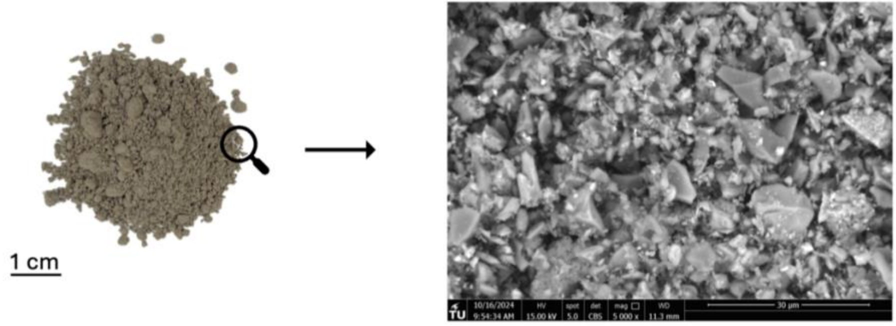

(a) (b)

Figure 3.3 (a) Raw BA powder and (b) SEM image of BA.

Compared to FA, BFS and BA particles look finer and more angular. The replacement of spherical FA particles with more angular and finer BA particles is expected to result in reduced flowability and lubrication effect due to higher surface friction from interlocking [54]. These features are expected to potentially reduce the workability and increase water demand of alkali-activated mixes [46].

3.3 Particle Size Distribution

The particle size distribution of BFS, FA and MSWI BA materials was measured using the laser diffractometry. The results are presented in Figure *3.4*, with the cumulative percentiles (D_{10}, D_{50}, D_{90}) summarized in Table *3.1*. The average particle sizes (D_{50}) of BFS, FA and MSWI BA are 26.08 µm, 45.39 µm and 6.99 µm respectively. Among the three materials, BA particles are the finest, with most particles below the D_{50} of BFS, followed by BFS and FA, with FA exhibiting the broadest size range.

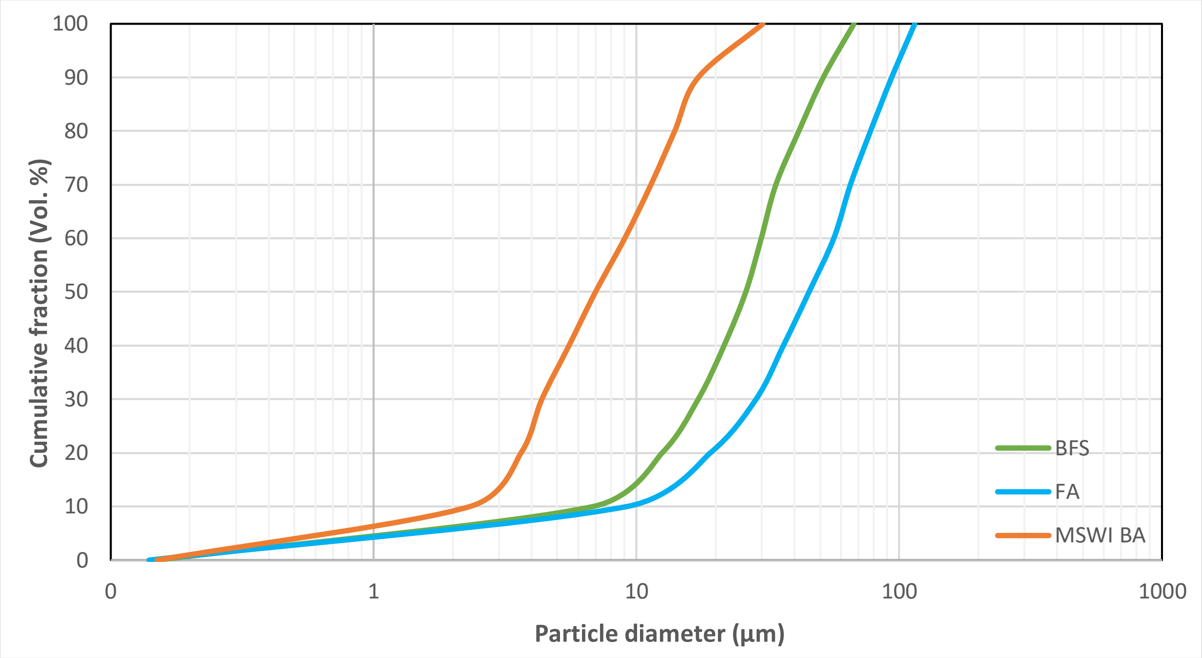

Figure 3.4 Particle size distribution of BFS, FA and BA determined by laser diffractometry.

Table 3.1 Cumulative particle size percentiles.

Precursor	D_{10} (µm)	D_{50} (µm)	D_{90} (µm)
BFS	6.85	26.08	51.43
FA	9.23	45.39	93.63
MSWI BA	2.33	6.99	17.19

The PSD analysis confirms that BA particles are very finer compared to both BFS and FA. This observation aligns with SEM findings, which highlighted that BA particles are smaller than BFS and FA, with both BFS and BA exhibiting angular shapes. The finer particles of BA, combined with their angular and rough surfaces, result in a higher surface area, which can negatively impact workability by increasing water demand during wetting process. Higher fineness and angularity are known to contribute to increased interparticle friction, contact forces and reduced flowability, leading to a loss of workability compared to binders with lower fineness [47], [48].

3.4 Chemical Composition

The chemical composition of the amorphous phase of BFS, FA, and BA, obtained from reference data, is presented in Table *3.2*. Additionally, Figure *3.5* compares the CaO/SiO_2 and SiO_2/Al_2O_3 mass ratios in amorphous phase of these materials. This comparison helps in highlighting key differences in their chemical composition and reactivity.

The initial chemical composition of system and the reaction extent of raw materials significantly influences the formation and composition of reaction products [55]. The amorphous phase in the precursors is the most reactive while crystalline phases (e.g., quartz, mullite and hematite) are generally inert or react very slowly, minimally contributing to reaction process [56]. Blast Furnace Slag is fully amorphous (100%), ensuring maximum reactivity in alkali-activated systems, while FA and BA contain 74% and 64.7% amorphous content, respectively. Thus, the presence of crystalline phases in FA and BA reduces their reactivity compared to BFS.

Slag contains the highest amount of CaO at 36.3%, followed by Bottom Ash (BA) with 10.87%, and Fly Ash (FA) with the lowest content at 4.3%. In contrast, FA has the highest amount of reactive silica (41.5%) compared to BFS (35%) and BA (29.09%). A previous study on the reaction kinetics of NaOH- and Na_2SiO_3-activated BFS has shown that higher Al_2O_3 content can slow reaction kinetics and reduce early-stage compressive strength [57]. The Al_2O_3 content in BFS and FA is nearly similar, while BA has the lowest content. In earlier studies, a CaO/SiO_2 ratio close to 1.0 has been identified as optimal for enhancing reactivity and achieving higher strength in alkali-activated systems [55]. BFS closely aligns with this ideal ratio, contributing to its superior performance. Additionally, the deviations from the optimal SiO_2/Al_2O_3 ratio, whether higher or lower, lead to reduced strength, primarily due to the presence of unreacted silica or alumina remaining in the matrix. BFS and FA have SiO_2/Al_2O_3 ratios of 2.4 and 2.6, respectively, both within a suitable range for strength development. However, BA has a significantly higher ratio of 4.2, indicating excess silica and reduced reactivity. Therefore, Compared to FA and BA, the reactivity of slag is higher.

Table 3.2 Chemical composition of amorphous phase in BFS, FA and BA [58].

Compounds	Percentages in amorphous phase (wt. %)		
	BFS	FA	MSWI BA
SiO_2	35	41.3	29.09
CaO	36.3	4.3	10.87
Al_2O_3	14.3	15.7	6.94
MgO	9.4	0.9	2.15
Na_2O	0.2	0.9	4.52
Fe_2O_3	0.4	5.1	4.74
Others	4.4	5.8	6.39
Sum	100	74	64.70

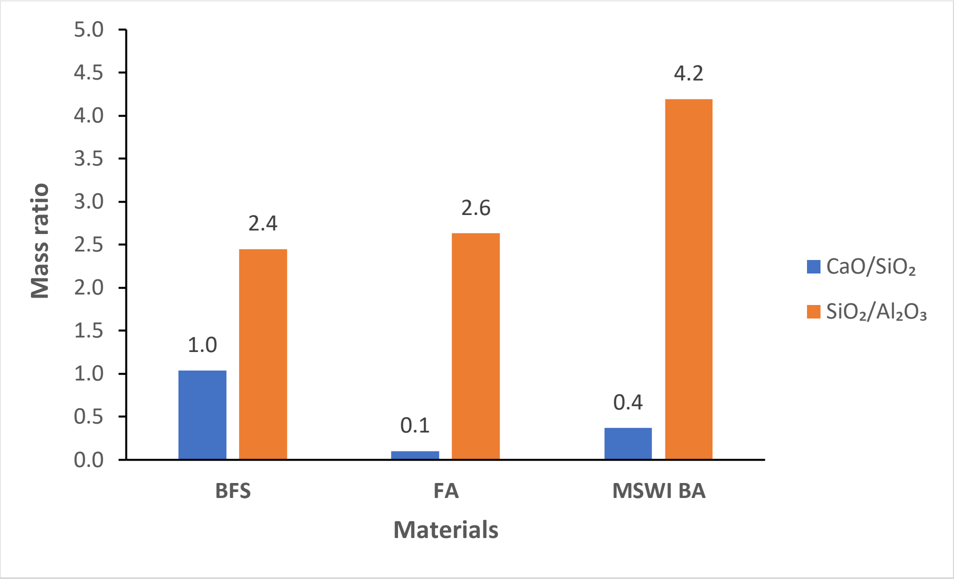

Figure 3.5 Comparison of CaO/SiO_2 and SiO_2/Al_2O_3 mass ratios in the amorphous phase of BFS, FA, and BA.

3.5 Metallic Aluminium content

To ensure the suitability of MSWI bottom ash (BA) for alkali activation, the metallic aluminium content of MSWI BA was determined. In an alkaline environment, MSWI bottom ash undergoes a reaction where the metallic aluminium present reacts with water, producing hydrogen gas as shown in the Eq.3.1. When this reaction takes place during the setting phase of the matrix, before full hardening, the generated hydrogen gas can lead to expansion and increased porosity, reducing the strength and durability of the material [59].

$$2\mathrm{Al} + 2\mathrm{NaOH} + 6\mathrm{H_2O} \rightarrow 2\mathrm{Na[Al(OH)_4]} + 3\mathrm{H_2}\uparrow \quad \mathrm{pH} > 11 \qquad \text{(Eq. 3.1)}$$

To conduct this test, a small quantity of BA was added to a conical flask containing 1 M NaOH solution in 1:10 ratio. The experimental setup is shown in Figure *3.6*.The flask was placed on a magnetic stirrer to ensure uniform mixing. It was connected to a graduated cylinder using a rubber tube. The graduated cylinder was submerged upside-down in a water bath to collect any gas released during the reaction through the tube.

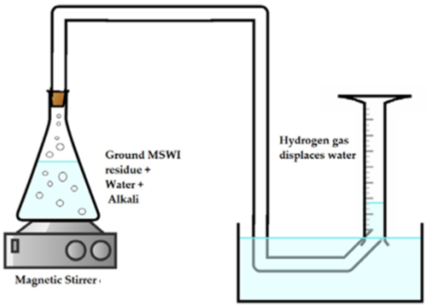

Figure 3.6 Set up to determine metallic aluminium in bottom ash [59].

Following the test, no hydrogen gas evolution was observed, indicating that metallic aluminium had been effectively removed during the pretreatment process. This confirms that the MSWI bottom ash is safe for use in alkali-activated mixtures without the risk of gas formation or expansion during curing.

3.6 Mix design and Mixing Procedure

The primary challenge in 3D-printed concrete mix design lies in balancing the conflicting requirements of extrudability and buildability [2]. The printable mixes generally require high binder content [5] and fine aggregates, as equipment limitations prevent coarse particles from passing through precision nozzles [5], [25]. Traditional concrete design principles prove unsuitable for alkali-activated printing materials. Given the absence of established protocols in this emerging field, successful implementation necessitates balancing workability with setting time requirements while accommodating material constraints [25].

In this research, BFS and FA were used as precursors to develop the reference mix, while BFS and BA were used to obtain the target mix. Standard sand sourced from Normensand GmbH, Germany, conforming to CEN EN-196 standards, was used as the fine aggregate in the preparation of all mortar mixes. The alkali activators used were sodium hydroxide (NaOH) from Brenntag and sodium silicate (Na_2SiO_3), commonly known as waterglass, was sourced from PQ Corporation. Their composition is as follows:

- Sodium hydroxide: NaOH - 50%, H_2O - 50%.
- Sodium silicate: Na_2O - 15%, SiO_2 - 30%, H_2O - 55%.

In the mixture design, the total binder mass (denoted as b) consists of blast furnace slag (BFS) and either fly ash (FA) or municipal solid waste incineration bottom ash (MSWI BA), i.e., b = BFS + FA/MSWI BA. The term w/b refers to water-to-binder ratio, representing the mass ratio of water (w) to the total binder (b). The percentage of sodium oxide (Na_2O) in the activator solution calculated by weight of binder is denoted by alkali content (Na_2O/b). The molar ratio of silica (SiO_2) to sodium oxide (Na_2O) in the activator solution is represented by activator modulus (SiO_2/Na_2O). In this context, silica is provided solely by the sodium silicate activator, while sodium oxide is contributed by both sodium silicate and sodium hydroxide. The sand-to-binder ratio (s/b) is maintained constant at 1.5 for all the mortar mixtures throughout the study. The details of the mixture compositions used in this study are presented in Table *3.3*.

Table 3.3 Compositions of the mixtures.

Mix-ID	**Precursors (%)**			**w/b**	**Na_2O/b (%)**	**SiO_2 / Na_2O**
	BFS	FA	MSWI BA			
20FA-BFS_0.38	80	20	-	0.38	5	0.5
20FA-BFS_0.4	80	20	-	0.4	5	0.5
20BA-BFS_0.4	80	-	20	0.4	5	0.5

The activator solution was prepared by mixing NaOH, Na_2SiO_3, and water in specific proportions to achieve the required composition for alkali activation of binder. The additional water added was calculated by excluding the water present in the commercial sodium hydroxide and sodium silicate solutions from the total water required to maintain the desired water-to-binder ratio. The prepared solution was then allowed to cool for 24 hours before use. For the preparation of all the mortar mixes, a constant sand-to-binder mass ratio of 1.5 was maintained throughout. The mixing protocol for mortar preparation is presented in Table *3.4*. For paste preparation, the same protocol was followed as shown in the Table *3.4*., but without the addition of sand.

Table 3.4 Hobart mixing protocol for mortar [60].

Time (min:sec)	Procedure
-2:00	The sand was homogenized at Speed 1 (60 rpm) with a Hobart mixer for 1 minute.
-1:00	Mixing was stopped; precursors were added; mixing continued at speed 1 for 1 minute.
0:00	Alkali activator solution was added; mixing continued at speed 1 for 1minute.
1:00	Mixing was stopped; the bottom and walls of the container were scraped for 30 seconds.
1:30	Mixing resumed at speed 2 (124 rpm) for 1 minute.
2:30	Mixing was stopped.

3.7 Test Methods

As outlined in the research methodology (Chapter 1), this research follows a systematic three-stage approach designed to comprehensively evaluate the incorporation of municipal solid waste incineration bottom ash (MSWI BA) as a sustainable alternative to fly ash in 3D printable alkali-activated materials. The experiments involved in this multi-stage methodology are discussed in this section. This experimental investigation addresses the research objectives by progressing from evaluating MSWI BA incorporation, through understanding the mechanisms governing rheology and reaction kinetics, to assessing environmental benefits.

The experimental framework is designed to establish not only the technical feasibility of MSWI BA incorporation but also to elucidate the fundamental mechanisms governing its influence on printability performance. Each stage builds upon the previous findings, creating a comprehensive understanding of how waste-derived precursors can be effectively utilized in advanced manufacturing applications while maintaining environmental sustainability.

Stage 1: Development of 3D Printable AAM with MSWI BA

This stage focuses on the systematic development and optimization of alkali-activated mortar formulations suitable for extrusion-based 3D printing. The primary objective is to establish mix designs that successfully incorporate MSWI BA as a replacement for fly ash while satisfying multiple printability criteria. These criteria are evaluated through mini slump and slump flow tests (buildability and flowability), mini extrudability test (continuous extrusion capability), Vicat test (setting time), and mechanical strength tests (compressive and flexural) as shown in Figure *3.7*. Through these comprehensive assessments, the stage demonstrates the technical feasibility of incorporation of MSWI BA in AAMs for 3D printing applications.

Mini slump and slump flow

Mini Extrudability

Vicat test

Mechanical strength tests

Figure 3.7 Overview of experiments in stage 1.

Stage 2: Impact of MSWI BA on Printability of AAM

This stage investigates the fundamental mechanisms governing how MSWI BA influences printability. The investigation employs slugs test for rheological characterization alongside three techniques for reaction kinetics analysis: Inductively coupled plasma emission spectroscopy (ICP-OES) for pore solution analysis, thermodynamic modelling, and Fourier Transform Infrared spectroscopy (FTIR) for solid phase characterization as shown in Figure *3.8*. Through this integrated approach, the stage aims to elucidate the relationship between MSWI BA incorporation, early-age reaction kinetics, and rheological behaviour that determines printability performance.

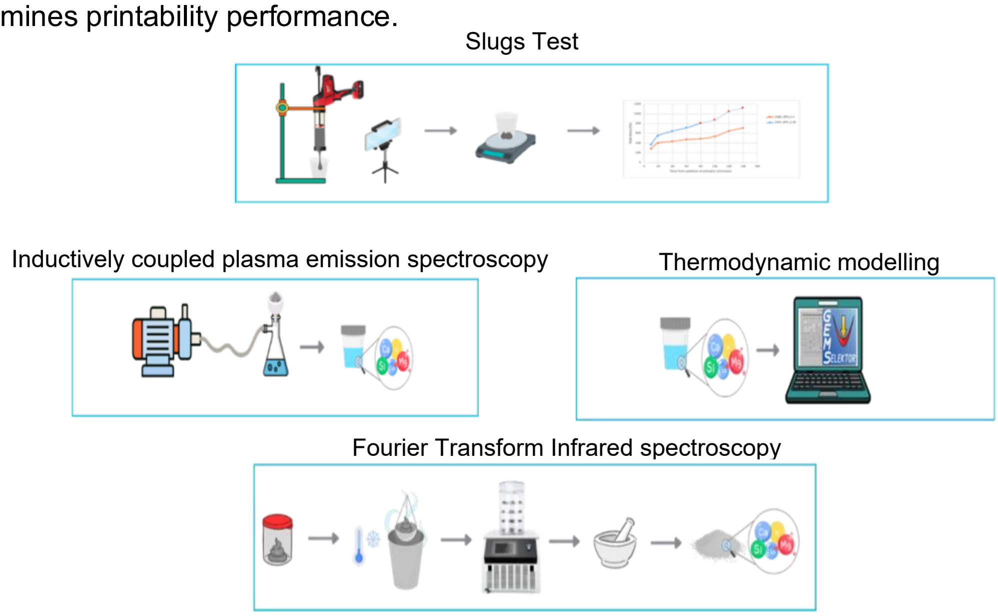

Figure 3.8 Overview of experiments in stage 2.

Stage 3: Environmental Impact Assessment through LCA

This stage evaluates the environmental implications of incorporating MSWI BA in 3D printable alkali-activated materials through life cycle assessment as shown in Figure *3.9*. The assessment quantifies and compares environmental impacts across multiple categories using shadow costs as an integrated indicator. Through this evaluation, the stage demonstrates the sustainability benefits of MSWI BA utilization and provides environmental justification for its adoption as a fly ash alternative in additive manufacturing applications.

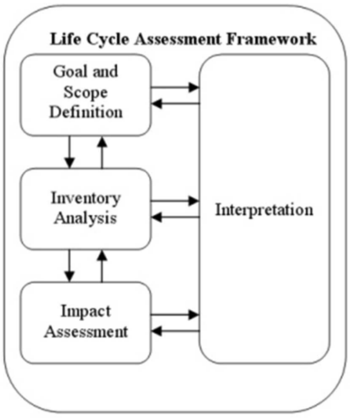

Figure 3.9 Life cycle assessment framework.

3.7.1 Stage 1: Development of 3D Printable AAM with MSWI BA

3.7.1.2 Slump and Slump flow

The slump and flow table tests, performed at the mortar level, provide valuable insights into the rheological behaviour of the material. The slump value is associated with the static yield stress, indicating the material's ability to hold its shape, which is critical for assessing buildability. Similarly, the slump-flow value is related to the dynamic yield stress, reflecting the material's flow behaviour, which is essential for evaluating pumpability [61]. For successful 3D printing, these properties must be balanced: the material must flow easily during pumping (high flowability/low dynamic yield stress) while maintaining shape after deposition (high buildability/adequate static yield stress) [6]. Therefore, this research employs both tests to optimize mix designs that achieve this critical balance between pumpability and buildability.

The slump height was measured as the difference between the height of the cone and the final height of the material at the centre after the cone was removed. The slump flow value was determined by measuring the average diameter across two perpendicular lines after the material spread following 25 drops [25], [62] as illustrated in the Figure *3.10*. Therefore, lower slump values imply that the material can hold its shape better, while a larger slump-flow diameters indicate better flow. The slump cone used for the test had dimensions of 100 mm in diameter at the bottom, 70 mm in diameter at the top, and 60 mm in height in accordance with ASTM C230/C230M – 13 [63]. The test was conducted following the procedure outlined in ASTM C1437 – 20 [62]. Measurements were taken every 20 minutes over a period of 2 hours to monitor the slump development that may occur during the printing process.

Different studies have reported varying ranges of slump and slump flow values for assessing the printability of AAMs. A key factor contributing to these variations was the choice of test setup. Differences in cone height, base diameter, can affect the measured values, leading to discrepancies across studies. This study considered the slump and slump flow values reported by Tran et al. [64] as a reference, which identified mixtures with initial slump values of 15–30 mm combined with initial slump flow values of 210–240 mm to be optimal for 3D printing of AAMs. Most research shows that slump values below 8 mm and slump flow values below 160 mm [61], [64], [65] result in mixes that are too dry and unsuitable for printing. These values mark the minimum criteria for the slump and slump flow of the developed mixes. The variations in slump and slump flow values arise due to differences in binder composition, activator concentration, and additive incorporation, all of which influence the material's flowability [5]. To address these influencing factors, this research employed a systematic stepwise optimization approach, sequentially varying the slag-to-binder ratio (BFS/b), alkali content (Na_2O/b), activator modulus (SiO_2/Na_2O), and water-to-binder ratio (w/b) to achieve target printability values. This optimization strategy enabled the development of both reference (FA-based) and target (MSWI BA-based) mixes that satisfy the stringent requirements for 3D printing applications.

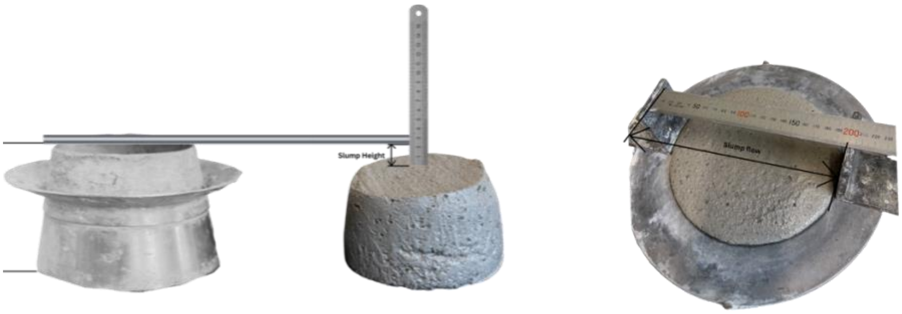

(a)

(b)

Figure 3.10 (a) Slump height and (b) slump flow test.

3.7.1.3 Mini-Extrudability test

The mini extrudability test provides direct validation of a material's suitability for extrusion-based 3D printing at laboratory scale. The test is conducted by manually extruding fresh mortar using an extrusion gun with a 10 mm diameter circular nozzle to produce continuous filaments in a layer-by-layer manner as shown in Figure *3.11*. The extruded filaments are visually assessed for critical quality indicators: surface smoothness (absence of tears or cracks), flow continuity (no blockage or interruption) and shape retention (maintenance of circular cross-section).

Figure 3.11 Mini-extrudability test.

3.7.1.4 Vicat Test

Open time is the duration after mixing the activator solution during which the material remains extrudable through the printer nozzle. For a concrete mix to be suitable for 3D printing, its open time must exceed the total extrusion time required for the printing process [6]. Open time can be assessed using the initial setting time and certain rheological parameters. A slower increase in static yield stress or a longer initial setting time generally results in an extended open time [5]. Therefore, the requirement for setting time depends on the scale of the 3D printing setup. The printing trials conducted in some studies indicated that an optimal initial setting time of 90 minutes [66], [67] provided a sufficient printable time window for execution.

The Vicat test was performed using Vicat apparatus (shown in Figure *3.12*) according to NEN-EN 480-2:2006 [68] at mortar level to determine the setting time as shown in Figure *3.12*. The dimensions of the mould of the Vicat apparatus are 40 ± 0.2 mm in height, with an internal diameter of 70 ± 5 mm at the top and 80 ± 5 mm at the bottom [68]. Initial setting time for mortar is the time measured from addition of activator solution to the mixture until the time at which the distance between the needle and the base plate is 4.0 mm. The final setting time measured from addition of activator solution to the mixture until the time after which the needle no longer penetrates 2.5 mm into the specimen is the final setting time of the mortar mixture. The setting time was considered as the average of three tests.

Figure 3.12 Vicat apparatus.

3.7.1.5 Mechanical Strength Tests

The mechanical strength tests of mortar prisms, which include compressive strength test and flexural strength test, were tested in accordance with NEN-EN 196-1:2016 [69]. The mortar mixture, prepared using a Hobart mixer, was placed into prism moulds of 160 × 40 × 40 mm^3. To prevent moisture loss, the specimens were sealed and cured in a fog room under controlled conditions of 20 ± 2 °C temperature and 95 ± 5% relative humidity until testing at 7 and 28 days. The prisms were first tested for flexural strength following the standard procedure. Subsequently, the broken halves from the flexural test were used for the compressive strength test (shown in Figure *3.13*). Hence, flexural strength was calculated as the average of three samples, while compressive strength was determined as the average of six samples for each testing age. The target mechanical performance for 3D printing applications requires a minimum 28-day mould cast compressive strength of 45 MPa and flexural strength of 9 MPa [70], [71], ensuring adequate structural capacity for printed elements.

(a) (b)

Figure 3.13 (a) Flexural strength test and (b) compressive strength test.

3.7.2 Stage 2: Impact of MSWI BA on Printability of AAM

3.7.2.2 Slugs Test

The slugs test was selected for monitoring yield stress evolution due to its specific advantages for mortar-scale testing in 3D printing applications. Unlike conventional rheometers, which are primarily designed for paste measurements and require sophisticated laboratory setups, the slugs test provides a simple, direct method suitable for mortar systems with aggregate particles. This technique enables on-site measurements during actual printing operations, making it particularly valuable for quality control and real-time assessment of printability. Furthermore, the test directly measures yield stress at conditions mimicking nozzle extrusion, providing more relevant data [72].

This test is based on the observation that, under gravity-driven flow, the material forms discrete slugs (drops) when extruded through a nozzle. The mass of these slugs directly correlates with the material's yield stress, providing a quantitative measure of rheological properties [72].

The mathematical model behind the slugs test is derived from Herschel-Bulkley viscoplastic flow theory and when viscosity effects are neglected, the yield stress (τ_c) is given by Eq. 3.2:

$$\tau_c = \frac{g}{\sqrt{3}s} m_s \quad \text{(Eq. 3.2)}$$

where g is the gravitational acceleration, m_s is the mass of the slug, and S is the nozzle cross-sectional area.

The manual slugs test was performed by extruding the material through a 10 mm-diameter nozzle, collecting approximately 5 slugs, and determining their mass. The total collected mass (m_t) was divided by the number of slugs (n) to estimate the average mass of each (m_s) as:

$$m_s = \frac{m_t}{n} \quad \text{(Eq. 3.3)}$$

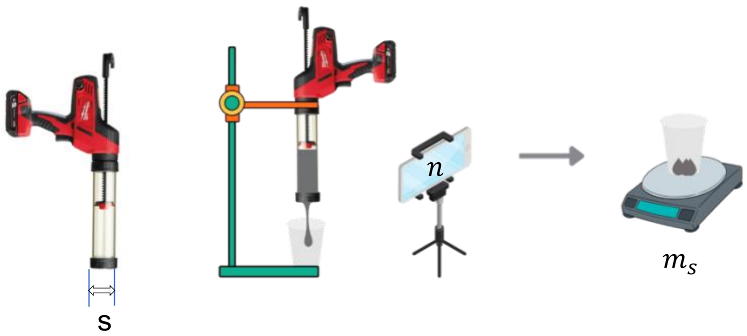

Figure 3.14 Slugs test for yield stress measurement showing marked parameters S (nozzle area), n (slug count), and m_s (slug mass).

3.7.2.3 Inductively Coupled Plasma Optical Emission Spectroscopy

Inductively Coupled Plasma Optical Emission Spectroscopy (ICP-OES) is widely used for the chemical analysis of pore solutions in AAMs due to its high sensitivity and ability to detect multiple elements simultaneously. In alkali-activated materials (AAMs), the composition of the pore solution provides crucial insights into the dissolution of precursors, the formation of reaction products, and the evolution of solid phases. Alkali activation follows a dissolution-precipitation mechanism, where the concentration of dissolved species in the pore solution determines the solubility and saturation state of key reaction products [73]. Monitoring these concentrations helps in understanding the kinetics of precursor dissolution, the development of sodium aluminosilicate hydrate (N-A-S-H) and/or calcium-aluminosilicate hydrate phases (C-A-S-H), secondary reaction products and the overall reaction process [73]. In this study, ICP-OES was used to analyse the concentrations of calcium (Ca), aluminium (Al), silicon (Si), sodium (Na), and magnesium (Mg) in the pore solution of BFS/FA-AAM and BFS/BA-AAM over time. These elements are crucial because they directly influence the formation and composition of reaction products, which govern the microstructure and mechanical performance of the material.

The ICP-OES test was conducted on past level considering that sand is inert and does not participate in the reactions. The paste was prepared using deionized water according to the procedure mentioned in the Table *3.4* without the addition of Sand. The sample preparation for ICP-OES involved the extraction of pore solution from the fresh pastes using a pump as (shown in Figure *3.15*). The suction hose of the pump was connected to the side port of an Erlenmeyer flask. A funnel was placed on top of the flask and sealed using a rubber sealing ring to ensure an airtight connection between them [74]. Whatman 41 filter paper was placed inside the funnel before introducing the fresh paste to separate solid particles from the liquid phase. The vacuum pump was then used to draw the pore solution from the paste for 5 minutes. The solution was extracted every 20 minutes for 140 minutes. To prevent precipitation, the extracted pore solution was immediately diluted with acid before ICP-OES analysis.

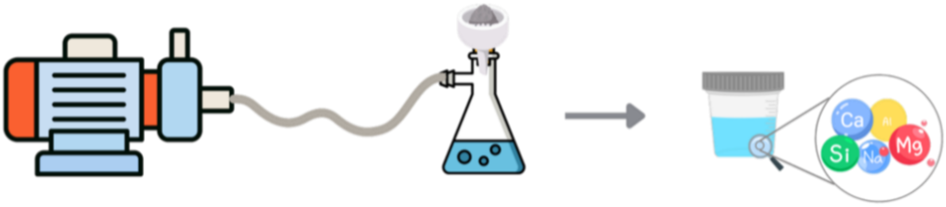

Figure 3.15 Sample preparation for ICP-OES.

3.7.2.4 Thermodynamic modelling

Thermodynamic modelling of pore solutions was conducted using the Gibbs Energy Minimization Selektor (GEMS, version 2023) to predict the possibility of precipitation of solid phases from saturation index.

The analysis was performed using the CEMDATA18 database [75] developed for AAMs along with the thermodynamic database for N-C-A-S-H model recently developed in [76], [77]. The elemental concentrations measured by ICP-OES in the pore solutions of two developed 3D-printable mixes were used as input to calculate the ionic activities directly. Since saturation indices can be misleading for comparison of phases that dissociate into differing numbers of ions[78]. For this reason, "effective" saturation indices (ESI) are computed by dividing the saturation indices (SI) by the total number of ions released during the dissolution reaction to form the solids [78].

The effective saturation index is then calculated from the following (Eq. *3.4*) and (Eq. *3.5*) [78].:

$$SI = log\left(\frac{IAP}{K_{S0}}\right)$$

(Eq. 3.4)

$$ESI = \frac{SI}{N}$$

(Eq. 3.5)

where IAP is the ion activity product, K_{S0} is the equilibrium solubility product at 1 bar and 25°C, and N is the number of ions participating in the dissolution reaction [78].

The calculated ESI indicates thermodynamic stability, with positive values representing oversaturation (potential precipitation) and negative values indicating undersaturation (no precipitation). This allows the identification of phases, particularly early-age gels, whose potential precipitation might be challenging to detect experimentally.

3.7.2.5 Fourier Transform Infrared spectroscopy

Fourier Transform Infrared spectroscopy (FTIR) was conducted to track the degree of polymerisation, changes in chemical bonds, and the formation of hydration products over time [79], [80]. By analysing the characteristic wavenumbers and their transmittance patterns, the functional groups present in alkali-activated systems can be identified [79]. This makes FTIR a simple and effective analytical method for studying the material reactions [81]. The test was conducted at paste level as sand is considered inert and does not participate in the alkali-activation reactions.

FTIR test required sample preparation of paste mixture using deionized water. The paste mixture was first prepared and covered with plastic foil while resting under normal laboratory conditions to prevent moisture loss. To analyse the solid phase development over time, the reaction was stopped by freezing the samples in liquid nitrogen at 20-minute intervals from the time of activator addition. The frozen samples were then placed in a freeze dryer for one week to ensure complete drying before being ground into a fine powder for testing [82], [83] as shown in the Figure *3.16*. FTIR measurements were conducted using a Spectrum™ 100 Optical ATR-FTIR spectrometer over a wavelength range of 400 to 4000 cm^{-1} with a resolution of 4 cm^{-1}[83]. Each sample was scanned 30 times, with a background scan performed before each measurement to ensure accuracy.

(a) (b) (c)

Figure 3.16 Sample preparation process for FTIR analysis showing (a) liquid nitrogen freezing to stop reaction, (b) freeze drying, and (c) grinding to fine powder.

3.7.3 Stage 3: Environmental Impact Assessment through LCA

Life cycle assessment (LCA) was conducted to quantify and compare the environmental impacts of developed 3D printable alkali-activated mortars against other mixtures. Life cycle assessment (LCA) was conducted following ISO 14040/14044 standards [84] to quantify the environmental impacts of MSWI BA-based mortars compared to fly ash-based and OPC alternatives. This approach quantifies multiple environmental impact categories in monetary terms, enabling direct comparison of the sustainability benefits achieved through MSWI BA utilization in 3D printable alkali-activated materials.

3.8 Summary of Target Values

The summary of the target values considered for the development of 3D printable mixes is shown in Table *3.5*.

Table 3.5 Summary of the target values.

Performance Criteria	Test Parameter	Target Values
Buildability	Initial Slump Height	15-30 mm
	Final Slump Height	8 mm
Flowability	Initial Slump Flow	210-240 mm
	Final Slump Flow	160 mm
Open time	Setting Time	90 minutes
Mechanical Strength	28-day Compressive strength	45 MPa
	28-day Flexural strength	9 MPa

4

Development of 3D Printable Alkali activated Mortar Mixture with MSWI Bottom Ash

4.1 Introduction

This chapter presents the systematic development and optimization of alkali-activated mortar mix suitable for extrusion-based 3D printing applications. Two mix designs are developed: a reference mix utilizing blast furnace slag and fly ash as precursors, and a target mix where municipal solid waste incineration bottom ash replaces fly ash while BFS is retained as precursor.

For successful 3D printing applications, the printability of developed mixes must satisfy multiple performance criteria. This study assesses printability through three fundamental properties: buildability, which represents the material's shape retention ability measured by slump test; flowability, indicating the ease of material flow through the printing system measured by slump flow test; and extrudability, demonstrating continuous extrusion capability evaluated through mini extrusion test. Additionally, setting time determination provides critical information about the open time available for printing operations, while mechanical strength tests ensure the printed structures meet structural requirements. Target values for these properties have been established based on preliminary studies and literature benchmarks for printable cementitious materials, providing quantitative criteria for mix optimization.

The following are the steps involved in the development of mixes suitable for 3D printing application (shown in Figure *4.1*):

- **Step 1: Development of reference mix through optimization of buildability and flowability-** This initial step involves designing the reference mix using BFS and FA as precursors. To optimize printability, mini slump and slump flow tests are performed to assess buildability and flowability, respectively. Through these tests, key mixture parameters are systematically varied— the slag-to-binder ratio (BFS/b), alkali content (Na_2O/b), activator modulus (SiO_2/Na_2O), and water-to-binder ratio (w/b). Each parameter is varied independently while others remain constant. Once the optimal value for a parameter is identified, it is fixed for the subsequent steps. This systematic process allows for the isolation of individual effects on buildability and flowability characteristics, ultimately establishing a reference mix that meets target printability requirements.

- **Step 2: Development of target mix through optimization of buildability and flowability-** The reference mix composition fixed in the previous step serves as the starting point for developing the target mix, which incorporates MSWI BA as a replacement for fly ash. The mix proportions are systematically optimized to match the slump and slump flow characteristics of the reference mix, ensuring comparable buildability and flowability while demonstrating the feasibility of waste material utilization.

- **Step 3: Assessment of extrudability for developed reference and target mixes –** After the reference mix and target mix are established in the previous steps based on buildability and flowability characteristics, extrudability testing is conducted to validate the suitability for extrusion-based 3D printing. This manual test mimics the actual extrusion in printing process and provides direct assessment of the material's ability to be continuously extruded through a nozzle while maintaining shape stability.

- **Step 4: Determination of setting time for developed reference and target mixes -** Setting time determination using the Vicat apparatus establishes the critical time window for printing operations. This test ensures that both mixes maintain adequate workability during the printing process.

- **Step 5: Determination of Mechanical strengths for developed reference and target mixes -** The final validation step involves comprehensive mechanical characterization, including compressive and flexural strength testing. These tests confirm that the optimized mixes not only meet printability requirements but also achieve the target mechanical properties necessary for structural applications.

Step 1: Development of reference mix through optimization of buildability and flowability

Step 2: Development of target mix through optimization of buildability and flowability

Step 3: Mini Extrudability test on developed reference and target mixes

Step 4: Determination of setting time for developed reference and target mixes

Step 5: Determination of mechanical strengths for developed reference and target mixes

Figure 4.1Overview of the steps followed for development of reference and target mix.

This chapter demonstrates that through systematic optimization, it is possible to develop alkali-activated mortars that meet the demanding requirements of 3D printing while incorporating industrial waste materials, thereby advancing both technological innovation and sustainability in construction materials.

4.2 Development of Reference mix through optimization of buildability and flowability

4.2.1 Test Approach for Mini Slump and Slump flow to optimize buildability and flowability of Reference Mix

The optimization of the reference mix for buildability and flowability follows a systematic stepwise approach where mix design parameters are sequentially varied to achieve the target values for slump and slump flow (as shown in Table *3.5*). The buildability and flowability are significantly influenced by mix design parameters [60]. This relationship between composition and fresh-state properties necessitates a methodical optimization strategy that enables the identification of optimal parameter ranges while maintaining independent control over each variable's influence on printability.

The following mix design parameters were systematically investigated in this study:

- Slag-to-binder ratio (BFS/b)
- Alkali content (Na_2O/b %)
- activator modulus (SiO_2/Na_2O)
- water-to-binder ratio (w/b)

In this stepwise approach, only one parameter was varied and optimised at a time, while the others were held constant. Once the optimal value was identified, it was fixed for the following steps. This process was repeated to assess the influence of each parameter on printability independently.

Each of the above-mentioned parameters were optimized independently in the following manner:

- **Parameter 1: Slag-to-binder ratio (BFS/b)** - As the primary parameter defining binder composition, BFS/b was varied from 0.2 to 0.8 in increments of 0.1. During this optimization, the remaining parameters were held constant: w/b at 0.4, Na_2O/b at 4%, and SiO_2/Na_2O at 0.5. This range encompasses compositions from FA-dominated to BFS-dominated systems, allowing identification of the optimal balance between the two precursors.

- **Parameter 2: Alkali content (Na_2O/b %)** - With the optimal BFS/b ratio established, the alkali content was varied from 4% to 5.5% in increments of 0.5%. The previously optimized BFS/b was maintained, while w/b remained at 0.4 and SiO_2/Na_2O at 0.5. This range was selected to provide sufficient activation while avoiding excessive alkalinity that could compromise workability.

- **Parameter 3: Activator modulus (SiO_2/Na_2O)** - The silicate-to-hydroxide ratio was adjusted between 0.45 and 0.6 in the increments of 0.05. The previously optimized BFS/b and Na_2O/b values were fixed, with w/b maintained at 0.4. This narrow range focuses on moduli known to provide optimal activation kinetics for slag-based systems.

- **Parameter 4: Water-to-binder ratio (w/b)** - As the final optimization step, w/b was fine-tuned between 0.36 and 0.4 to achieve the target rheological properties. All previously optimized parameters (BFS/b, Na_2O/b, and SiO_2/Na_2O) were held constant. This final adjustment ensures optimal workability without compromising the established chemical composition.

The details of tested mix parameter values for reference mix are outlined in Table *4.1*.

Table 4.1 Parameters tested for development of reference mix.

Varied Parameter	**Start Point**	**Step Size**	**Constant Parameters**	**Optimised**
BFS/b	0.1	0.1	Na_2O/b – 4%; SiO_2/Na_2O – 0.5; w/b – 0.4	-
Na_2O/b	4%	0.5	SiO_2/Na_2O – 0.5; w/b – 0.4	BFS/b
SiO_2/Na_2O	0.5	0.05	w/b – 0.4	BFS/b;Na_2O/b
w/b	0.4	0.02	-	BFS/b;Na_2O/b;SiO_2/Na_2O

4.2.2 Optimization of slag-to-binder ratio for Buildability and Flowability

To optimise the BFS and FA compositions, slump and slump-flow tests were performed on mortar mixes with varying slag-to-binder ratios (BFS/b). In these mixes, the total binder mass (b) refers to the combined mass of BFS and FA. The corresponding results, measured immediately after mixing (within 5 minutes), are shown in Figure X and Figure Y. The BFS/b ratio was varied from 0.2 to 0.8 while maintaining a w/b constant at 0.4, Na_2O/b at 4% and activator modulus at 0.5.

From the figures, it can be observed that the slump and slump-flow values increased consistently with increasing BFS/b ratio. This means that the flowability of the mix improved as the slag content increased relative to fly ash. This observed trend contradicts conventional expectations. Fly ash particles, with their spherical morphology and smooth surface texture, are typically known to enhance flowability when incorporated into mortar mixes. Therefore, reducing the fly ash content would normally be expected to decrease flowability. However, the results demonstrate the opposite effect.

This behaviour aligns with findings reported in previous studies [85], which demonstrated that flowability trends in alkali-activated systems are strongly dependent on activators. In systems activated with only sodium hydroxide (modulus = 0), flowability decreases with decreasing fly ash content, following the expected trend. However, when sodium silicate is incorporated into the activator (modulus > 0), flowability improved with higher slag content and reduced fly ash content [85]. This implies that the water glass content governs the slump and slump flow behaviour, resulting in improved flowability with higher slag content despite the reduction in spherical fly ash particles.

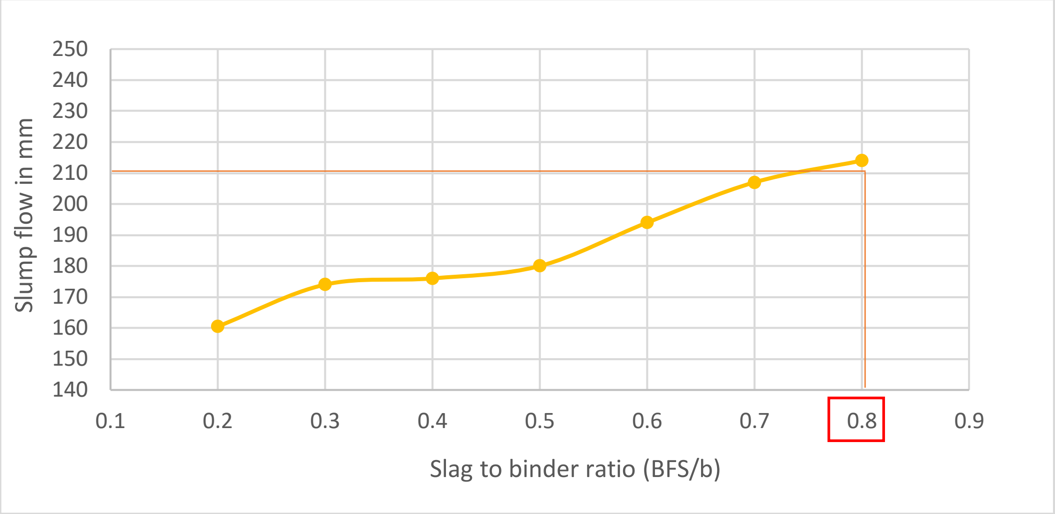

(a)

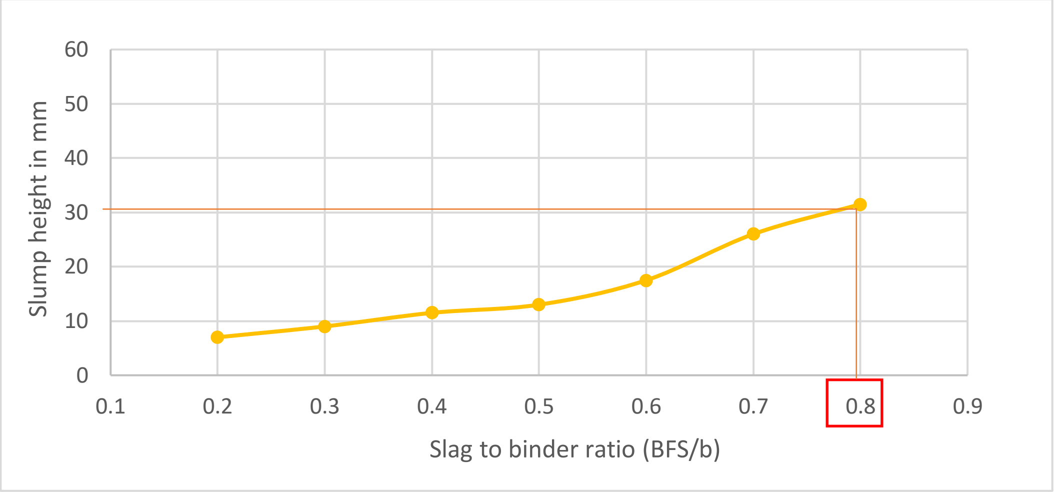

(b)

Figure 4.2 (a) Slump flow and (b) slump height with varying BFS/b ratios.

From the Figure *4.2* it can be observed that the mix with BFS/b ratio of 0.8 achieved slump and slump flow values within the target ranges established in Table *3.5*. This composition was therefore selected as the optimal binder proportion for the reference mix. This combination yielded a slump of approximately 31.5 mm and a slump-flow of about 214 mm, which falls within the initial target ranges of 15–30 mm for slump and 210–240 mm for slump-flow [64], as stated in Section 3.7.1.2. These values were found to be well-suited for 3D printing applications.

This composition was therefore selected as the optimal binder proportion for the reference mix. To ensure final target slump and flow values requirements are met, this mix will undergo extended testing over 2 hours in conjunction with alkali content optimization, as detailed in the following section.

4.2.3 Optimisation of alkali content for Buildability and Flowability

With the optimal binder proportion established at BFS/b = 0.8, the next parameter investigated was the alkali content (Na_2O/b). Following the stepwise optimization approach, the previously optimized BFS/b ratio was maintained constant along with SiO_2/Na_2O at 0.5 and w/b at 0.4. The Na_2O/b was varied from 4% to 5.5% in increments of 0.5% to determine the optimal alkali dosage. Mini slump and slump flow tests were performed immediately after mixing and at 20-

minute intervals up to 2 hours to evaluate the evolution of buildability and flowability over time as illustrated in Figure *4.3*.

The results show that the mixes with higher Na_2O/b content exhibited lower slump and slump-flow values and consistently decreased over time. This trend can be attributed to the increased concentration of OH^- ions at higher alkali dosages, which accelerates the dissolution of aluminosilicate precursors and promotes early polymerization reactions [60].

For 3D printing applications, the mixture needs to exhibit lower slump values over time to ensure proper buildability, while maintaining sufficient flowability for pumping. Mixes with Na_2O/b ranging from 4% to 5% successfully met both initial and final target values for buildability and flowability. In contrast, the mix with 5.5% Na_2O/b experienced excessive workability loss, with final values falling outside the acceptable ranges. Among the compositions meeting the printability criteria, the mix with 5% Na_2O/b achieved the optimal balance between buildability and flowability. This composition exhibited enhanced buildability (lower slump values) while maintaining flowability comparable to the 4% and 4.5% mixes. Based on these results, Na_2O/b = 5% was selected and carried forward for activator modulus optimization.

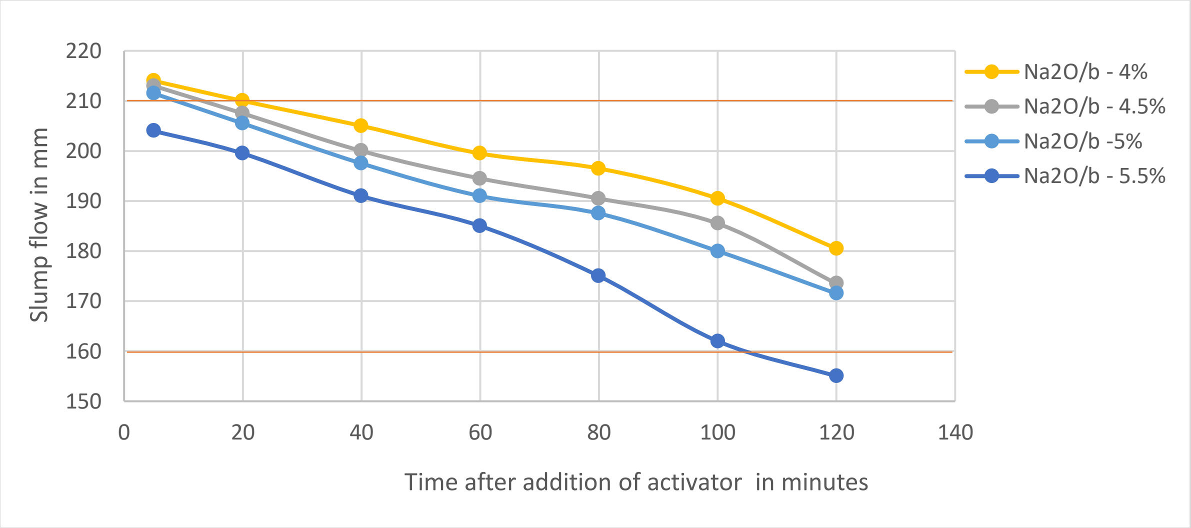

(a)

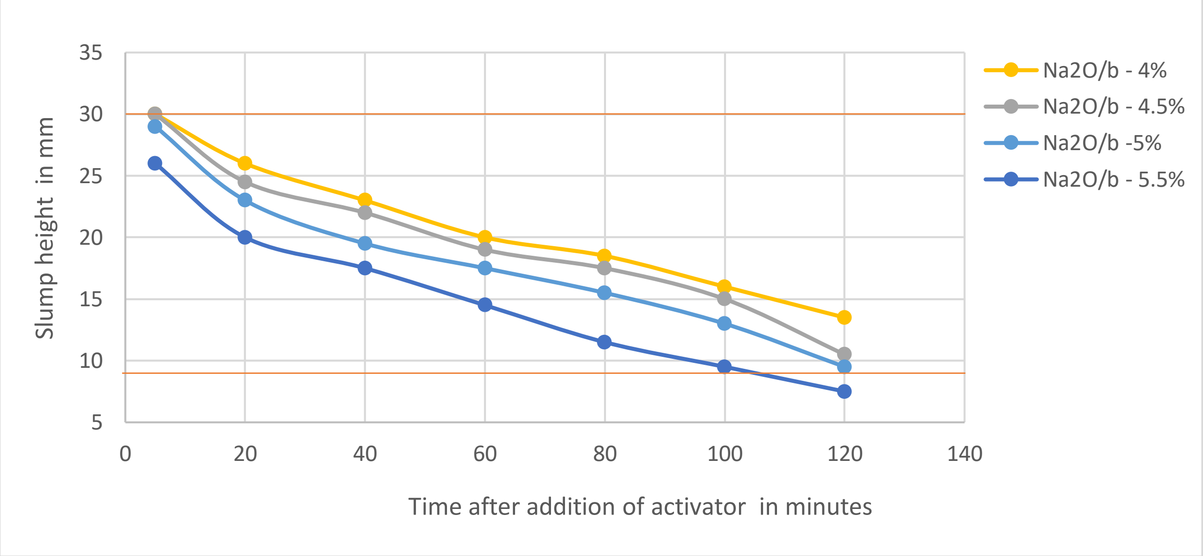

(b)

Figure 4.3 (a) Slump flow and (b) slump height with varying Na_2O /b.

4.2.4 Optimisation of activator modulus for Buildability and Flowability

With BFS/b fixed at 0.8 and Na_2O/b at 5%, the activator modulus (SiO_2/Na_2O) was varied to optimize the activator chemistry. The modulus was adjusted from 0.45 to 0.6 while maintaining w/b at 0.4.

Figure *4.4* presents the effect of activator modulus on slump and slump flow over time. The results show that increasing the SiO_2/Na_2O modulus led to higher slump and slump flow values. This trend can be attributed to the lower pH of the activator at higher modulus values [85], [86], which reduces the initial dissolution rate of precursors and increases the slump height and flow values.

The mix with modulus 0.45 exhibited the lowest values and failed to meet the final target ranges after 2 hours, with excessive workability loss rendering it unsuitable for printing applications. Mixes with modulus between 0.5-0.6 satisfied the initial and final target values. However, the higher modulus > 0.5 resulted in reduced buildability, as evidenced by higher slump values throughout the testing period.

The mix with SiO_2/Na_2O modulus 0.5 demonstrated optimal performance, achieving initial slump of 29 mm and slump flow of 211.5 mm, with final values of 9.5 mm and 171.5 mm respectively. This composition provided the best balance between buildability and controlled flowability. Therefore, activator modulus of 0.5 was selected for the reference mix formulation and carried forward for water content optimization.

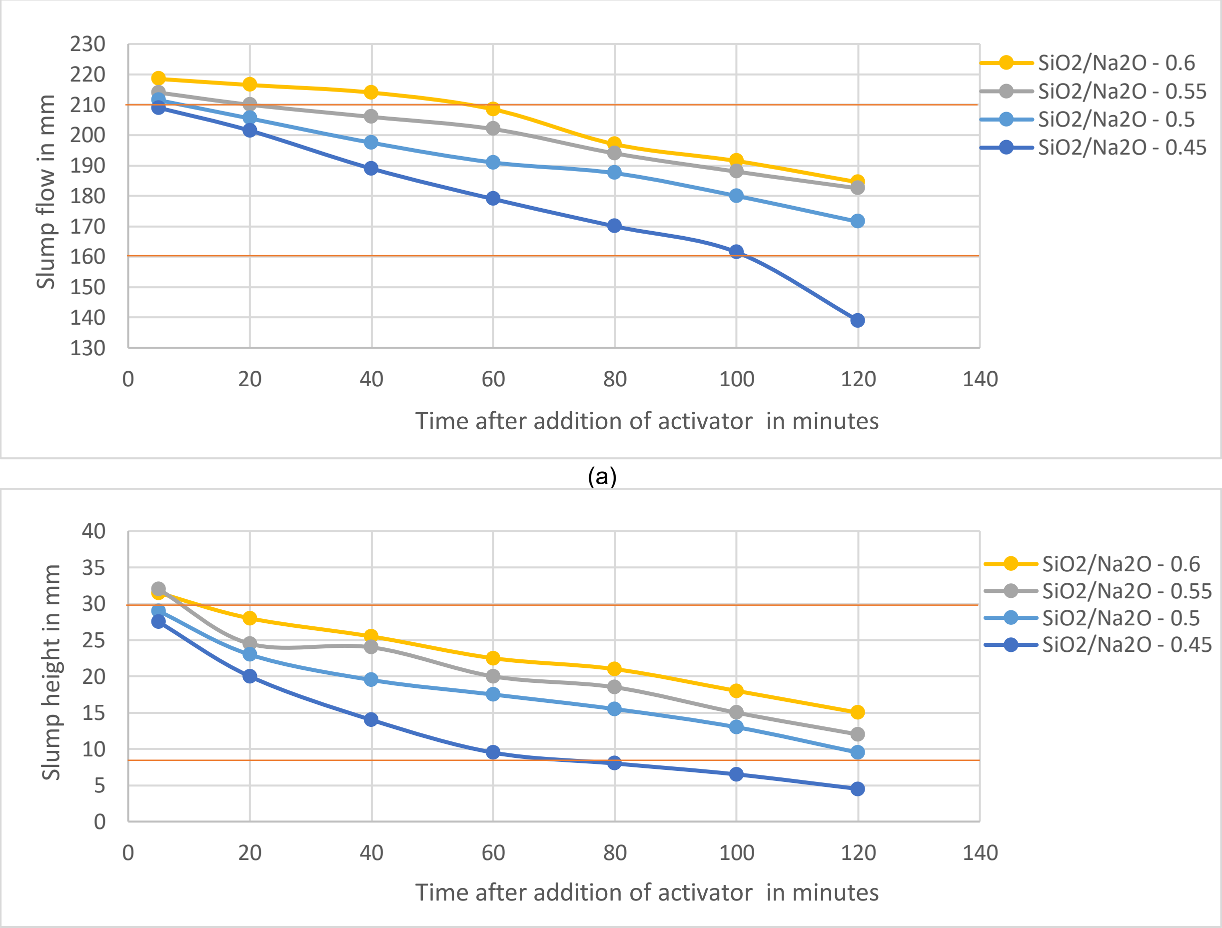

(a)

(b)

Figure 4.4 (a) Slump flow and (b) slump height with varying SiO_2/Na_2O modulus.

4.2.5 Optimization of water to binder ratio for buildability and flowability

With the binder composition and activator parameters established (BFS/b = 0.8, Na_2O/b = 5%, SiO_2/Na_2O = 0.5), the final optimization step focused on the water-to-binder ratio. The w/b was varied from 0.36 to 0.4 to eliminate excess water and prevent bleeding while maintaining adequate workability.

Figure 4.5 shows the influence of w/b on slump and slump flow over time. As the water-to-binder ratio increased, both slump and slump flow improved. Increasing the water-to-binder ratio enhanced both slump and slump flow values due to two primary mechanisms: dilution of the alkaline activator, which reduces the rate of early dissolution [87], [88], and decreased interparticle friction [89], which improves flowability.

The mix with w/b ratio 0.36 had insufficient amount of water required for adequate wetting of particles. Conversely, the mix with w/b 0.4 had excess amount of water than required. The intermediate w/b ratio of 0.38 was identified as optimal, striking a balance between flowability and buildability was selected.

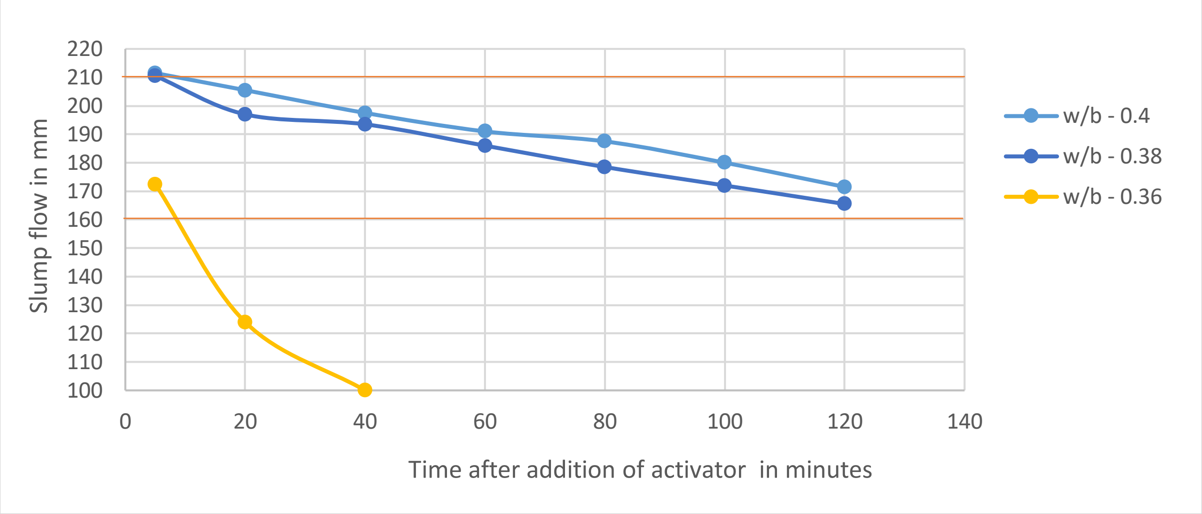

(a)

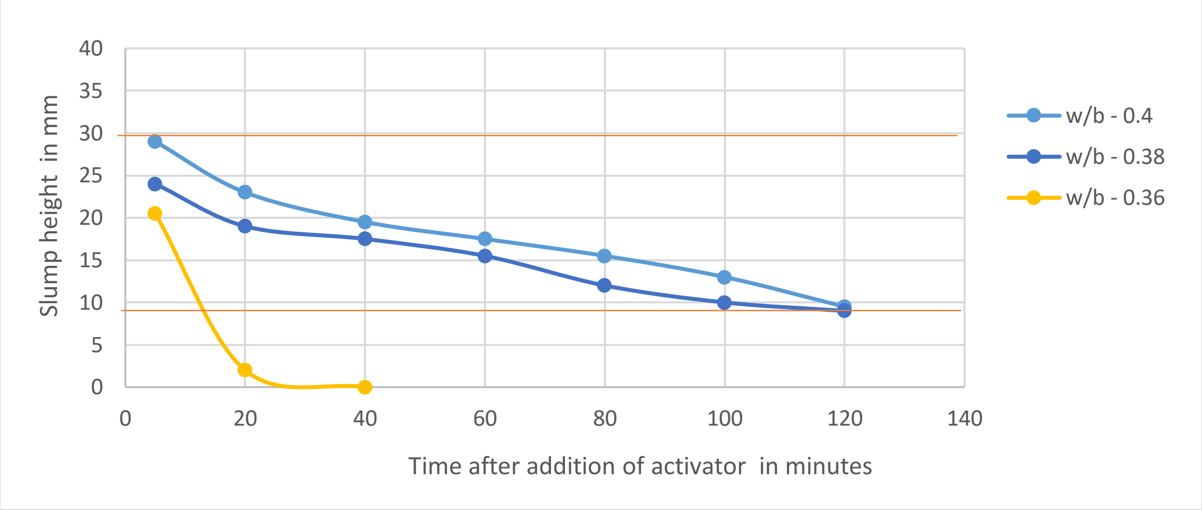

(b)

Figure 4.5 (a) Slump flow and (b) slump height with varying w/b.

Based on these results, w/b = 0.38 was selected for the final reference mix formulation. The optimized reference mix composition therefore comprises: BFS/b = 0.8, Na_2O/b = 5%, SiO_2/Na_2O = 0.5, and w/b = 0.38.

4.3 Summary of the optimized reference mix composition

Through the systematic stepwise optimization approach, the reference mix composition was established by sequentially optimizing each parameter while monitoring buildability and flowability. Table *4.2* presents the final composition of this reference mix (20FA-BFS_0.38), where the notation indicates 20% fly ash content with blast furnace slag at a water-to-binder ratio of 0.38.

Table 4.2 Developed reference mix composition (20FA-BFS_0.38).

Parameter	**Reference Mix**
Precursor	**Slag - 80% and Fly Ash - 20%**
SiO_2 / Na_2O	**0.5**
Na_2O/b	**5%**
Water/binder	**0.38**
Sand/binder	**1.5**

The developed reference mix successfully met the buildability and flowability criteria, with initial values (at 5 minutes) achieving slump height of 24 mm (target: 15-30 mm) and slump flow of 210.5 mm (target: 210-240 mm), while maintaining acceptable final values (at 120 minutes) of 9 mm slump height (target: 8 mm) and 165.5 mm slump flow (target: 160 mm). This formulation serves as the baseline for developing the target mix incorporating MSWI bottom ash in the following section.

4.4 Development of target mix through optimization of Buildability and Flowability

4.4.1 Test Approach for Mini Slump and Slump flow to optimize buildability and flowability of Reference Mix

The target mix was developed using MSWI bottom ash as a replacement for fly ash. The developed Reference mix composition is considered as the starting point for target mix. The mix proportions of the target mix were optimised to match the slump and slump flow of the reference mix in order to achieve a comparable buildability and flowability as the reference mix.

4.4.2 Optimization of Water-to-Binder Ratio for buildability and flowability of Target Mix

The target mix was developed by replacing fly ash with MSWI bottom ash (BA) at 20% of the total binder content. Using the optimized reference mix as the baseline, all parameters were maintained constant (BFS/b = 0.8, Na_2O/b = 5%, SiO_2/Na_2O = 0.5) varying the water to binder.

Figure *4.6* presents the slump and slump flow for the bottom ash mix with varying w/b ratios. The bottom ash mix with w/b of 0.38 resulted in inadequate workability. Increasing the water content to w/b = 0.40 enabled the bottom ash mix (20BA-BFS_0.40) to achieve similar slump and slump flow as the reference mix (20FA-BFS_0.38) as shown in Figure *4.7*. This increased water demand is attributed to the morphological differences between MSWI BA and fly ash. As observed in section 3.2.2 and section 3.3, MSWI BA particles possess irregular, angular morphology and finer particle size distribution compared to the spherical fly ash particles. The average particle size of MSWI BA (D_{50} = 6.99 µm) is 6 times finer than that of spherical fly ash particles (d50 = 45.39 µm). These characteristics result in higher specific surface area and increased interparticle friction, thereby requiring additional water to achieve equivalent buildability and flowability as reference mix.

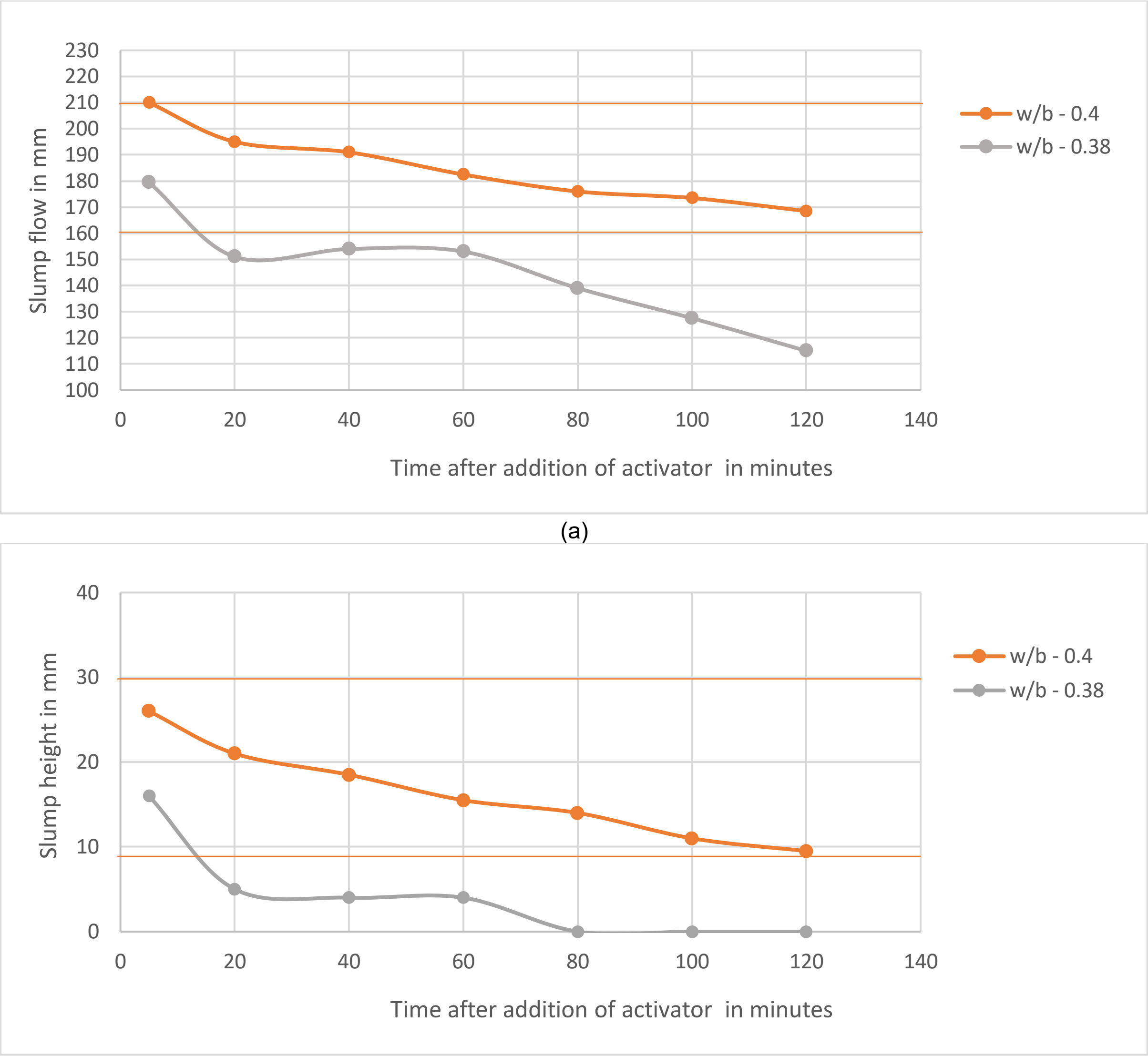

(a)

(b)

Figure 4.6 (a) Slump flow and (b) slump height with varying w/b ratio.

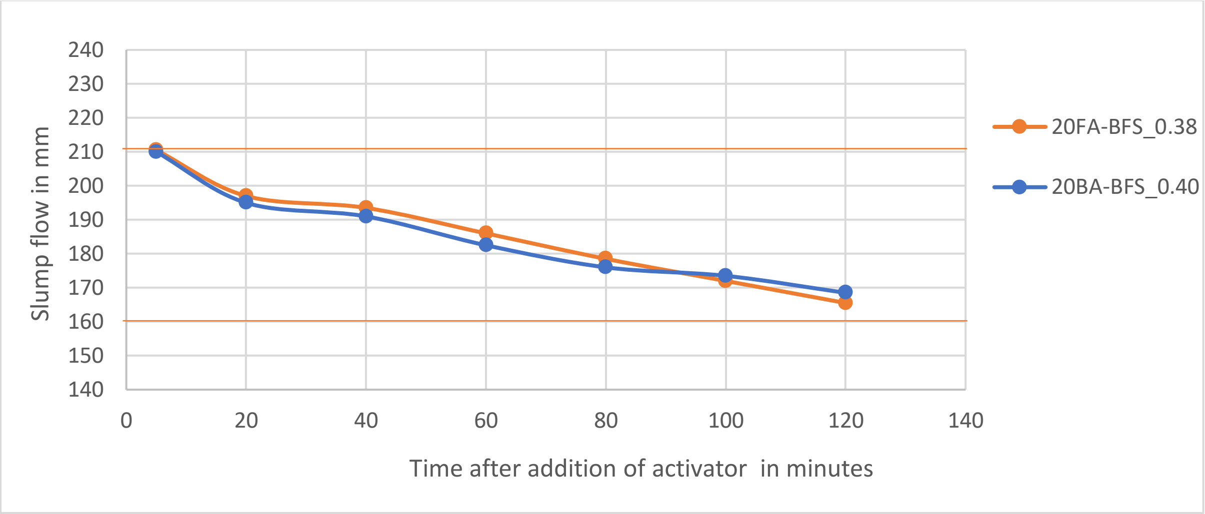

(a)

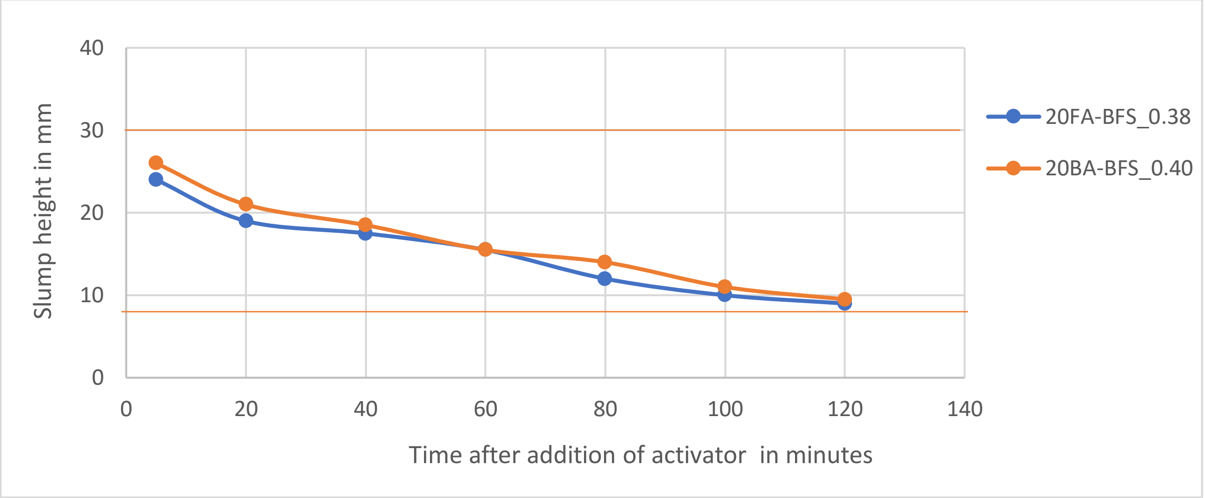

(b)

Figure 4.7 (a) Slump flow and (b) slump height of final reference mix and target mix.

4.4.3 Summary of Optimized Target Mix Composition

The target mix incorporating MSWI bottom ash was successfully developed through adjustment of the water-to-binder ratio while maintaining all other parameters from the reference mix. Table 4.4 presents the final composition of the target mix (20BA-BFS_0.40), where the notation indicates 20% bottom ash content with blast furnace slag at a water-to-binder ratio of 0.40.

Table 4.3 Developed target mix composition (20BA-BFS_0.4).

Parameter	**Reference Mix**
Precursor	**Slag - 80% and MSWI BA - 20%**
SiO_2 / Na_2O	**0.5**
Na_2O/b	**5%**
Water/binder	**0.4**
Sand/binder	**1.5**

The 20BA-BFS_0.40 mix achieved slump and slump flow values similar to the reference mix (20FA-BFS_0.38), with initial values of 26 mm slump height and 210 mm slump flow, and final values of 9.5 mm and 168.5 mm respectively. The Target mix was successfully developed meeting the buildability and flowability criteria.

4.5 Mini Extrudability Test on Developed

Following the optimization of buildability and flowability, both the reference mix (20FA-BFS_0.38) and target mix (20BA-BFS_0.40) were subjected to mini extrudability testing to validate their suitability for extrusion-based 3D printing. Figure *4.8* shows the extrudability test results for both mixes.

(a) (b)

Figure 4.8 Mini extrudability test conducted on (a) reference mix (20FA-BFS_0.38) and (b) target mix (20BA-BFS_0.40).

The extruded filaments from both the reference mix (20FA-BFS_0.38) and target mix (20BA-BFS_0.40) exhibited smooth, continuous surfaces without any tearing or surface imperfections. When extruded in a layer-by-layer manner, both mixtures maintained dimensional stability with no observable deformations. The extrusion process produced uniform filaments that retained their circular cross-section without significant shape loss. These results successfully confirm the extrudability of both developed mixtures and validate that they meet the stability requirements essential for layer-by-layer construction in 3D printing applications.

4.6 Setting time of developed reference and target mixes

The setting time of both optimized mixes was determined using the Vicat test to ensure adequate open time for 3D printing. Figure *4.9* presents the setting time results for the reference mix (20FA-BFS_0.38), target mix (20BA-BFS_0.40), and an additional control mix with matched water content (20FA-BFS_0.40) for comparative analysis.

The developed reference and target mixes satisfied the target setting time of 90 minutes, providing sufficient open time for printing operations. The reference mix (20FA-BFS_0.38) exhibited an initial setting time of 90 minutes, while increasing the water content to 0.40 (20FA-BFS_0.40) extended the setting time to 116 minutes. This can be attributed to the dilution effect of additional water, which reduces the alkalinity of the activating solution and subsequently decreases dissolution rate [87], [88].

The target mix (20BA-BFS_0.40) demonstrated the longest setting time at 146 minutes, significantly exceeding both FA-based mixes. When compared to the mix with identical water content (20FA-BFS_0.40), the incorporation of MSWI BA extended the setting time by approximately 30 minutes. This difference in setting times between 20FA-BFS_0.40 and 20BA-BFS_0.40 indicates that the delay was inherently caused by MSWI BA. This can potentially mean that the MSWI BA has caused slower reaction kinetics. This extended setting time in 20BA-BFS_0.40 provides a longer operational window for printing applications.

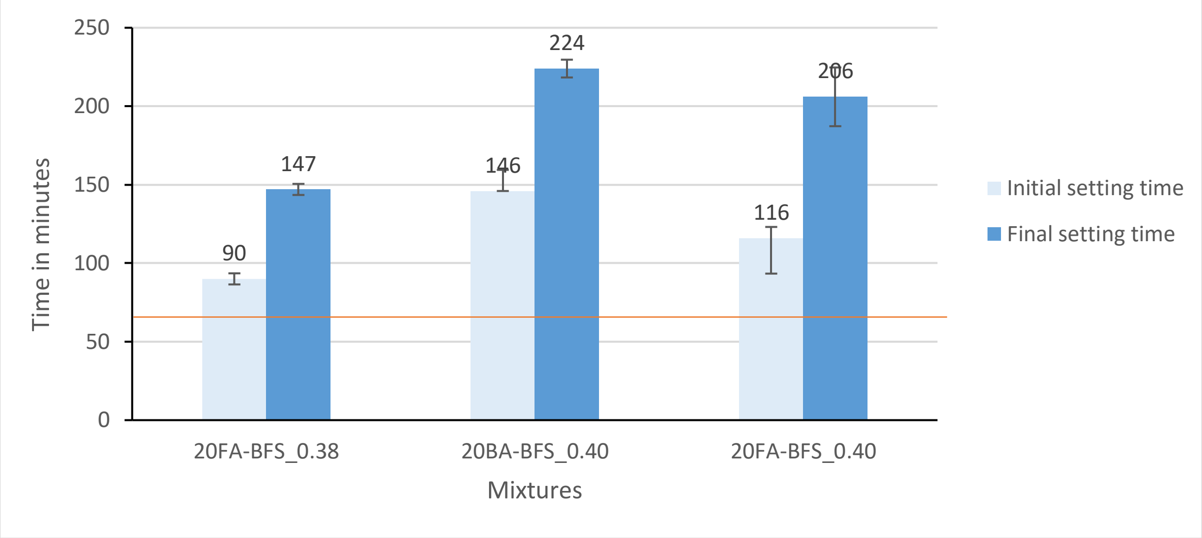

Figure 4.9 Initial and final setting times.

4.7 Mechanical strength

Compressive and flexural strength tests were conducted at 1, 7, and 28 days to validate the mechanical performance of the developed reference mix (20FA-BFS_0.38) and target mix (20BA-BFS_0.4). Additionally, a control mix (20FA-BFS_0.4) with water content matching the target mix was tested to isolate the effect of MSWI BA from the water content effect. Figure *4.10* and Figure *4.11* present the strength development profiles for all three mixes.

The compressive and flexural strength results demonstrated a clear strength hierarchy: 20FA-BFS_0.38 > 20FA-BFS_0.4 > 20BA-BFS_0.4 at all ages. The 28-day compressive strength values were 58.6 MPa, 52.2 MPa, and 48.0 MPa respectively. The 28-day mould cast specimens of both the reference mix (20FA-BFS_0.38) and target mix (20BA-BFS_0.4) exceeded the required 3D printing strength criteria of 45 MPa compressive and 9 MPa flexural strength, as indicated in Figure *4.10* and Figure *4.11* respectively.

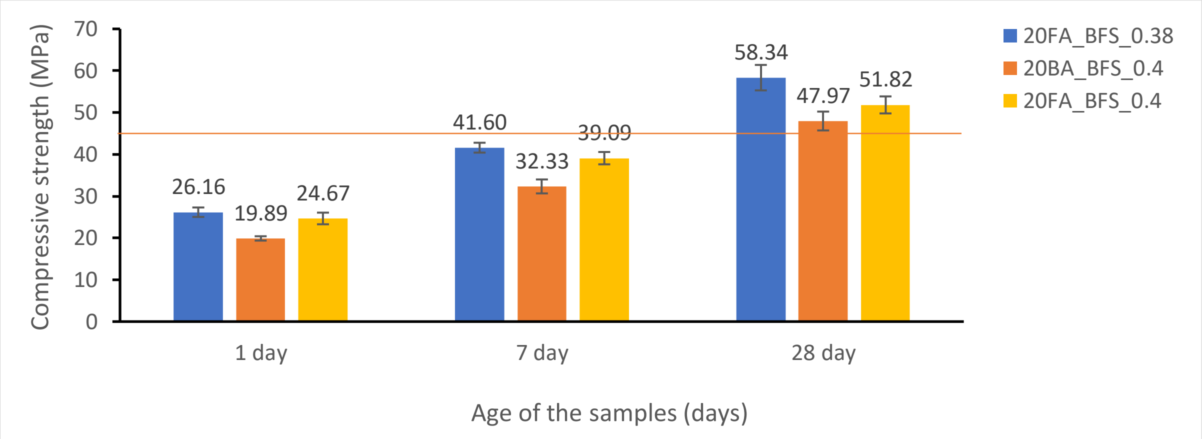

Figure 4.10 Compressive strength.

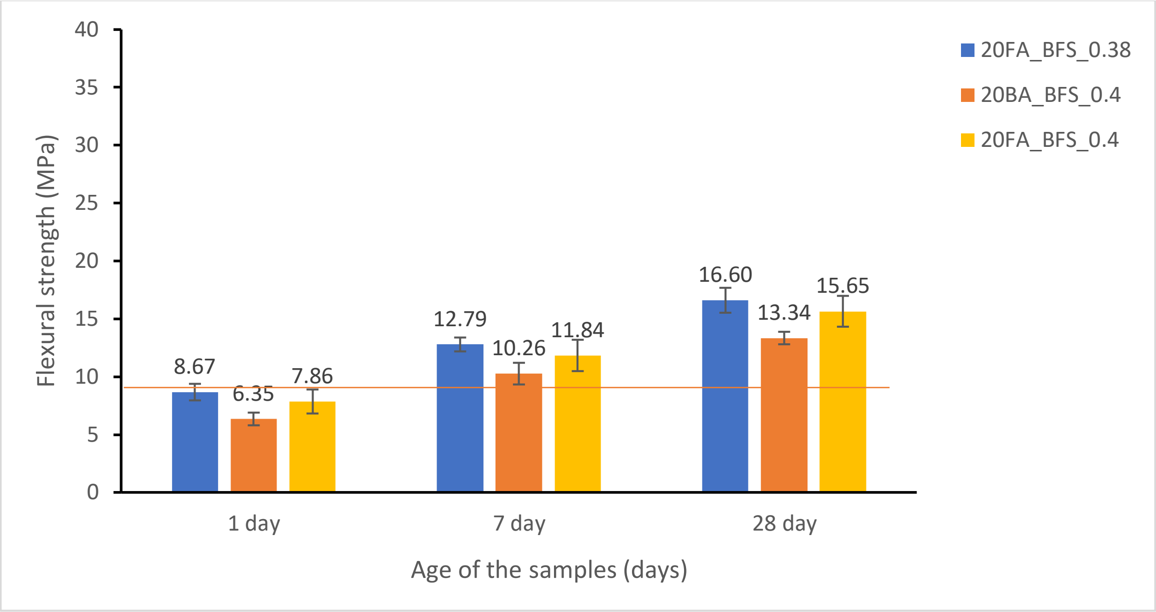

Figure 4.11 Flexural strength.

Early strength development was substantial for reference (20FA-BFS_0.38) and target (20BA-BFS_0.4) mixes, with approximately 60-65% of the 28-day compressive strength achieved by 7 days. Similarly, flexural strength showed rapid early development, reaching 75-77% of the 28-day values by 7 days. This early strength gain is crucial for 3D printing applications, ensuring adequate support for subsequently deposited layers.

Comparison between mixes with identical water content (20BA-BFS_0.40 vs. 20FA-BFS_0.40) reveals that MSWI BA incorporation reduced 28-day compressive strength by approximately 8% and flexural strength by 15%, demonstrating the direct effect of MSWI BA independent of water content. The overall strength reduction of the target mix compared to the reference mix was approximately 18% for compressive strength and 22% for flexural strength. This reduction in strength of 20BA-BFS_0.40 mix can be attributed to combined effect of two factors: higher water content leading to increased porosity [88], and the slower reaction kinetics of MSWI BA compared to fly ash, as evidenced by the extended setting times.

Despite the strength reduction, the target mix (20BA-BFS_0.40) achieved 28-day compressive strength of 47.97 MPa and flexural strength of 13.34 MPa, exceeding the target values of 45 MPa and 9 MPa respectively as indicated in Figure *4.10* and Figure *4.11*. These results confirm that MSWI BA can successfully replace fly ash in printable alkali-activated mortars while maintaining mechanical properties suitable for structural applications.

4.8 Conclusion

This chapter presented the systematic development and optimization of alkali-activated mortar composition for extrusion-based 3D printing applications. A reference mix using BFS and FA was first established through stepwise parametric optimization, followed by the development of a target mix incorporating MSWI BA as a sustainable replacement for fly ash. The effects of MSWI BA on printability, setting behaviour, and mechanical properties were comprehensively investigated. The main findings are:

- **Reference mix development:** A 3D printable reference mix (20FA-BFS_0.38) was successfully developed through systematic parametric optimization. The optimized composition comprised BFS/b = 0.8, Na_2O/b = 5%, SiO_2/Na_2O = 0.5, and w/b = 0.38, demonstrating adequate printability.

- **Successful MSWI BA incorporation:** The target mix (20BA-BFS_0.40) was developed by replacing fly ash with MSWI BA at 20% of total binder content. The irregular morphology and finer particle size of MSWI BA necessitated a 5% increase in water content (from 0.38 to 0.40) to achieve comparable printability as the reference mix.
- **Printability performance:** The 20FA-BFS_0.38 and 20BA-BFS_0.40 mixes demonstrated excellent performance across all printability criteria. The mixes exhibited appropriate buildability and flowability based on slump and slump flow testing, produced continuous filaments without blockage or shape loss during extrusion, achieved the setting time requirement of 90 minutes, and required mechanical properties. The longer setting time in 20BA-BFS_0.40 provides an operational advantage for 3D printing applications, allowing more flexibility during the printing process without compromising on buildability and flowability.
- **Slower reaction kinetics of MSWI BA:** A key finding is the consistently slower reaction kinetics exhibited by MSWI BA compared to fly ash. This was evidenced by: (i) extended initial setting time of 146 minutes versus 116 minutes for FA mix with identical water content; and (ii) reduced early strength development, with 1-day and 7-day strengths approximately 25% and 22% lower respectively. These results collectively demonstrate the slower reaction caused by MSWI BA in alkali-activated systems.
- **Adequate structural performance:** Despite slower reaction kinetics, the target mix achieved 28-day compressive strength of 47.97 MPa and flexural strength of 13.34 MPa, exceeding the 3D printing requirements of 45 MPa and 9 MPa respectively. While approximately 18% lower than the reference mix, these values confirm that MSWI BA-based formulations provide sufficient mechanical properties for structural applications.

The successful development of both formulations validates that MSWI BA can effectively replace fly ash in printable alkali-activated mortars with appropriate mix design adjustments. The combination of equivalent printability, extended working time, and adequate mechanical properties demonstrates the feasibility of incorporating industrial waste materials in additive manufacturing without compromising critical performance requirements.

5

Early-age Reaction Kinetics of Developed mixtures

5.1 Introduction

The successful implementation of extrusion-based 3D concrete printing technology requires a fundamental understanding of the early-age reaction kinetics that govern the rheological behaviour and microstructural evolution of printable alkali-activated mortars. In this context, reaction kinetics at early ages directly influence key printing parameters such as pumpability, extrudability, and buildability. Therefore, an in-depth analysis of how these reactions evolve within the printable window is critical for optimizing performance and ensuring consistent print quality.

This chapter examines the evolution of rheology and the microstructure during the early stages of alkali-activation of the two 3D printable mixes developed in Chapter 4. The two printable mixes developed are: the reference mixture (20FA-BFS_0.38) containing fly ash, and the target mixture (20BA-BFS_0.4) in which fly ash is replaced with MSWI bottom ash. The primary objective is to determine how substitution of fly ash with MSWI bottom ash influences early-age reaction kinetics, affecting rheological performance and the printability window of the mortar.

To achieve this objective, the early-age reactions and their effects on rheology and microstructure of these two mixtures were investigated in four steps. The Figure *5.1* provides a visual overview of the steps followed in this chapter for investigation. The steps include:

1. Yield Stress Evolution through Slugs test: Determination of yield stress development with time, providing insights into rheological structuration the progressive formation of the percolated particle network and printable window.

2. Pore Solution Analysis through ICP-OES: This method quantifies elemental concentrations (Na, Si, Ca, Al, Mg) in the pore solution, offering crucial data on chemical reaction kinetics and precursor dissolution.

3. Thermodynamic Modelling of Pore solution through GEMS: Due to experimental challenges in directly identifying early-age gels present in trace amounts, thermodynamic modelling was performed. Using pore solution data from ICP-OES as input, the precipitation of solid phases is predicted from modelling. This provides a theoretical basis for interpreting and validating experimental observations.

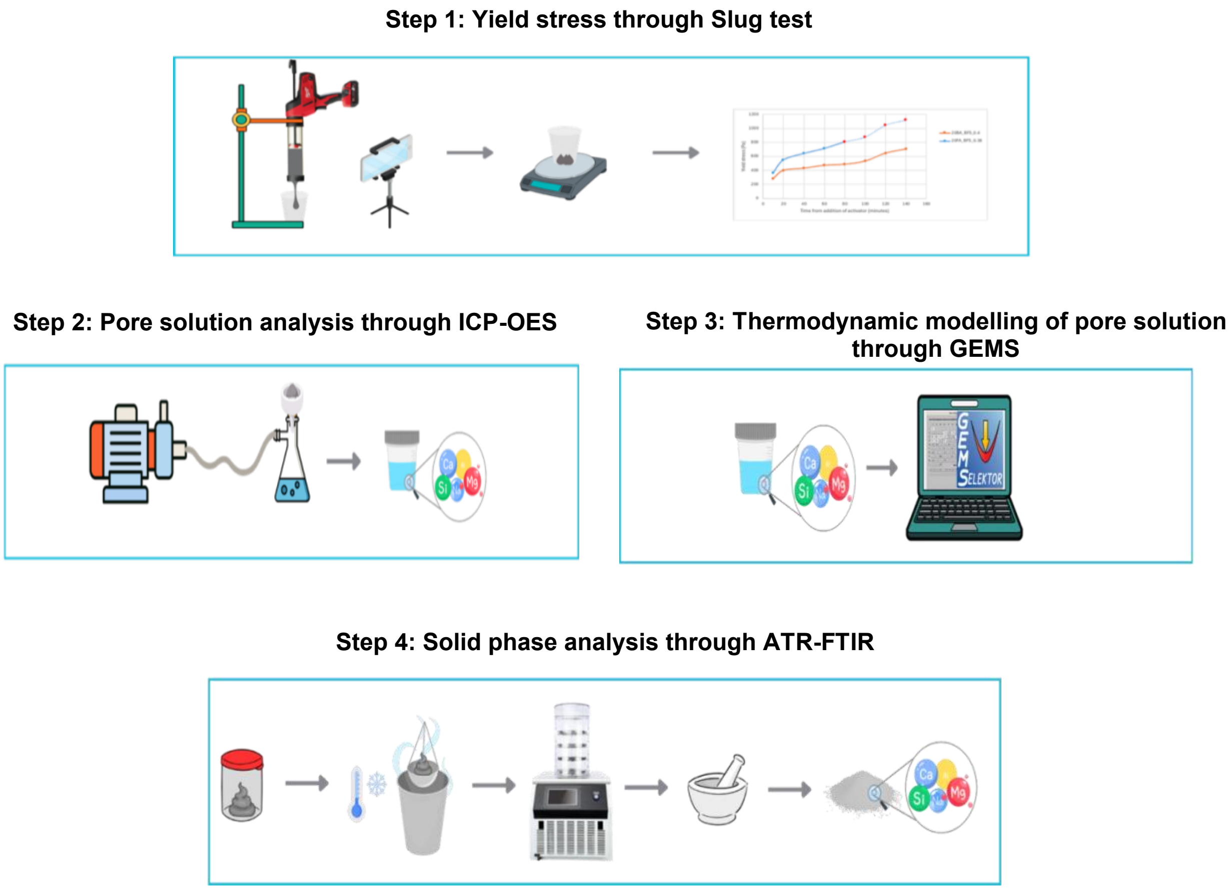

Figure 5.1 Overview of the steps followed for investigation

4. Solid Phase Analysis through ATR-FTIR: FTIR spectroscopy helps identify the formation of reaction products and tracks chemical bond evolution within the solid phases, confirming microstructural evolution and product formation at early ages. It complements and validates findings from thermodynamic modelling and pore solution analysis.

These steps provide complementary insights and facilitate a comprehensive understanding of MSWI bottom ash's impact on rheology and early-age reaction kinetics.

5.2 Yield Stress Evolution by Slugs Test

The yield stress in cementitious materials originates from attractive interparticle forces within flocculated particle networks formed immediately after mixing [20], [89]. A flow is initiated when applied stress exceeds the strength of these particle networks, causing structural breakdown [20]. Due to ongoing chemical reactions, such as the formation of early reaction products, yield stress typically increases over time, causing irreversible stiffening and reduced workability [89].

The evolution of static yield stress over a period of 140 minutes was assessed for the mixes 20FA-BFS_0.38 and 20BA-BFS_0.4 using the slugs test, as illustrated in Figure *5.2*. Complete time-series images documenting slug formation at 20-minute intervals for the reference mix (20FA-BFS_0.38) and target mix (20BA-BFS_0.4) are provided in Figure A.*1* and Figure A.*2* of Appendix A, respectively. The goal of this test was to evaluate their rheological performance for extrusion-based 3D printing.

For extrusion-based 3D concrete printing, yield stress must balance conflicting requirements: sufficiently low to facilitate pumping and extrusion, yet adequately high to ensure shape stability and buildability post-extrusion [6]. Literature suggests an optimal yield stress range for printable alkali-activated mortars between 400 – 1000 Pa [6], balancing the contradictory demands of pumping ease and structural retention. Additionally, the minimum initial yield stress (τ_i) required to prevent deformation due to self-weight is calculated based on mortar density (ρ), gravity (g) and layer thickness (h) of 10 mm using the following equation [72], [90]:

$$\tau_i = \frac{\rho g h}{\sqrt{3}} \quad \text{(Eq. 5.1)}$$

The required initial yield stress of 20BA-BFS_0.4 mix (τ_{iBA}) with density (ρ_{BA}) of 2200 kg/m³ is:

$$\tau_{iBA} = \frac{\rho_{BA} g h}{\sqrt{3}} = \frac{2200\times 9.81 \times 0.01}{\sqrt{3}} = 124.6\,Pa \approx 125\,Pa \quad \text{(Eq. 5.2)}$$

The required initial yield stress of 20FA-BFS_0.4 mix (τ_{iFA}) with density (ρ_{FA}) of 2220 kg/m³ is:

$$\tau_{iFA} = \frac{\rho_{FA} g h}{\sqrt{3}} = 125.7\,Pa \approx 126\,Pa \quad \text{(Eq. 5.3)}$$

Both mortar mixes, 20FA-BFS_0.38 and 20BA-BFS_0.4, satisfy their respective minimum initial yield stress requirement and also exhibit the yield stress values within 400 – 1000 Pa range throughout the test period. However, distinct differences were observed in the rate and progression of structuration between the two mixes. For 20FA-BFS_0.38, the yield stress rises sharply and reaches 807 Pa at 80 minutes, after which slug formation ceases and a brittle discontinuity is observed. This brittle discontinuity is indicative of a fracture-type mechanism, wherein material becomes excessively stiff and has high yield stresses. As depicted in Figure *5.3*, this transition marks the limit of the slug test, which only yields reliable quantitative results under necking or slug-by-slug deformation. Beyond this point, values for 20FA-BFS_0.38 represent qualitative indicators rather than true yield stress. Notably, this rheological transition coincides with the measured initial setting time of 90 minutes of the 20FA-BFS_0.38 mix.

In contrast, 20BA-BFS_0.4 maintains continuous slug formation throughout the entire test period, as demonstrated in Figure *5.4*. Its yield stress evolves more gradually, reaching 703 Pa at 140 minutes, and remains within the printable range without brittle failure. This difference reflects underlying variations in early-age reaction kinetics especially implying a slower rate in the MSWI BA mix. As a result, the development of a rigid percolated network is delayed, and the system retains its deformable structure for a longer period. Therefore, the prolonged workability observed in the 20BA-BFS_0.4 mix can be attributed to the interplay between reaction kinetics and particle dispersion mechanisms [91]. This extended printable window is advantageous for 3D printing tasks that involve longer pumping or staging intervals.

In summary, although both mixtures initially fall within the printable yield stress range, the BA-based system has prolonged open time, enhanced extrudability, and potentially lower pumping pressures. Its delayed transition to brittle discontinuity makes it a more robust candidate for 3D concrete printing, particularly for applications where time-dependent stability is crucial.

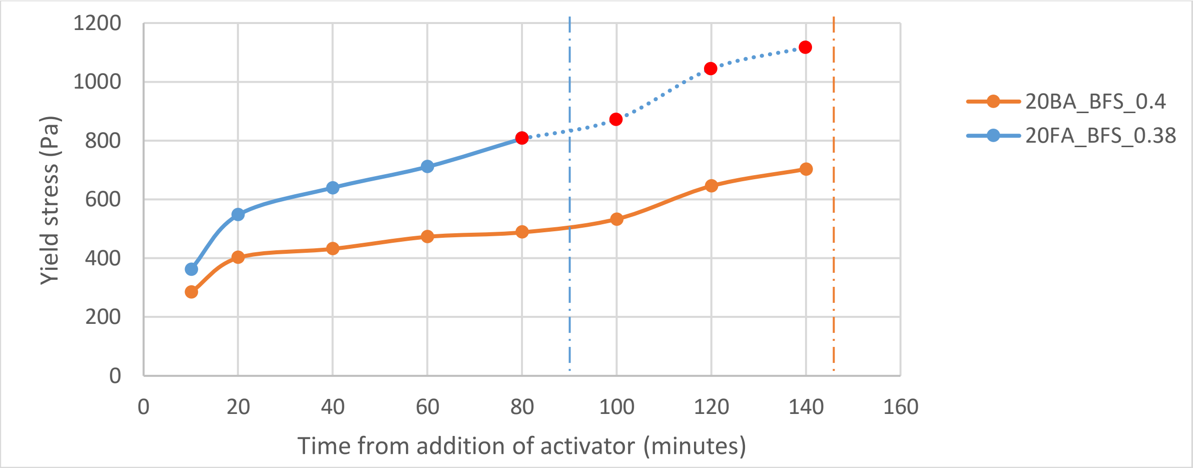

Figure 5.2 Evolution of static yield stress over time for 20FA-BFS_0.38 and 20BA-BFS_0.4 mixes with blue and red dotted lines representing respective initial setting times.

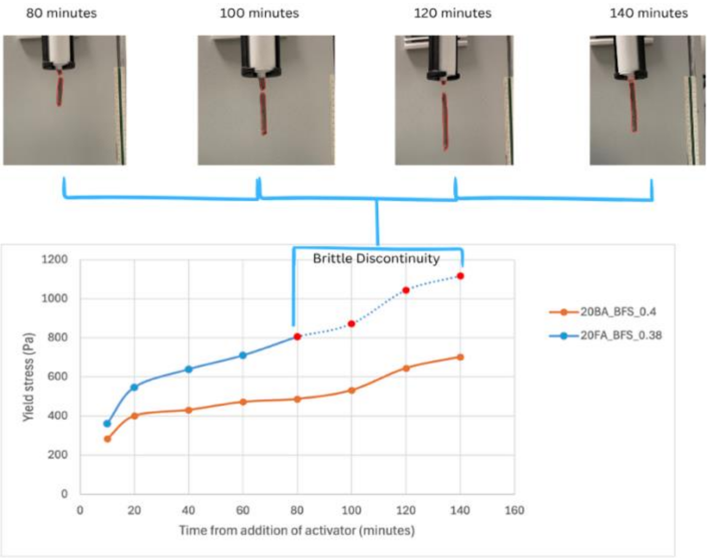

Figure 5.3 Brittle discontinuity in slugs test of 20FA-BFS_0.38 mix from 80 minutes.

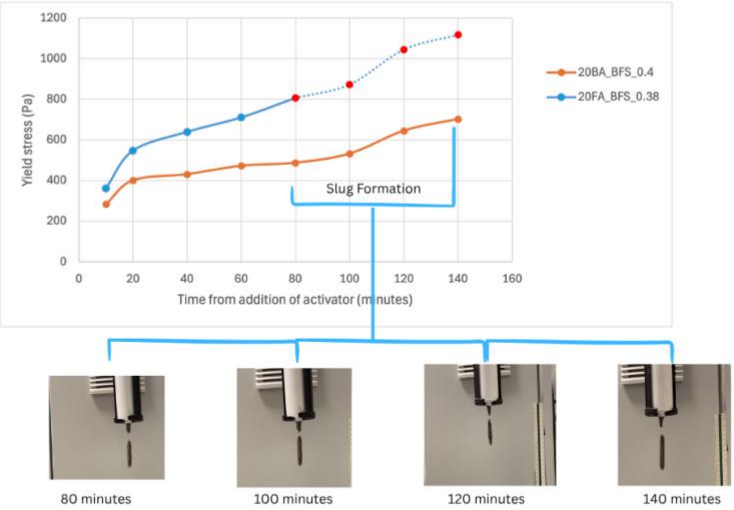

Figure 5.4 Slug formation in slugs test of 20BA-BFS_0.4 mix continuing beyond 80 minutes.

5.3 Pore Solution Analysis through ICP-OES

The evolution of concentration of elements in the pore solution provides critical insights into early-age reaction kinetics, influencing both the rheological behaviour and microstructural development of 3D printable mixtures. Monitoring specific elements such as Na, Si, Al, Ca, and Mg is essential, as these are directly involved in forming key reaction products, including calcium aluminosilicate hydrate (C-A-S-H), sodium aluminosilicate hydrate (N-A-S-H), and secondary phases like hydrotalcite. Their concentrations in the pore solution thus reflect precursor dissolution, reaction progress, and product formation.

The concentrations of Na, Si, Al, Ca, and Mg in the pore solution, are denoted as [Na], [Si], [Al], [Ca], and [Mg], respectively, and are presented in Figure *5.5* and Figure *5.6* as a function of time, up to 140 minutes for the 20FA-BFS_0.38 mix and 20BA-BFS_0.4 mix.

Throughout the considered timeframe, both mixtures exhibited a consistent ionic concentration order: [Na] > [Si] > [Al] > [Ca] > [Mg], with concentrations decreasing over time. This decrease indicates ongoing chemical reactions and progressive product formation. Concentration of Na and Si in the pore solution originate from the alkali activators and precursors. The higher concentrations of Na and Si result from the significant soluble Na and Si content provided by the activators. In contrast, Al, Ca, and Mg are primarily derived from the precursors, leading to comparatively lower concentrations. As the reaction advances, Si tetrahedrons in bridging positions are replaced by Al tetrahedrons and Na and Ca get incorporated into the chain with Al to neutralize the charge imbalance [45], [92]. The Na and Ca are consumed, and their concentration reduces gradually with time as the formation of C-A-S-H/N-A-S-H gels continues [83] Figure *5.5* and Figure *5.6*. However, a subtle increase in Na concentration observed in the BA-based mix after approximately 80 minutes indicates additional dissolution of amorphous Na_2O present in MSWI bottom ash. This amorphous Na_2O is present in significantly higher amounts compared to BFS and FA Table *3.2*.

A notable observation is that the consistently lower concentration levels of Na, Si, Ca, and Mg in the pore solution of the BA-based mix (20BA-BFS_0.4) compared to the FA-based mix (20FA-BFS_0.38). Additionally, elemental concentrations in the FA-based reference mix declined more rapidly than in the BA-based target mix, indicating faster reaction kinetics and quicker precipitation of reaction products in the FA system.

This difference in concentration trends of the elements can be attributed to the combined influence of the change in water content and the incorporation of MSWI bottom ash. The higher water content in the BA-based mix reduces alkalinity of pore solution, limiting the dissolution rates of aluminosilicate sources, thereby leading to lower concentrations. However, the difference in initial concentrations for Na, Si, Ca, and Mg is substantially greater than the dilution caused 5% addition of water. Additionally, in the initial stages, the dissolution is dominated by slag. Literature shows that MSWI bottom ash releases heavy metals such as chromium (Cr), zinc (Zn) and lead (Pb) into the pore solution [93], [94]. The high pH environment typical of alkali-activated systems promotes the mobilization of these metal ions from the bottom ash. These metal ions react with hydroxide ions present in the pore solution to form metal hydroxides, which precipitate on the surface of unreacted slag particles and hinder the slag reaction [93], [94]. Hence, the release of these elements from bottom ash impedes slag dissolution in the early stages of the BA-based mix. On the other hand, Al concentrations in both mixes remain relatively stable, fluctuating between 25–33 mmol/L over time. This stability can be attributed to equilibrium between dissolved Al and the early formation of Al-bearing gels, confirmed by thermodynamic modelling (GEMS), which indicates saturation of Al-bearing phases, preventing substantial increases in concentrations.

The concentration of Ca was observed to be in the low range, 3.4 – 0.9 mmol/L for 20FA-BFS_0.38 sample and 1.6 – 0.5 mmol/L for 20BA-BFS_0.4 sample and decreased with time. These values are consistent with previously reported low ranges for high-calcium-based alkali activated systems from the literature [83], [95]. This decline of [Ca] is associated with immediate incorporation of Ca into C-A-S-H gels. Interestingly, despite the BA-BFS system containing significantly more calcium than the FA-BFS system (with MSWI BA having a CaO content of 10.87%, nearly twice that of fly ash, plus the additional calcium from BFS), the Ca concentration in 20BA-BFS_0.4 (1.6 to 0.5 mmol/L) remains consistently lower than in 20FA-BFS_0.38 (3.4 to 0.9 mmol/L). This counterintuitive result further substantiates that BA hinders the release of Ca from BFS, effectively limiting calcium dissolution despite the higher total calcium content in the system.

Mg follows a similar trend as Ca but starts at even lower concentrations (~1.5 mmol/L initially, decreasing to <0.2 mmol/L over time) closer to the detection limit. The rapid decline in Mg indicates its incorporation into secondary phases such as hydrotalcite-like layered double hydroxides (LDH). Literature suggests that when the content of the MgO in slag exceeds 5%, hydrotalcite was identified as one of the main secondary products and as the MgO content increased hydrotalcite formation was found to be faster and higher [96], [97]. In our case the slag has about 9.4% of MgO in it as shown in Table *3.2*. This implied that the formation of hydrotalcite is highly likely. The subsequent thermodynamic modelling through GEMS further validates these findings, emphasizing the formation of reaction products (C-N-A-S-H, N-C-A-S-H, N-A-S-H, hydrotalcite) consistent with these observed trends.

These observed elemental concentration trends directly correlate with rheological behaviour. Initially, 20FA-BFS_0.38 mix exhibits significantly higher initial concentrations compared to 20BA-BFS_0.4, indicating more intensive precursor dissolution. This enhanced dissolution generates a higher concentration of anionic species, creating stronger electrostatic repulsion between particles [29]. While both systems initially maintain fluidity through electrostatic stabilization, the higher ionic concentrations in the FA-based system accelerate subsequent polymerization reactions. This results in increasingly rigid inter-particle connections and stronger van der Waals attraction. These mechanisms lead to the rapid formation of a percolated elastic network, causing an earlier transition from a repulsion-dominated to an attraction-dominated rheological regime. As a result, the FA-based mix develops sufficient yield stress to exhibit brittle fracture around 80 minutes.

In contrast, the 20BA-BFS_0.4 exhibits a more gradual decrease in ionic concentrations. This suggests slower dissolution-polymerization kinetics, whereby electrostatic repulsion remains dominant for an extended period, delaying the development of a fully rigid particle network. Consequently, this allows the BA-based mixture to remain plastic and facilitate continuous slug formation. This explains why 20FA-BFS_0.38 develops sufficient yield stress to exhibit brittle fracture by 80 minutes, while 20BA-BFS_0.4 retains adequate plasticity for slug formation throughout the 140-minute test period.

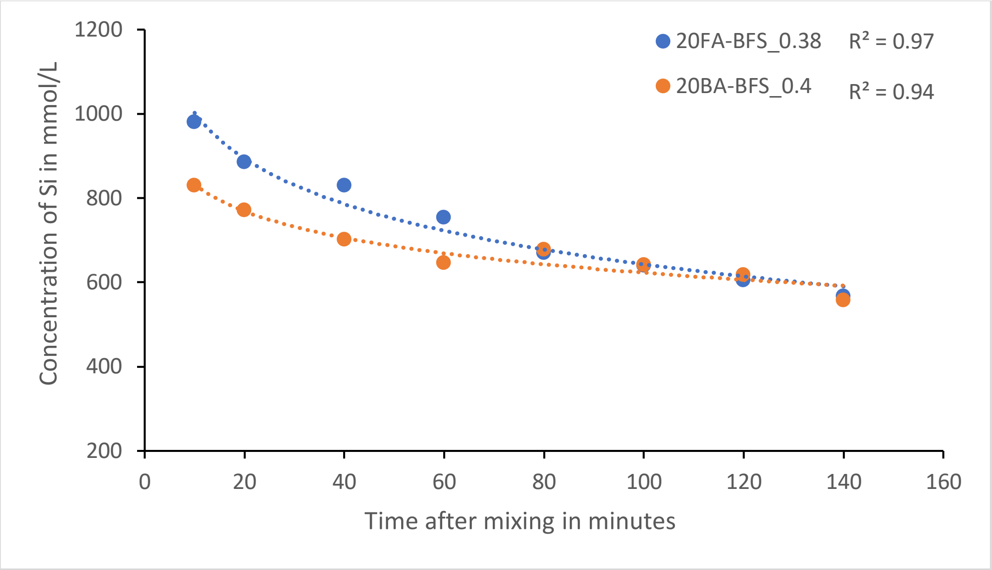

(a)

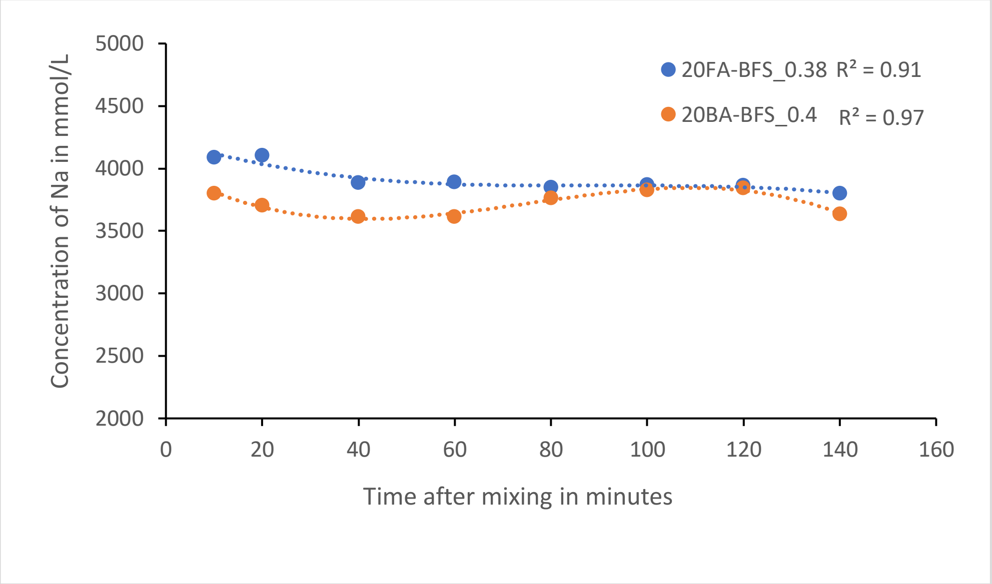

(b)

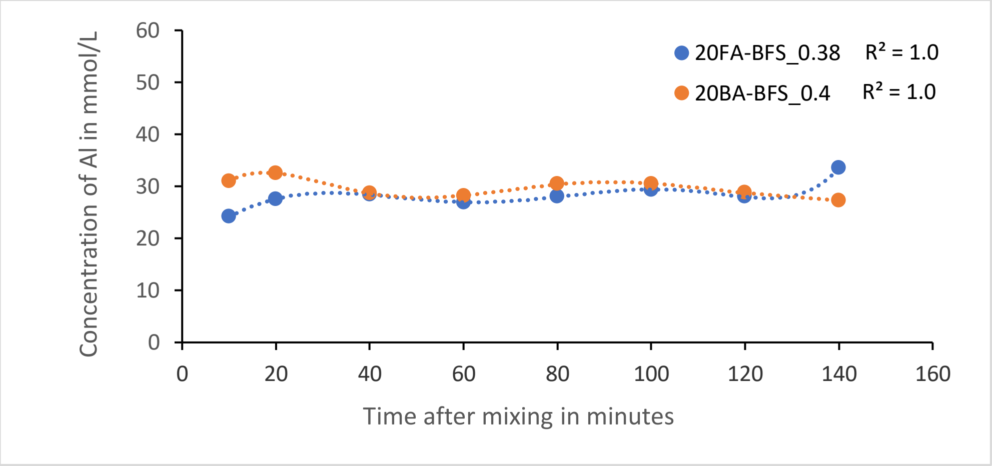

(c)

Figure 5.5 Concentration of (a) silica([Si]), (b) sodium ([Na]), and (c) aluminium ([Al]) in pore solution.

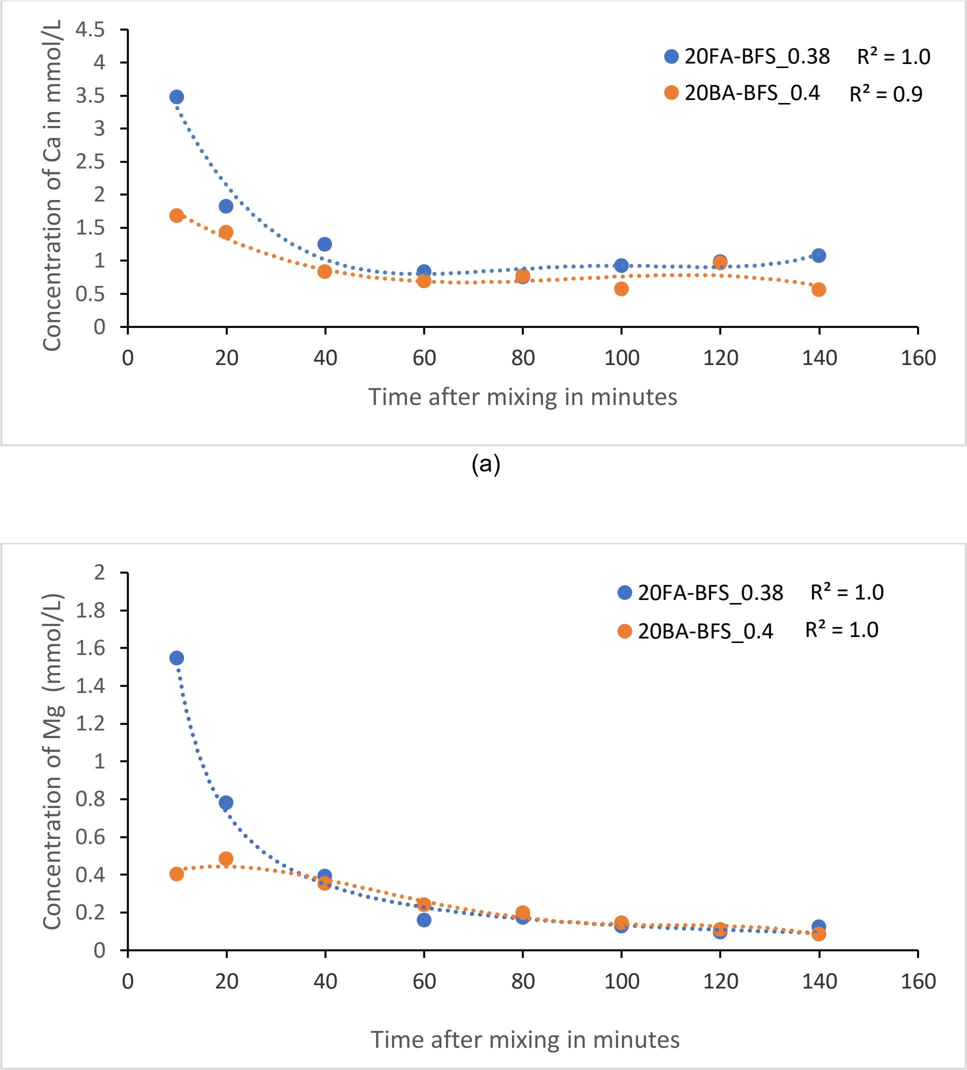

(a)

(b)

Figure 5.6 Concentration of (a) calcium([Ca]) and (b) magnesium ([Mg]) in pore solution.

5.4 Thermodynamic modelling of Pore Solution through GEMS

Thermodynamic modelling using Gibbs Energy Minimization Software (GEM-Selektor, version 2023) was conducted to validate the trends observed in the pore solution analysis of previous section. The primary reaction products dominant in alkali activated systems are the calcium aluminosilicate hydrates (C-(N-)A-S-H) and sodium calcium aluminosilicate hydrate gels (N-C-A-S-H), and hydrotalcite-like layered double hydroxides (LDHs). Hydrotalcite was considered an important secondary product due to the significant MgO content in slag. To model these three specific models sourced from established databases [75]and the N-C-A-S-H thermodynamic database [76], [77]were utilized in this analysis: CNASH_ss model, MA-OH-LDH_ss model and N-C-A-S-H model.

The CNASH_ss model was used for calcium aluminosilicate hydrates, comprising end members 5CA and INFCA representing the C-A-S-H gel, 5CNA and INFCNA representing the C-N-A-S-H gel, INFCN representing the C-N-S-H gel, and T2C, T5C, and TobH representing the C-S-H gel [83]. The MA-OH-LDH_ss model included hydrotalcite-like phases with different Mg/Al ratios represented by end members M4A-OH-LDH, M6A-OH-LDH, and M8A-OH-

LDH[83]. Additionally, the N-C-A-S-H model represented sodium aluminosilicate gels, consisting of three NASH end members (Nash1, Nash2, Nash3) and four calcium-incorporated sodium aluminosilicate end members (NCASH1, NCASH2, NCASH3, NCASH4) [77]. The equilibrium solubility products (log Kso) of these end-members, essential for calculating the Effective Saturation Index (ESI), are summarized in Table *5.1* along with their respective dissolution equations.

Table 5.1 Chemical reactions and equilibrium solubility products at 25°C and 1 bar for C-(N-)A-S-H, hydrotalcite-like phases and N-(C-)A-S-H gels [77], [83], [98].

Phase	Chemical Reactions	log K_{so}
C-(N-)A-S-H Gel Phases (CNASH_ss model)		
5CA	$(CaO)_{1.25}(Al_20_3)_{0.125}(SiO_2).(H_2O)_{1.625} \rightleftharpoons 1.25Ca^{2+}+SiO_3^{2-}+0.25AlO_2^{-}+0.25OH^{-}+1.5H_2O$	-10.75
INFCA	$(CaO).(AL_2O_3)_{0.15625}.(SiO_2)_{1.1875}.(H_2O)_{1.65625}+0.6875OH \rightleftharpoons Ca^{2+}+1.1875SiO_3^{2-}+0.3125AlO_2^{-}+2H_2O$	-8.90
5CNA	$(CaO)_{1.25}.(Na_2O)_{0.25}.(Al_20_3)_{0.125}.(SiO_2).(H_2O)_{1.25} \rightleftharpoons 1.25Ca^{2+}+SiO_3^{2-}+0.25AlO_2^{-}+0.5Na^{+}+0.75OH^{-}+H_2O$	-10.40
INFCNA	$(CaO).(Na_2)_{0.34375}.(AL_2O_3)_{0.15625}.(SiO_2)_{1.1875}.(H_2O)_{1.3} \rightleftharpoons Ca^{2+}+1.1875SiO_3^{2-}+0.3125AlO_2^{-}+0.6875Na^{+}+1.3125H_2O$	-10.00
INFCN	$(Ca0).(Na_2O)_{0.3125}.(SiO_2)_{1.5}.(H_2O)_{1.1875}+0.375OH \rightleftharpoons Ca^{2+}+1.5SiO_3^{2-}+0.625Na^{+}+1.375H_2O$	-10.70
T2C-CNASHss	$(CaO)_{1.5}.(SiO_2).(H_2O)_{2.5} \rightleftharpoons 1.5Ca^{2+}+SiO_3^{2-}+OH^{-}+2H_2O$	-11.60
T5C-CNASHss	$(CaO)_{1.25}.(SiO_2)_{1.25}.(H_2O)_2 \rightleftharpoons 1.25Ca^{2+}+1.25SiO_3^{2-}+2.5H_2O$	-10.50
TobH-CNASHss	$(CaO).(SiO_2)_{1.5}.(H_2O)_{2.5}+OH^{-} - \rightleftharpoons Ca^{2+}+1.5SiO_3^{2-}+3H_2O$	-7.90
Hydrotalcite-like Phases (MA-OH-LDH_ss model)		
M4A-OH-LDH	$(MgO)_4.(Al_2O_3).(H_2O)_{10} \rightleftharpoons 4Mg^{2+}+2AlO^{-}_{2}+6OH^{-}+7H_2O$	-49.70
M6A-OH-LDH	$(MgO)_6.(Al_2O_3).(H_2O)_1 \rightleftharpoons 6Mg^{2+}+2AlO^{-}_{2}+10OH^{-}+7H_2O$	-72.02
M8A-OH-LDH	$(MgO)_8.(Al_2O_3).(H_2O)_{14} \rightleftharpoons 8Mg^{2+}+2AlO^{-}_{2}+14OH^{-}+7H_2O$	-94.34
N-C-A-S-H gels		
nash1	$(Na_2O)_{0.46}(Al_2O_3)_{0.46}(SiO_2)_1(H_2O)_{0.54} \rightarrow 0.92\ Na^{+}+0.92\ AlO_2^{-}+SiO_2^{0}+0.54\ H_2O$	-8.47
Nash2	$(Na_2O)_{0.25}(Al_2O_3)_{0.25}(SiO_2)_1(H_2O)_{0.35} \rightarrow 0.5\ Na^{+}+0.5\ AlO_2^{-}+SiO_2^{0}+0.35\ H_2O$	-6.44
Nash3	$(Na_2O)_{0.18}(Al_2O_3)_{0.18}(SiO_2)_1(H_2O)_{0.31} \rightarrow 0.36\ Na^{+}+0.36\ AlO_2^{-}+SiO_2^{0}+0.31\ H_2O$	-5.38
NCASH1	$(Na_2O)_{0.25}(CaO)_{0.11}(Al_2O_3)_{0.25}(SiO_2)_1(H_2O)_{0.47} \rightarrow 0.11Ca^{2+}+0.5Na^{+}+0.5AlO_2^{-}+SiO_2^{0}+0.22OH^{-}+0.36H_2O$	-7.70
NCASH2	$(Na_2O)_{0.23}(CaO)_{0.2}(Al_2O_3)_{0.23}(SiO_2)_1(H_2O)_{0.42} \rightarrow 0.2Ca^{2+}+0.46Na^{+}+0.46AlO_2^{-}+SiO_2^{0}+0.4OH^{-}+0.22H_2O$	-8.50
NCASH3	$(Na_2O)_{0.23}(CaO)_{0.08}(Al_2O_3)_{0.16}(SiO_2)_1(H_2O)_{0.44} \rightarrow 0.08Ca^{2+}+0.46Na^{+}+0.32AlO_2^{-}+SiO_2^{0}+0.3OH^{-}+0.29H_2O$	-6.75
NCASH4	$(Na_2O)_{0.24}(CaO)_{0.15}(Al_2O_3)_{0.18}(SiO_2)_1(H_2O)_{0.42} \rightarrow 0.15Ca^{2+}+0.48Na^{+}+0.36AlO_2^{-}+SiO_2^{0}+0.42OH^{-}+0.21H_2O$	-7.52

The ESI results with respect to time for CNASH_ss model, MA-OH-LDH_ss model and N-C-A-S-H model are shown in Figure *5.7* for 20FA-BFS_0.38 and 20BA-BFS_0.4 mixes respectively.

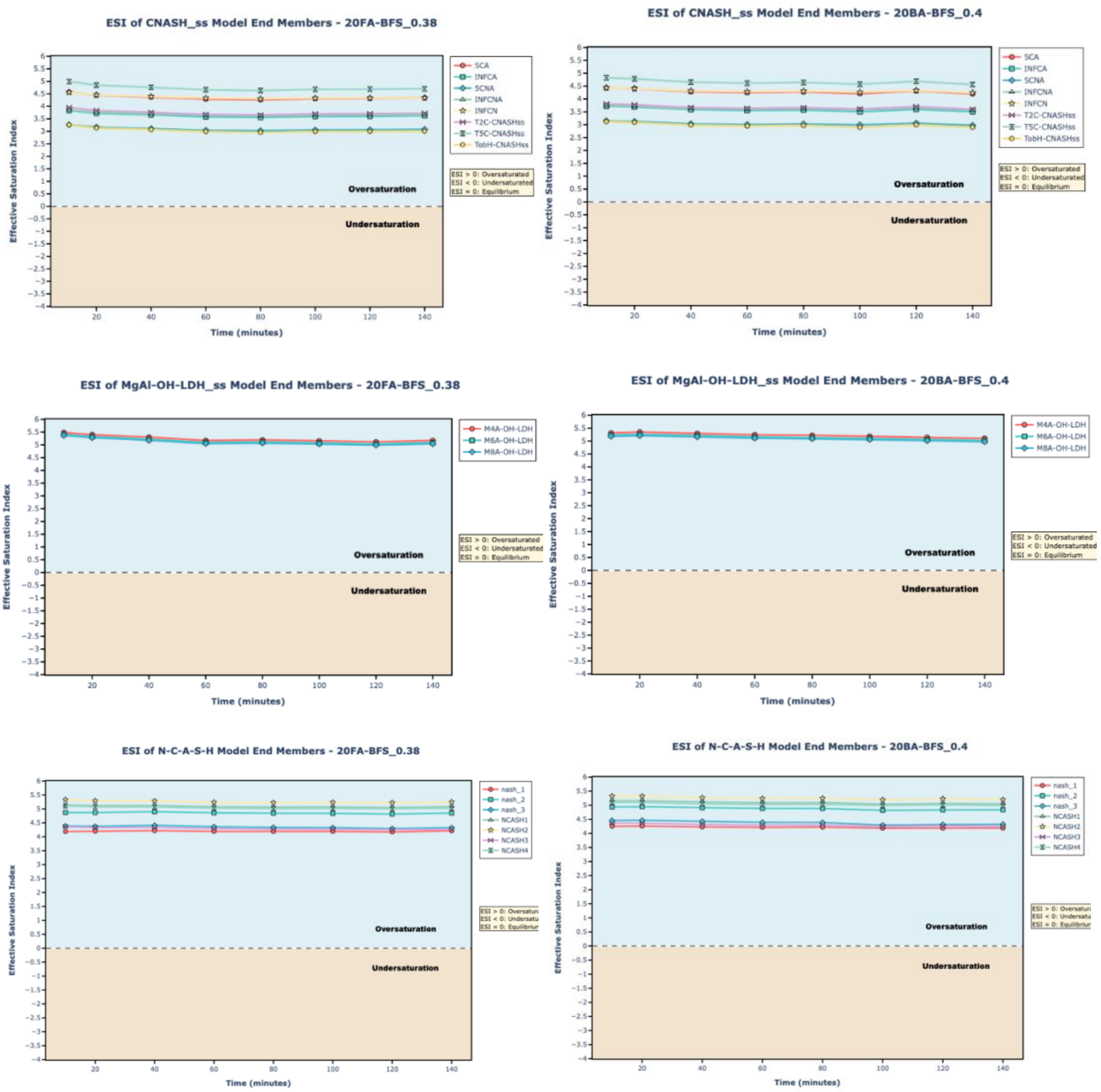
ESI of CNASH_ss Model End Members - 20FA-BFS_0.38

ESI of CNASH_ss Model End Members - 20BA-BFS_0.4

ESI of MgAl-OH-LDH_ss Model End Members - 20FA-BFS_0.38

ESI of MgAl-OH-LDH_ss Model End Members - 20BA-BFS_0.4

ESI of N-C-A-S-H Model End Members - 20FA-BFS_0.38

ESI of N-C-A-S-H Model End Members - 20BA-BFS_0.4

Figure 5.7The ESI results of 20FA-BFS_0.38 and 20BA-BFS_0.4 mix with respect to time for CNASH_ss model, MA-OH-LDH_ss model and N-C-A-S-H model.

All ESI values for the analyzed phases were consistently positive (ESI > 0) for both mixes throughout the test period, indicating continuous oversaturation. This oversaturation signifies that the pore solutions have sufficient thermodynamic driving force for precipitation, thus confirming the potential for these phases to precipitate during early hydration stages. In thermodynamic terms:

- ESI > 0 indicates oversaturation and the possibility of phase precipitation.
- ESI = 0 indicates equilibrium.
- ESI < 0 indicates undersaturation and potential dissolution.

The ESI trends align strongly with the observed ICP-OES concentration trends. The gradual decrease in concentrations of Si, Ca, Na, and Mg reflects the ongoing formation and precipitation of reaction products such as C-(N-)A-S-H gels, N-(C-)A-S-H gels and hydrotalcite. The oversaturation of hydrotalcite end members supports the rapid decline in Mg concentration, validating its expected early precipitation given the significant MgO content in slag.

This thermodynamic analysis effectively validates the experimental ICP-OES results, highlighting the early precipitation potential of critical phases. This integrated approach significantly enhances the understanding and prediction of early-age reaction kinetics in alkali-activated printable mixes.

5.5 Solid Phase Analysis Through ATR-FTIR

Fourier Transform Infrared spectroscopy (FTIR) was employed to monitor the structural evolution and gel formation within the solid phases, complementing the liquid-phase analysis discussed in the previous section. This technique enables identification of functional groups through characteristic wavenumber patterns, providing insights into the formation of reaction products and gel structure development [79], [80].

Figure *5.8* presents the FTIR spectra of Dry samples 20FA-BFS and 20BA-BFS, while Figure *5.9* and Figure *5.10* illustrate the time-dependent spectral evolution of the 20FA-BFS_0.38 and 20BA-BFS_0.4 respectively during the first 140 minutes of reaction with main bands marked [99].

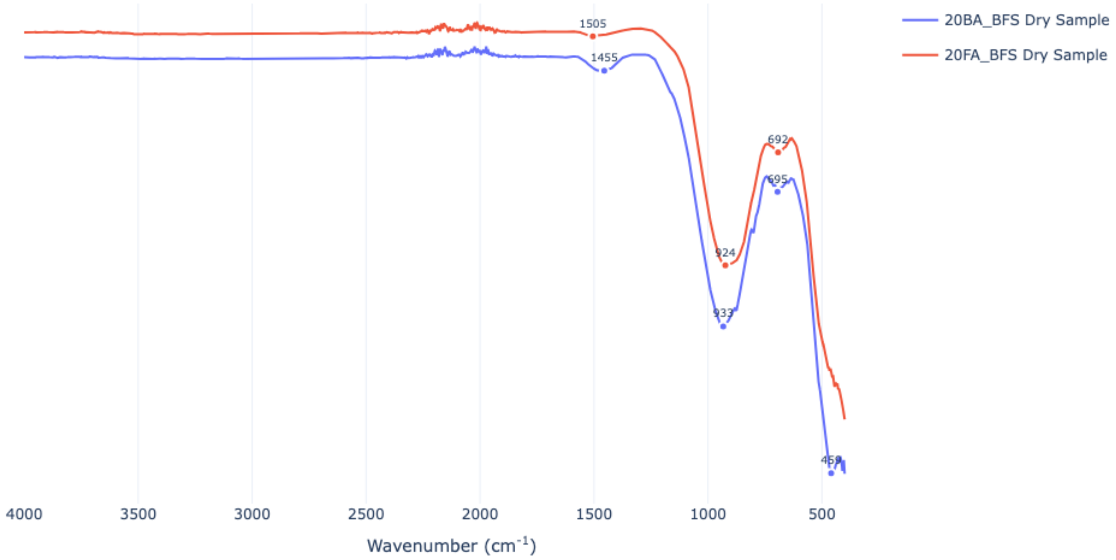

Figure 5.8 FTIR spectra of 20FA-BFS and 20BA-BFS dry samples.

In Figure *5.9* and Figure *5.10*, the broad band observed between 3600–2370 cm-1 [79] corresponds to O–H stretching vibration of hydroxyl molecule in water [100], [101], [102]. This bands primarily indicates water embedded in reaction products such as C–S–H and C–A–S–H, representing structural and absorbed water [79], [99], [101], [103], and can also represent free water present within the material [104]. However, the intensity of these signals is very low, as the majority of water present during the early stages is free/absorbed water, which is most likely to evaporate during the freeze-drying process. In addition to the water-related bands, carbonate group bands are generally present at approximately 1400-1550 cm^{-1} [99] and 880 cm^{-1} in the FTIR spectra correspond to the asymmetric stretching vibration and out-of-plane bending vibration of C–O bonds in carbonates, respectively [100], [102], [104], [105], [106], indicating the carbonation of amorphous gels or other sodium compounds [100], [102]. These two bands in both the activated samples imply the formation of reaction products (C-(A)-S-H/N-A-S-H or hydrotalcite), and a portion of these products had undergone carbonation

[80] possibly due to exposure to atmospheric CO_2 during sample preparation or storage[80], [101].

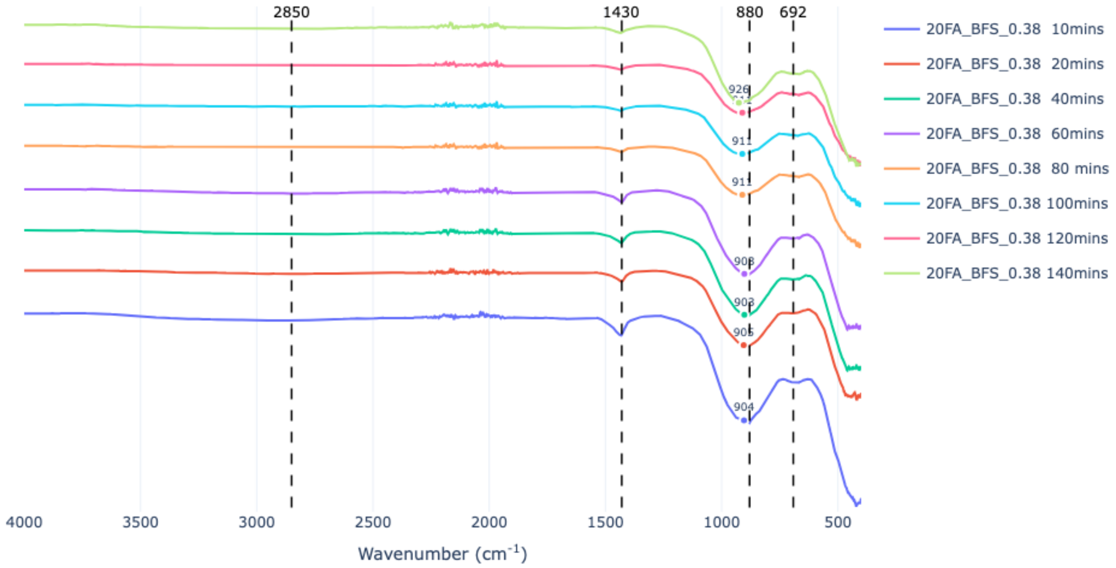

Figure 5.9 FTIR spectra of 20FA-BFS_0.38 mix with evolution of time.

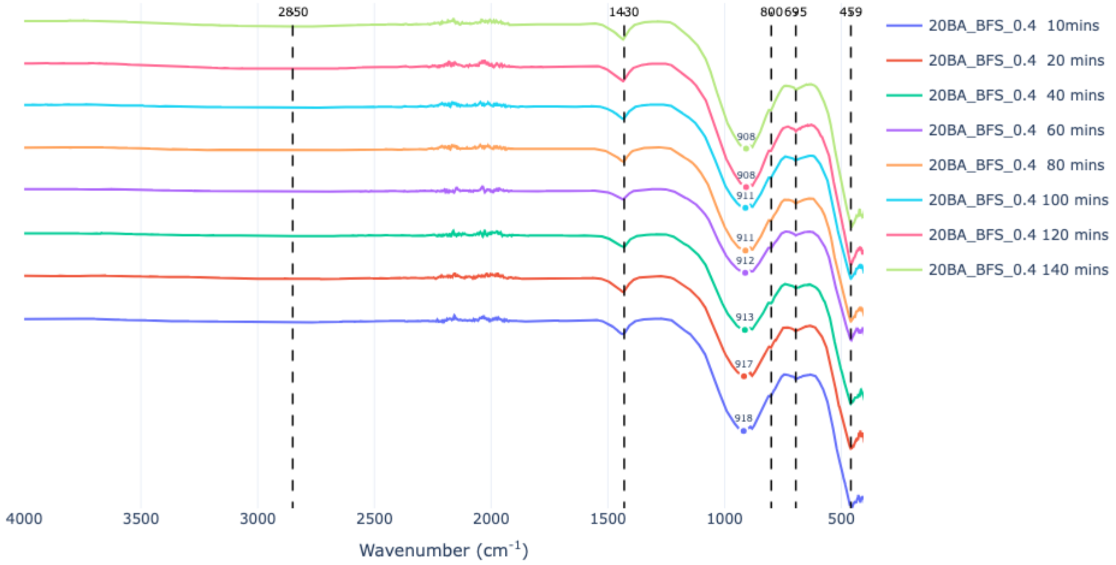

Figure 5.10 FTIR spectra of 20BA-BFS_0.4 mix with evolution of time.

In Figure *5.8*, Figure *5.9* and Figure *5.10*, the band present around 692-695 cm^{-1} corresponds to Si–O symmetric stretching vibrations and is indicative of the presence of quartz. The band near 454 cm^{-1} is attributed to the bending vibrations of Si–O–Si and O–Si–O bonds. These bands are characteristic of unreacted silicates and are often associated with quartz [99], [101], [107], [108], [109]. Therefore, these spectral bands remain as such even after activation as they correspond to the quartz present in the starting material [102], which remains unreacted due to its crystalline nature. In this study, the slag used is completely amorphous, as confirmed in Table *3.2*, and thus does not contribute to these crystalline bands. The observed quartz-related bands, therefore, originate from the crystalline components present in the fly ash and bottom ash used in the respective mixes.

The FTIR spectrum of the two mixes exhibit a broad absorption band within the 800–1200cm^{-1} [105] range, corresponding to the asymmetric stretching vibrations of Si–O–T bonds (T: tetrahedral Si or Al) [80], [101], [108], arising from the combined vibrational modes of silicate and aluminate species in the aluminosilicate structure [105]. This band provides critical insights into the degree of polymerisation of the aluminosilicate network, and it highly depends on the presence of network formers (Si/Al ratio) and modifiers, as well as the alkali solution concentration. In alkali-activated systems, Al and Si function as network formers, while Na, Ca and Mg act as network modifiers. These network modifiers not only balance the charge of tetrahedral Al but also influence the depolymerization of the Si–O–T framework [45]. The increase in concentration of these network modifiers changes the structural disruption resulting in the formation of non-bridging oxygens (NBOs), directly impacting the material's polymerisation degree.

The extent of polymerisation can be assessed through the Si–O stretching vibrations of SiQ^n units (n = 0, 1, 2, 3, 4), where n refers to the number of bridging oxygen atoms connected to silicon, represents the degree of polymerization. In other words, n represents connectivity level[100]. Bands are typically centred around 850 cm^{-1} (SiQ^0), 900 cm^{-1} (SiQ^1), 950 cm^{-1} (SiQ^2), 1100(SiQ^3) and 1200 cm^{-1} (SiQ^4). Lower wavenumbers (e.g., 850–950 cm^{-1}) indicate lower polymerisation, whereas higher wavenumbers (e.g., 1100–1200 cm^{-1}) correspond to more polymerised and cross-linked structures [100], [107]. Therefore, the changes in the position of these Si–O stretching vibrations within FTIR spectra reflect the dissolution of precursors and the formation and reorganisation of the aluminosilicate gel network [81], [100]. The Figure *5.11* shows the connection modes of silicon-oxygen tetrahedra.

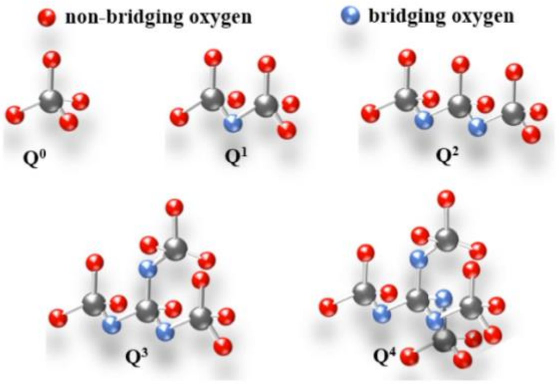

Figure 5.11 Connection modes of silicon-oxygen tetrahedra [110].

The dry samples of 20FA-BFS and 20BA-BFS had their main peak of the Si–O–T absorption band centred at 921 cm^{-1} and at 932 cm^{-1} respectively as shown in Figure *5.8*, highlighting the differences in precursor chemical compositions and glass structures of these materials [99]. The overall position of these peaks is relatively in the lower wavenumber range (900–950 cm^{-1}), indicating the dominance of low-polymerised silica and alumina species, specifically Q2 and Q3 units. The presence of such low-polymerised units (Q^1 and Q^0) is typically minimal in fly ash [107] and bottom ash. However, the observed lower crosslinking in these raw materials is primarily attributed to the system's high calcium content [99], stemming from the significant proportion of slag (~80%) in the precursor blend. The lower wavenumber peaks observed in the FTIR spectra of raw precursor samples is thus reflected from calcium acting as a network depolymerisation cation [107].

After activation, as only the vitreous components of the precursors dissolve. Initially, this dissolution causes the Si–O–T absorption bands of 20FA-BFS_0.38 and 20BA-BFS_0.4 mixtures progressively shifted towards lower wavenumbers as shown in Figure *5.12*. This shift indicates the formation of negatively charged silica and alumina monomers and/or monomers[91]. At this early stage, these negatively charged silicate oligomers adsorbed onto the particle surfaces, significantly enhancing the electrostatic inter-particle repulsive forces between particles [29]. Such repulsion promotes effective dispersion and sustained fluidity in the initial stages.

The 20FA-BFS_0.38 mixture shows rapid shift towards lower wavenumbers compared to the 20BA-BFS_0.4 mix after activation. The extent of this shift is governed by changes in the Si/Al ratio within the forming gel, where an increase in Al content results in a shift to lower wavenumbers due to the lower valency force constant of Al–O bonds compared to Si–O [105]. This shift reflects the substitution of $(SiO_4)^{4-}$ by $(AlO_4)^{4-}$, where Al^{3+} replaces Si^{4+} in the Si–O–Si framework, resulting in the formation of an aluminium–oxygen tetrahedral structure [104]. The inclusion of Al^{3+} into these early gels subsequently required further alkali cations (Na^+, Ca^{2+}) to maintain charge neutrality, leading to the rapid depletion of [Ca] and [Na] from the pore solution. The consistent Al concentration observed in ICP analysis can also be explained in this context. The rapid incorporation of dissolved Al into aluminosilicate gels observed here aligns well with earlier thermodynamic modelling (GEMS) results.

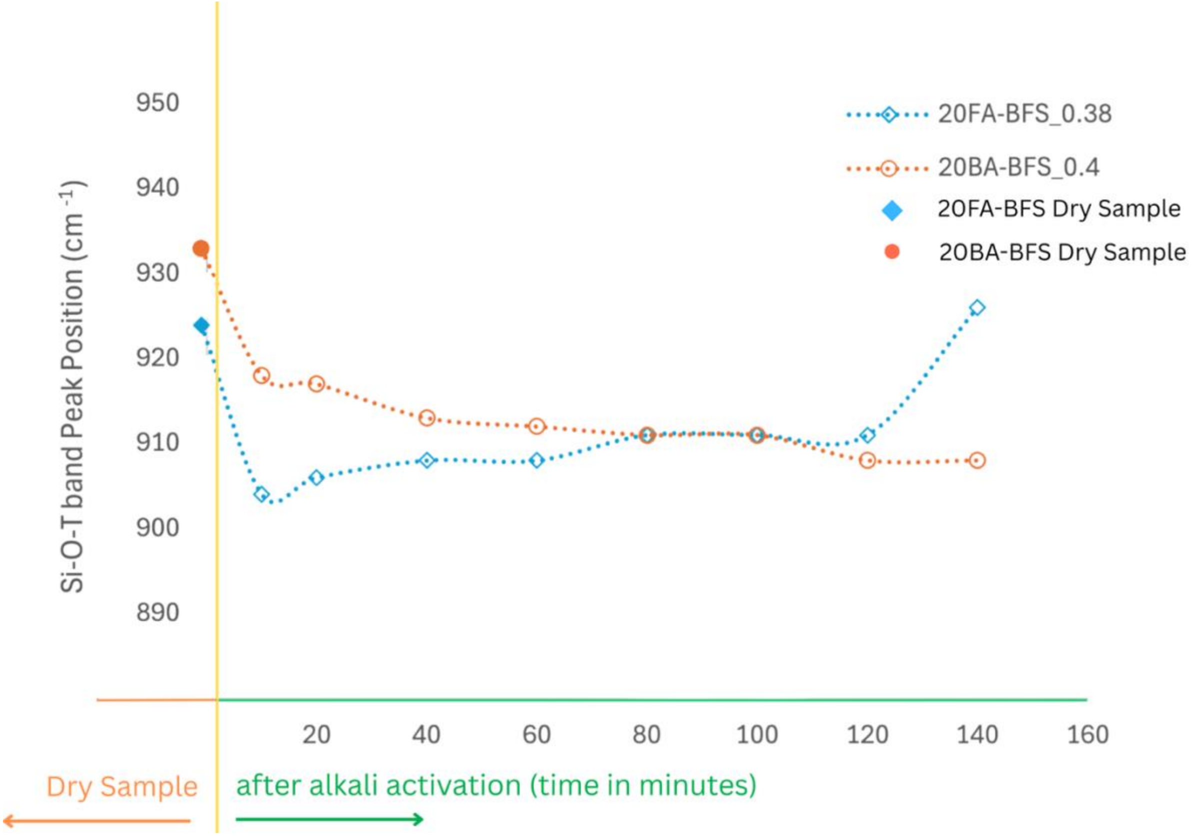

Figure 5.12 Evolution of Si-O-T band starting from dry samples of 20FA-BFS and 20BA-BFS to 20FA-BFS_0.38 and 20BA-BFS_0.4 after activation.

In the later stages of the process, a re-shift of Si-O-T band towards higher waver numbers is observed in the 20FA-BFS_0.38 mix. This demonstrates that the initially formed oligomers and monomers interconnect and gradually polymerise and cross-linking within the gel network forming larger aluminosilicate structural units [91].This faster shift indicates accelerated initial reaction kinetics. On the contrary, 20BA-BFS_0.4 mix maintains a more gradual shift towards lower wavenumbers (from 918 cm^{-1} to 908 cm^{-1}), consistently indicating persistent lower polymerization and higher concentrations of smaller, negatively charged silicate oligomers. The dominance of these smaller oligomers sustains electrostatic repulsive forces, prolonging the dispersion of precursor particles, delaying the polymerization[91], and subsequently extending the printable window. This trend is also indicative of slower reaction kinetics of 20BA-BFS_0.4 mix compared to 20FA-BFS_0.38 mix.

While hydrotalcite formation is expected in slag-rich systems, it is typically not traceable during early stages due to its low initial quantities and the dominance of primary reaction products such as CNASH, NASH, and NCASH. The FTIR spectra show no characteristic hydrotalcite bands. This suggests its presence is likely in trace amounts, below the detection threshold at this early stage. Additionally, its signals may overlap with those of primary reaction products.

These findings align with prior studies where hydrotalcite becomes distinctly observable only after 2-3 days of curing. This is particularly true in systems with higher Mg and Al availability[96], [97], [111]. Thermodynamic modelling performed via GEMS confirms that hydrotalcite may be present even when experimentally undetectable. The difficulty in detection arises from its coexistence with dominant early-stage gels.

The differences in polymerization dynamics of Si-O-T band clearly explain the distinct rheological behaviours of the two mixtures. The 20BA-BFS_0.4 system exhibits slower reaction kinetics due to the presence of bottom ash and higher water content compared to 20FA-BFS_0.38. This slower kinetics maintains persistent low-polymerized negatively charged silicate oligomers (SiQ^1). These oligomers adsorb onto particle surfaces, significantly enhancing electrostatic inter-particle repulsive forces. The sustained electrostatic repulsion delays the development of a percolated network [29], which in turn beneficially extends the printable window for practical applications.

In contrast, the FA-based mixture undergoes rapid polymerization of aluminosilicate monomers and oligomers. The faster transition to more polymerized species (SiQ^3) reduces electrostatic repulsion between particles. This reduction enhances particle attraction and van der Waals forces. Consequently, interparticle bridging develops more rapidly [29], shortening the printable window but accelerating yield stress development.

5.6 Conclusions

In this chapter, the early-age reaction kinetics of two 3D printable alkali-activated mixes were investigated to understand how the substitution of fly ash with MSWI bottom ash influences rheological performance and the printability window. A systematic approach was employed combining yield stress evolution, pore solution chemistry, thermodynamic modelling, and solid phase analysis to establish correlations between reaction kinetics and rheological behaviour. The key findings are presented below:

- The yield stress evolution revealed that the BA-based mix (20BA-BFS_0.4) maintained continuous slug formation throughout the 140-minute test period, while the FA-based mix (20FA-BFS_0.38) exhibited brittle discontinuity after 80 minutes. This extended printable window in the BA-based system demonstrates its superior processability for 3D printing applications requiring longer pumping or staging intervals.

- Pore solution analysis showed consistently lower elemental concentrations ([Na], [Si], [Ca], [Mg]) in the BA-based mix compared to the FA-based mix. The slower decline and lower concentrations in 20BA-BFS_0.4 indicated reduced precursor dissolution rates, attributed to both higher water content and the release of some heavy metals from MSWI bottom ash under high pH conditions that precipitate as hydroxides on slag particle surfaces, hindering slag dissolution.

- The correlation between pore solution chemistry and rheology was established through the role of electrostatic forces. Higher initial elemental concentrations in 20FA-BFS_0.38 accelerated the transition from a repulsion-dominated to an attraction-dominated regime, leading to rapid percolated network formation and early brittle failure.

- Thermodynamic modelling confirmed continuous oversaturation (ESI > 0) for C-(N-)A-S-H gels, N-(C-)A-S-H gels, and hydrotalcite phases in both systems. The validation of experimental ICP-OES results through GEMS modelling strengthened the understanding of phase precipitation potential during early hydration.

- FTIR analysis revealed distinct polymerization dynamics between the two systems. The Si-O-T band in 20BA-BFS_0.4 maintained a position at lower wavenumbers (908-918 cm^{-1}) throughout the test period, indicating persistent dominance of low-polymerized silicate oligomers (SiQ^1). In contrast, 20FA-BFS_0.38 showed rapid initial shift followed by polymerization towards higher wavenumbers, confirming accelerated gel network formation.

- This analysis established that MSWI bottom ash incorporation fundamentally altered the reaction kinetics by maintaining electrostatic repulsion dominance for an extended period. This was evidenced by: (i) sustained presence of negatively charged silicate oligomers detected through FTIR, (ii) slower and lower consumption rates of the key elements measured by ICP-OES, and (iii) delayed yield stress development observed in the slugs test.

- The slower reaction kinetics in the BA-based system, while reducing early-age strength development potential, beneficially extended the printable window by delaying the formation of rigid interparticle connections. This trade-off between reaction rate and workability time presents opportunities for optimizing 3D printing processes through controlled incorporation of MSWI bottom ash.

6

Life Cycle Assessment of Developed Mixtures

6.1 Introduction

The construction sector is under increasing pressure to adopt sustainable materials that can reduce environmental impacts without compromising performance. Alkali-activated materials (AAMs) have emerged as a viable alternative to conventional cement-based binders [31]. In this chapter, the environmental effects of slag-based alkali-activated mortar (AAM) mixes are quantified and compared with those of a reference OPC-based mix from literature. The focus is to evaluate whether MSWI BA can act as an effective substitute for FA while maintaining comparable performance and contributing to sustainable material use.

To assess the environmental impact of these mortar systems, a Life Cycle Assessment (LCA) was carried out following the ISO 14000 series framework. LCA is a globally recognized method for evaluating the potential environmental impacts of a product throughout its life cycle, from raw material extraction to production, use, and end-of-life disposal. Originally introduced in the late 1960s and formalized by SETAC in 1990, LCA is now a key tool in sustainability-focused decision-making across various industries. Life Cycle Assessment (LCA) is an analytical method used to calculate the Environmental Cost Indicator (ECI). In this study, the ECI methodology is applied to benchmark the developed AAM mixes against the cement-based reference mix.

This study evaluates three alkali-activated mortar mixes developed in this research: two FA-based mixes (20FA-BFS_0.38 and 20FA-BFS_0.4) and one MSWI BA-based mix (20BA-BFS_0.4). The 20FA-BFS_0.38 and 20BA-BFS_0.4 are optimized for 3D printing applications, while 20FA-BFS_0.4 serves as a control mix for comparison with Ba-based mix with same water content. These are compared against a 3D printable OPC-based mortar from literature [112] containing ordinary Portland cement, silica fume, fly ash, and sand.

In the Netherlands, environmental performance is typically expressed using the Environmental Cost Indicator (ECI), which aggregates impacts into a single score using the SBK method and it provides quantitative, multi-category environmental data. This approach accounts for 11 key environmental categories, including global warming, resource depletion, acidification, eutrophication, and toxicity effects on humans and ecosystems.

6.2 Methodology

The methodology adopted in this study follows the ISO 14040 framework for Life Cycle Assessment [84], ensuring a standardised and transparent evaluation process. It includes four key phases: goal and scope definition, life cycle inventory analysis, impact assessment, and interpretation as shown in Figure *6.1*. By adhering to this internationally recognised structure, the study provides a consistent basis for comparing the environmental performance of different mortar systems.

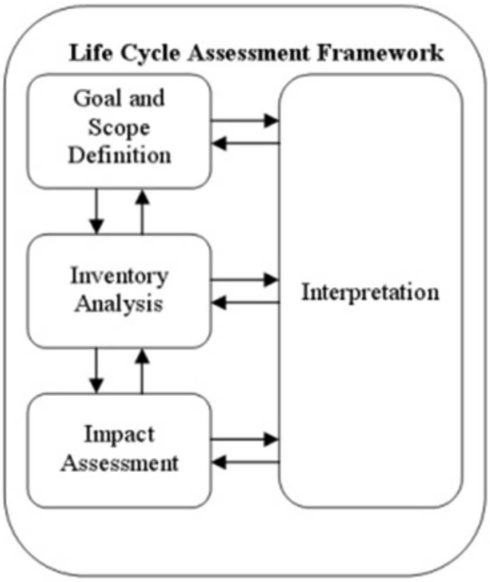

Figure 6.1 Schematic diagram of life cycle assessment procedure [84].

6.3 Goal and Scope of LCA

The goals of the LCA analysis are the following:

1. To evaluate the environmental performance of MSWI BA-based 3D printable alkali-activated mortar against fly ash-based mortar mixes and conventional Portland cement mortar.

2. To determine the relative environmental contributions of each constituent material and identify critical impact categories associated with AAM production.

3. To establish the environmental feasibility of utilizing MSWI BA as a sustainable fly ash alternative through comparative shadow cost analysis of all developed mortar systems.

Functional Unit: The functional unit is set as 1 cubic metre (1 m^3) of fresh mortar, which allows for a fair and standardized comparison across all mixes regardless of material type. All calculations, impact assessments, and comparisons are normalized to this unit. Geographically, the study is based in the Netherlands and thus follows the national Environmental Cost Indicator (ECI) methodology developed under the SBK framework. All impact results are expressed in monetary terms (€/m^3) using this single-score approach, which aggregates multiple environmental categories into a single quantifiable metric.

Scope: The Life Cycle Assessment (LCA) in this chapter is structured according to system boundaries, following the framework outlined in NEN 15804. This framework divides a product's life cycle into four main phases: production, construction, use, and end-of-life. Within the production phase, the analysis includes raw material extraction (A1), transportation (A2), and processing or manufacturing (A3). However, as the focus of this study is to evaluate and compare different concrete mixtures based on their constituent materials, only the raw material extraction phase (A1) is considered. Furthermore, since the mixes assessed are sourced from existing literature, specific data on transportation and manufacturing stages are unavailable and thus excluded from the assessment. Additionally, Data for silica fume is not available for the following impact categories and therefore these were excluded from the analysis: Human

Toxicity Potential, Freshwater Aquatic Ecotoxicity Potential, Marine Aquatic Ecotoxicity Potential, and Terrestrial Ecotoxicity Potential.

6.4 Inventory Analysis

The life cycle inventory included all constituent materials of the mortar mixes: blast furnace slag (BFS), fly ash (FA), municipal solid waste incineration bottom ash (MSWI BA), ordinary Portland cement (OPC), silica fume, sodium hydroxide (NaOH), sodium silicate (water glass) and sand. Environmental impact data of raw materials was sourced from verified Environmental Product Declarations (EPDs) and NIBE Database [113]. The Environmental data for blast furnace slag was obtained from verified MRPI-EPD provided by Ecocem Benelux B.V. [114], representing cradle-to-gate impacts of slag produced in the Netherlands. Environmental data for fly ash was obtained from the Vliegasunie B.V. EPD [115], where coal fly ash is considered a by-product with minimal processing requirements. The impact of ordinary Portland cement (CEM I 42.5N) was derived from the ENCI EPD [116], representing production across the Netherlands and Belgium. Environmental impact data for sodium hydroxide (NaOH), sodium silicate (water glass), and sand were obtained from the NIBE Environmental Database [113]. MSWI bottom ash inventory data was obtained from literature [94]. In accordance with standard LCA practice for waste materials, MSWI BA was allocated no upstream environmental burden as it is a residue from municipal solid waste incineration. However, the environmental impacts of mechanical treatment (grinding and sieving) required to achieve precursor-grade fineness were included in the inventory data, calculated based on energy consumption using Dutch wind power.

Silica fume was assessed using the Ferroglobe EPD (ASTM EPD 636) [117], which classifies silica fume as a recovered by-product from ferrosilicon smelting and does not include the following impact categories and therefore these were excluded from the analysis for silica fume: Human Toxicity Potential, Freshwater Aquatic Ecotoxicity Potential, Marine Aquatic Ecotoxicity Potential, and Terrestrial Ecotoxicity Potential.

6.5 Impact Assessment

In this study, the Life Cycle Impact Assessment (LCIA) was performed using the Environmental Cost Indicator (ECI) method developed under the Dutch SBK framework. This method quantifies the environmental impact of producing 1 m^3 of mortar by converting various impact categories into a single monetary value, expressed in euros per cubic meter (€/m^3). ECI integrates impacts across 11 key environmental categories, including global warming potential, abiotic resource depletion (both elements and fossil), ozone layer depletion, photochemical ozone formation, acidification, eutrophication, and toxicity effects to humans and ecosystems. These categories reflect the most significant environmental burdens associated with construction materials in the Dutch context. In the Table 6.1 Shadow costs of impact categories the shadow costs related to the impact categories can be seen.

The total environmental impact for one cubic meter of mortar is calculated as a weighted sum of the environmental impact factors (F_i) and the mass (M_i) of each constituent material, expressed as $F_{total} = \Sigma F_i \cdot M_i$. Likewise, the ECI value is determined by multiplying the mass of each material per cubic metre of mortar by its respective shadow cost (ECI_i), yielding $ECI = \Sigma ECI_i \cdot M_i$. This cradle-to-gate approach ensures that both the material-specific impacts and their relative proportions in the mix are considered. By applying this method to the selected mortar mixes, the study provides a transparent and standardised assessment of the environmental cost associated with each mix.

The four mortar mixes selected for LCA are:

- 20FA-BFS_0.38: Reference mix from this research
- 20BA-BFS_0.4: Target mix from this research
- 20FA-BFS_0.4: Control mix from this research
- OPC: Ordinary Portland cement mix from literature [112]

Table 6.1 Shadow costs of impact categories.

Impact Category	**Abbreviation**	**Unit Equivalent (UE)**	**Shadow Cost per UE (€)**
Abiotic depletion (non-fuel)	ADP-non fuel	kg Antimony	0.16
Abiotic depletion (fossil)	ADP-fuel	kg Antimony (4.81E-4 kg Antimony/MJ)	0.16
Global warming potential	GWP100	kg CO_2	0.05
Ozone layer depletion	ODP	kg CFC-11	30
Photochemical oxidation	POCP	kg Ethene	2
Acidification	AP	kg SO_2	4
Eutrophication	EP	kg PO_4^{3-}	9
Human toxicity	HTP	kg 1,4-dichlorobenzene	0.09
Fresh water aquatic ecotoxicity	FAETP	kg 1,4-dichlorobenzene	0.03
Marine aquatic ecotoxicity	MAETP	kg 1,4-dichlorobenzene	0.0001
Terrestrial ecotoxicity	TAETP	kg 1,4-dichlorobenzene	0.06

Additionally, the mix design in Table *6.2* shows the weight of the raw materials of the selected mixtures used to prepare 1 m3 of concrete for the LCA analysis and mixture comparison. In this study, all of the selected mixtures have a comparable 28-day compressive strengths with respect to the 3d printable OPC mixture taken from literature [112]. The Figure *6.2* illustrates the compressive strength values of the mixes used for comparison. A slight variation of around 10% was observed between the mixtures. However, this deviation is minimal and considered negligible for the purpose of environmental impact assessment.

Table 6.2 Mix design for life cycle assessment.

Component	**20FA-BFS_0.38 (kg/m³)**	**20FA-BFS_0.4 (kg/m³)**	**20BA-BFS_0.4 (kg/m³)**	**OPC (kg/m³)**
Sand	1127.2	1099.4	1109.5	730.68
Slag	601.5	586.4	591.8	-
Fly Ash	150.3	146.6		208.76
MSWI BA	-	-	147.9	-
Silica Fume	-	-	-	104.38
NaOH solution	60.7	59.2	59.8	-
Na_2SiO_3 solution	73.5	71.7	72.3	-
Water added	207.2	216.7	218.7	365.33

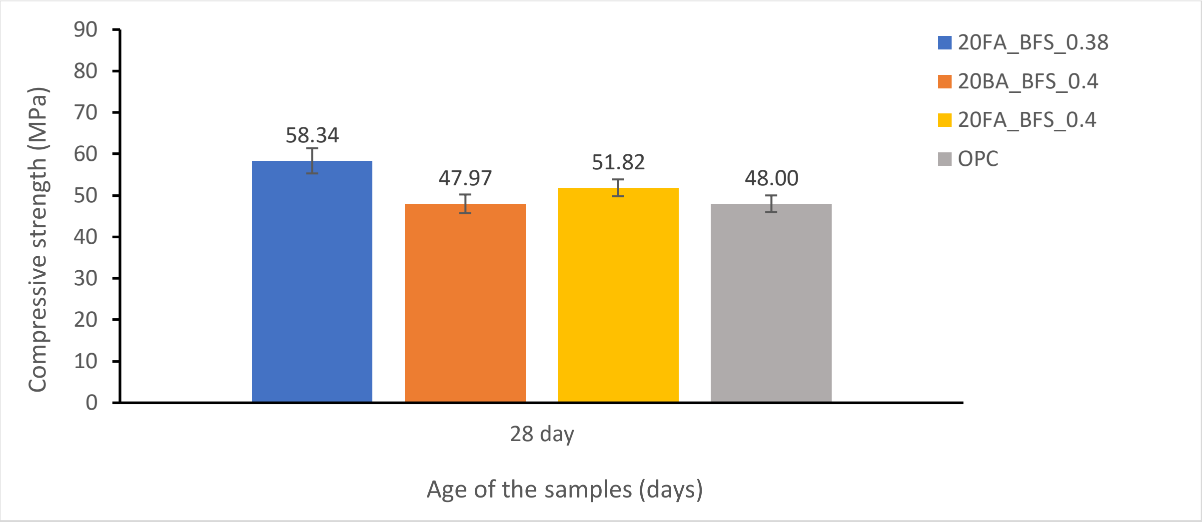

Figure 6.2 28-day compressive strength of selected mortar mixes for LCA.

6.6 Results and Interpretation

The life cycle assessment results presented Figure *6.3* in terms of shadow costs (€/m³), reveal notable differences among the analysed concrete systems. The alkali-activated mixes, namely 20FA-BFS_0.38, 20BA-BFS_0.4, and 20FA-BFS_0.4, recorded significantly lower total environmental costs compared to the OPC-based reference. The OPC mix showed a shadow cost of €33.3/m³, in stark contrast to the AAM systems which ranged between €10.5 – €10.7/m³.

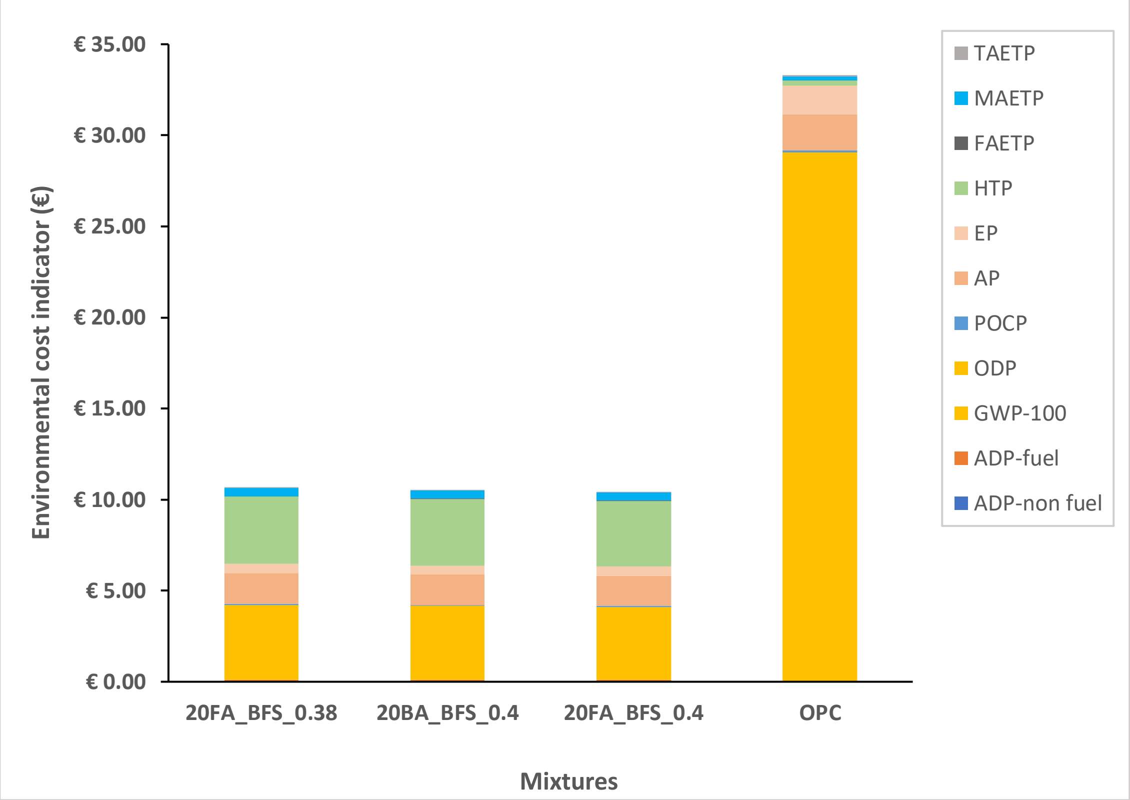

Figure 6.3 Total environmental cost indicators of the selected mortar mixes.

Among the alkali-activated mixes, 20FA-BFS_0.38 exhibited the highest shadow cost (€10.7/m³), followed by 20BA-BFS_0.4 (€10.6/m³), and finally 20FA-BFS_0.4(€10.5/m³) with the lowest at €10.5/m³. The small differences between these AAM systems are attributed to the variations in material densities, which affect the quantity of constituents required to produce 1 m³ of mortar. Despite these variations, the key insight is that both fly ash and MSWI bottom ash cause minimal environmental impact. The dominant contributors to environmental costs in the AAM mixes were the activators, sodium hydroxide and sodium silicate and GGBS.

Figure *6.4* and Figure 6.5 show the effects of the selected mixes on the environmental impact indicators. In terms of individual impact categories, the OPC mix had the highest values for Global Warming Potential (GWP), Human Toxicity Potential (HTP), and Abiotic Depletion (Elements), primarily due to cement and silica fume production. Clinker production, an energy-intensive process involving high CO_2 emissions from both combustion and calcination, significantly drives the GWP in OPC systems. Furthermore, the use of virgin raw materials in OPC manufacturing leads to higher impacts in HTP and fossil resource depletion (ADPF), thereby justifying the substantially higher ECI of the OPC mix.

On the other hand, the alkali-activated mixes, although lower in total ECI, showed noticeable impacts in categories like HTP and marine aquatic ecotoxicity. These were primarily associated with the production of sodium-based activators. Despite their small dosage in the mix, their high shadow cost per kilogram (due to chemical processing and energy use) contributes substantially to the overall impact. GGBS also had a moderate impact across several categories, particularly in ADPF. However, the contributions of fly ash and MSWI BA to environmental impacts remained negligible across all categories, confirming their sustainability advantage.

Notably, MSWI BA performed on par with fly ash in terms of total shadow cost and category wise impact distribution. Its negligible contribution to environmental burdens supports its suitability as an alternative precursor. Given the growing scarcity of fly ash and the increasing push towards circular economy practices in the Dutch construction sector, MSWI BA presents a viable and sustainable option for future 3D printable alkali-activated systems.

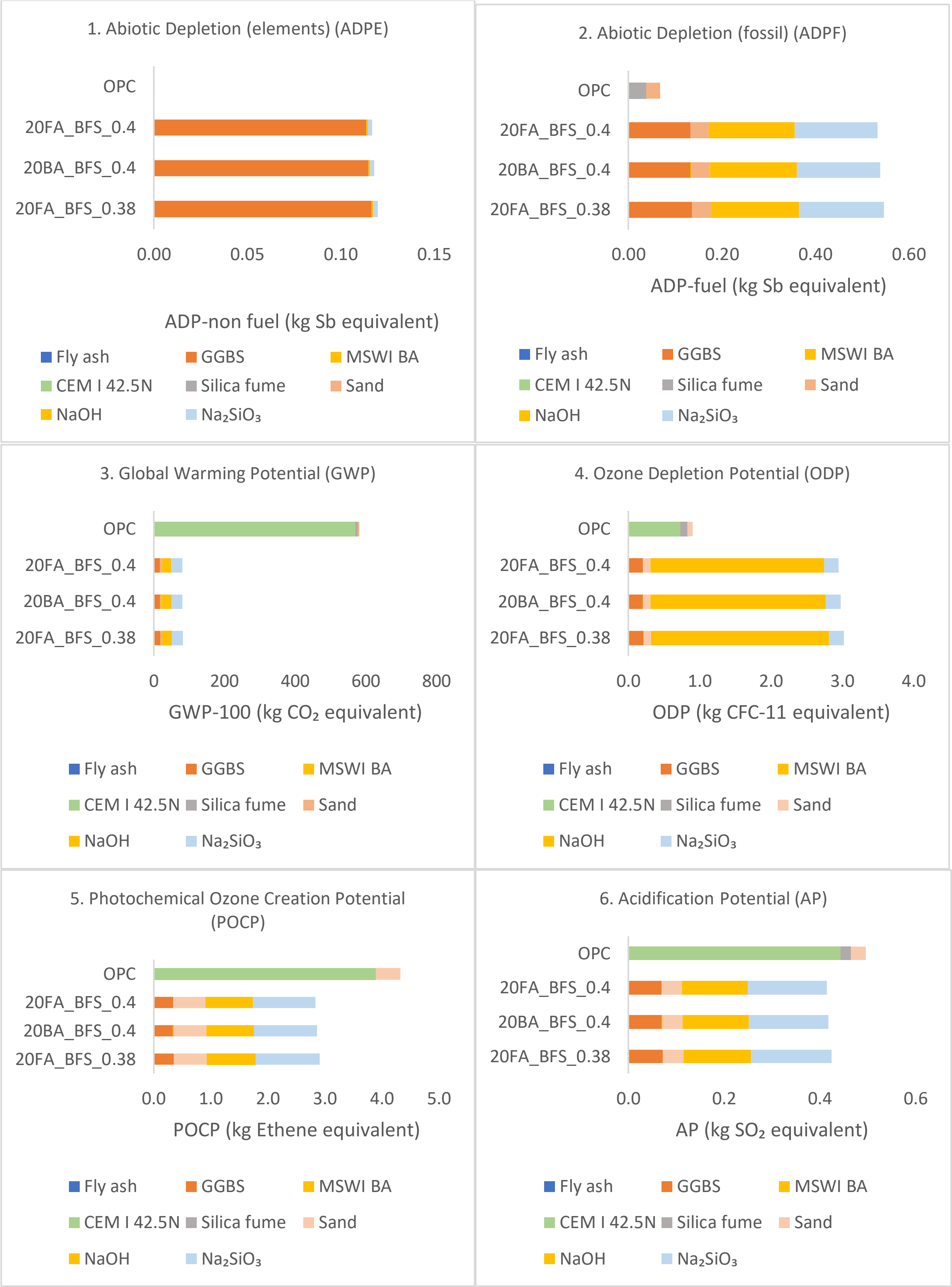

Figure 6.4 Environmental impact indicators of the selected mortar mixes.

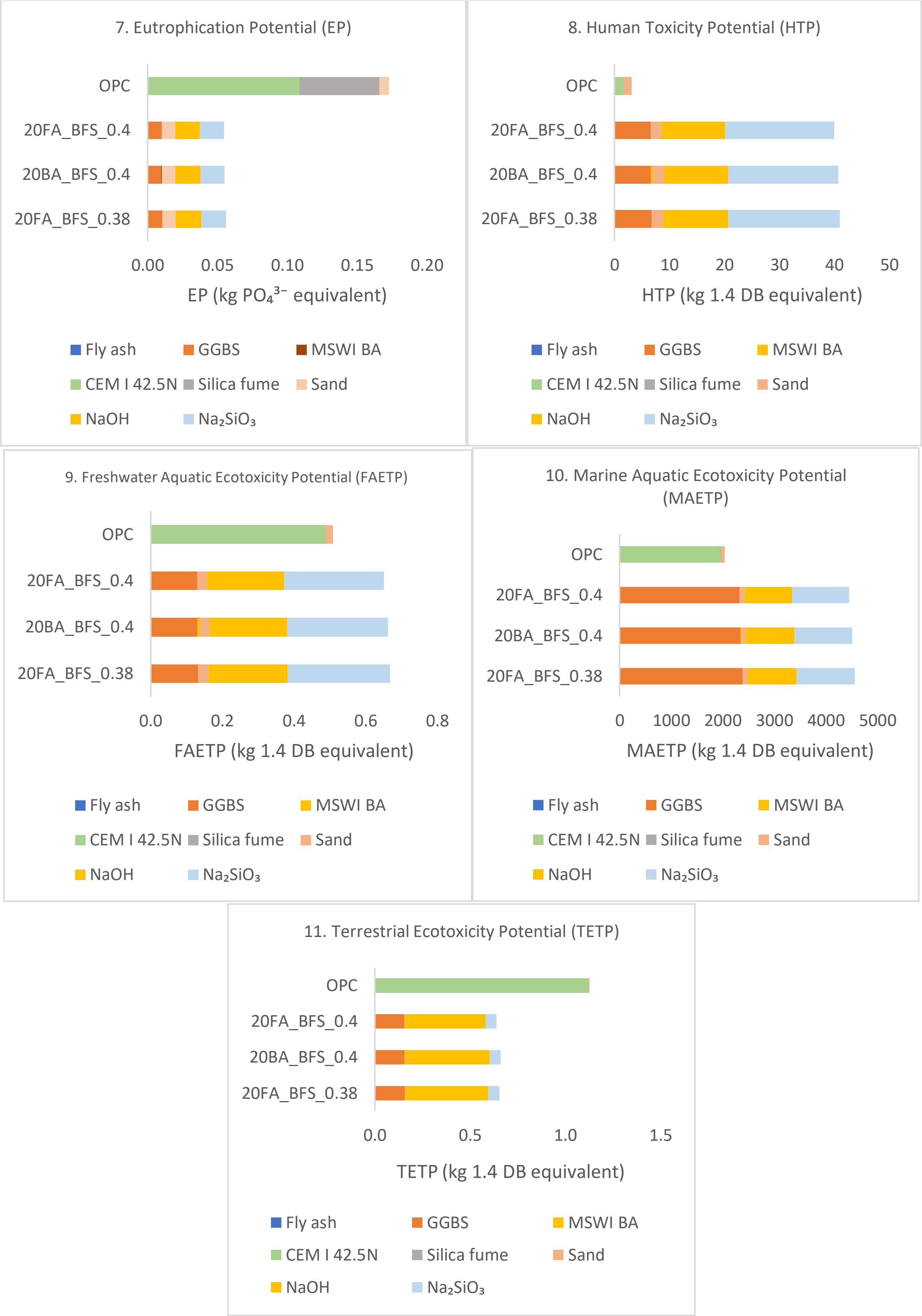

Figure 6.5 Environmental impact indicators of the selected mortar mixes (continued).

6.7 Conclusion

This chapter addressed the goals of comparing the environmental performance of MSWI BA-based mortar with other systems, identifying high-impact components, and quantifying the total shadow cost using the Dutch SBK Environmental Cost Indicator (ECI) method, in accordance with ISO 14040 LCA standards [84].

- The alkali-activated mortar (AAM) mixes incorporating fly ash and MSWI bottom ash demonstrated a substantial reduction in environmental cost (ECI €10.5–€10.7/m^3) compared to the OPC-based reference mix (€33.3/m^3), indicating a potential reduction of nearly 68%.
- Both fly ash and MSWI BA were considered burden-free in the LCA, and their contributions to environmental impact were negligible across all categories. This confirms their sustainability potential when used as precursors.
- The main contributors to the environmental impacts of AAMs were sodium hydroxide, sodium silicate, and GGBS, as these materials are more chemically processed and have higher embodied energy.
- The OPC-based mix recorded the highest impacts in categories like Global Warming Potential (GWP), Human Toxicity Potential (HTP), and Abiotic Depletion, mainly due to clinker and silica fume production.
- MSWI BA performed similarly to FA in both total shadow cost and category-wise impact distribution, supporting its viability as an alternative precursor in light of diminishing FA availability.
- The integration of MSWI BA into AAMs aligns with Dutch sustainability objectives and circular economy principles, offering a promising and environmentally beneficial route for future 3D printable construction materials.

7

General Discussion and Conclusions

7.1 Discussion

This research addressed the critical need municipal solid waste incineration bottom ash as a sustainable alternative to fly ash in alkali-activated slag-based materials, particularly for emerging applications in additive manufacturing. The investigation followed a systematic approach: first establishing an optimized reference mix using conventional fly ash and blast furnace slag precursors, subsequently developing a target mix with municipal solid waste incineration bottom ash replacing fly ash, and finally comparing the rheological behaviour and reaction kinetics of these developed printable mixes to elucidate the fundamental mechanisms governing their printability performance. The findings revealed that MSWI BA incorporation, while necessitating minor mix design adjustments, provided unexpected operational advantages through fundamentally altered reaction kinetics and rheological behaviour, thereby advancing both sustainability objectives and practical applicability for 3D printing operations.

Influence of MSWI BA on Printability Performance

This research successfully developed two 3D printable alkali-activated mortars: a reference mix (20FA-BFS_0.38) comprising 80% blast furnace slag and 20% fly ash with water-to-binder ratio of 0.38, and a target mix (20BA-BFS_0.4) where fly ash was replaced with MSWI bottom ash while maintaining identical chemical parameters except for increased water content (w/b = 0.4). The reference mix served as the benchmark against which the performance of the BA-based target mix was evaluated.

The development of the reference mix (20FA-BFS_0.38) and target mix (20BA-BFS_0.4) followed a structured optimization framework considering buildability, flowability, extrudability, setting time and mechanical strengths. The inclusion of BA required a 5% increase in water-to-binder ratio to achieve comparable buildability and flowability to the reference mix. This demand is attributed to the angular particle morphology and finer size distribution of MSWI BA compared to the spherical FA particles, resulting in higher interparticle friction and specific surface area. Despite this adjustment, the BA-based mix matched the reference mix in buildability and flowability, satisfying essential printability parameters. The mini extrudability test further validated both mixes, showing continuous, stable filament formation with no deformation, confirming suitability for layer-by-layer deposition in 3D printing.

A significant observation was the delayed setting time in the BA-based mix. The 20BA-BFS_0.4 exhibited an initial setting time of 146 minutes, compared to 90 minutes for 20FA-BFS_0.38 and 116 minutes for 20FA-BFS_0.4. This delay is beneficial for extrusion-based 3D printing, providing extended workability without compromising shape stability.

To validate structural adequacy, compressive and flexural strength tests were conducted at 1, 7, and 28 days. The results showed clear strength hierarchy: 20FA-BFS_0.38 > 20FA-BFS_0.4 > 20BA-BFS_0.4 at all ages. The 28-day compressive strength values were 58.6

MPa, 52.2 MPa, and 48.0 MPa respectively. Comparing mixes with identical water content, 20BA-BFS_0.4 showed approximately 8% lower strength than 20FA-BFS_0.4, indicating the direct effect of BA incorporation. Although, incorporation of BA resulted in slightly reduced early strength attributed to slower reaction kinetics, 20BA-BFS_0.4 mix exceeded the target requirements of 45 MPa compressive and 9 MPa flexural strength, confirming structural adequacy.

Influence of MSWI BA on Rheology and Reaction kinetics

To investigate early-age rheological behaviour, yield stress evolution was monitored through slugs test over 140 minutes. Through rheological studies, it was found that early-age structuration in 20FA-BFS_0.38 and 20BA-BFS_0.4 mixes is governed by micromechanical interactions, namely electrostatic repulsion and van der Waals attraction. These forces, in turn, are modulated by the dissolution of precursors and the formation of early reaction products. The evolution of static yield stress clearly demonstrated this interplay: the reference mix exhibited faster structuration and brittle transition by 80 minutes, while the target mix maintained gradual yield stress development, remaining in the printable regime for over 140 minutes. despite its slower evolution, the BA-based mix consistently maintained yield stress within the optimal printable range (400–1000 Pa) throughout the testing window, demonstrating not only sufficient early-age stiffness but also enhanced plastic deformation capacity suitable for layer deposition. This extended plastic deformation capability of the BA-based mix aligns with the longer setting time observed and confirms superior printability. The delayed rheological structuration indicates slower development of the percolated particle network, beneficial for extended printing operations.

To understand the mechanisms underlying gradual yield stress development and extended printable window of BA-based mix, ICP-OES analysis of pore solution was performed. The results showed consistently lower elemental concentrations of key elements (Na, Si, Ca and Mg) in 20BA-BFS_0.4 compared to 20FA-BFS_0.38. The reduced dissolution in 20BA-BFS_0.4 system was attributed to two mechanisms: the dilution effect from 5% higher water content reducing alkalinity of the pore solution, and more significantly, the mobilization of heavy metals (such as Cr, Zn and Pb) from MSWI BA in the high pH environment, which precipitate as metal hydroxides on unreacted slag particle surfaces, thereby hindering the dissolution of the slag. These differences directly influenced rheological behaviour. The higher elemental concentrations in 20FA-BFS_0.38 initially provided stronger electrostatic repulsion, but the rapid consumption of these elements accelerated the transition from repulsion-dominated to attraction-dominated regime, leading to rapid yield stress increase and brittle failure at 80 minutes. In contrast, the lower elemental concentrations and slower consumption rates of elements in 20BA-BFS_0.4 maintained the electrostatic repulsion for an extended period, delaying percolated network formation and enabling continuous slug formation beyond 140 minutes.

To provide insights into gel structure evolution, ATR-FTIR spectroscopy was employed to monitor the Si-O-T absorption band changes. The analysis revealed distinct polymerization dynamics between 20FA-BFS_0.38 and 20BA-BFS_0.4. The FA-based mix showed initial shift of the main band toward lower wavenumbers, followed by progressive shift toward higher wavenumbers, indicating rapid polymerization and formation of cross-linked aluminosilicate networks. In contrast, 20BA-BFS_0.4 maintained the Si-O-T band at consistently lower wavenumbers throughout testing, indicating persistent presence of low-polymerized silicate species (SiQ^1). These negatively charged oligomers adsorbed on particle surfaces maintained electrostatic repulsive forces between particles, delaying percolated network formation. This provides evidence to the rheological behaviour, confirming that the delayed transition to brittle failure results from the fundamentally altered early age reaction kinetics induced by MSWI BA incorporation.

Environmental Impact through Life Cycle Assessment

To evaluate sustainability performance, LCA was conducted comparing the developed AAM mixes with OPC reference mortar. The results indicated significantly lower environmental impact for all AAM systems. Total shadow costs were €10.7/m³ for 20FA-BFS_0.38, €10.6/m³ for 20BA-BFS_0.4, and €10.4/m³ for 20FA-BFS_0.4, compared to €33.3/m³ for OPC mortar. The minimal variation among AAM mixes confirms that MSWI BA substitution does not compromise environmental benefits. The impact breakdown revealed that sodium-based activators contributed the most and FA and BA contributed less than 5% each. The 68% reduction in shadow costs compared to OPC primarily resulted from avoided CO_2 emissions from clinker production. The negligible environmental burden of MSWI BA, combined with waste diversion from landfill, strongly supports its utilization as a sustainable alternative to increasingly scarce fly ash resources.

7.2 Limitations

The limitations of this research are as follows:

- **Material Availability**: Limited MSWI BA quantities restricted the study to laboratory-scale investigations. While mini-extrusion tests provide validated indicators of printability, full-scale 3D printing trials would strengthen conclusions.

- **Printing Validation**: Direct 3D printing demonstration was beyond the scope due to material constraints. However, the comprehensive printability parameters evaluated (slump, flow, extrudability, setting time) are established indicators of printing performance.

- **Mechanical Anisotropy**: Mechanical testing followed standard procedures for cast specimens. The potential anisotropic behaviour typical of 3D printed structures was not assessed.

7.3 Conclusions

This research successfully developed 3D printable alkali-activated mortars incorporating MSWI bottom ash as a replacement for fly ash. The main findings of this research are:

1. MSWI bottom ash can effectively replace fly ash in 3D printable alkali-activated mortars by adjusting the water-to-binder ratio. The BA-based target mix (20BA-BFS_0.4) achieved comparable printability to the FA-based reference mix (20FA-BFS_0.38) with a 5% increase in water content.

   The angular morphology and finer particle size distribution of MSWI BA particles (D_{50} = 6.99 µm) compared to spherical fly ash particles (D_{50} = 45.39 µm) created higher interparticle friction and surface area. This necessitated additional water for adequate particle wetting and lubrication. Despite the morphological differences, 20FA-BFS_0.38 and 20BA-BFS_0.4 mixes satisfied all printability criteria, with both mixes achieving required buildability, flowability, extrudability, setting time and strengths required for 3D printing applications.

2. The incorporation of MSWI BA significantly extends the printable window and provides substantial operational advantages for 3D printing applications.

   Slugs test revealed that the FA-based reference mix exhibited brittle discontinuity at 80 minutes while the BA-based target mix maintained continuous slug formation throughout the 140-minute test period. The extended setting time of 146 minutes compared to 90 minutes for the FA mix confirms this enhanced workability. Throughout this extended working period, the yield stress of the BA-based mix remained within the optimal range for 3D printing while maintaining plastic deformation capability. This characteristic is particularly beneficial for large-scale printing operations.

3. The MSWI BA incorporation fundamentally alters early-age reaction kinetics, with consistently lower concentrations and slower consumption rates of key elements in pore solution indicating delayed polymerization reactions and extended printable window.

   ICP-OES analysis revealed consistently lower elemental concentrations with slower consumption rates of key elements (Na, Si, Ca and Mg) in the BA system indicating reduced precursor dissolution. The reduced dissolution was attributed to two mechanisms: the dilution effect from 5% higher water content reducing alkalinity of the pore solution, and more significantly, the precipitation of metal hydroxides on slag particle surfaces, where heavy metals released by MSWI BA (such as Cr, Zn and Pb) in the high pH environment form metal hydroxides that impede slag dissolution. These conditions sustained the presence of negatively charged species, maintaining electrostatic repulsion dominance throughout the 140-minute test period. This prolonged electrostatic stabilization prevented premature particle aggregation and delayed percolated network formation, maintaining printability for a longer duration.

4. Persistent low-polymerized silicate oligomers maintain electrostatic repulsion forces in BA-based target mix, delaying percolated network formation and extending the printable window. The polymerization dynamics of the Si-O-T band provide explanation for the distinct rheological behaviours of the two developed 3D printable mixes.

   FTIR spectroscopy revealed that the BA system maintained the Si-O-T absorption band at consistently low wavenumbers throughout testing, indicating persistent dominance of low-polymerized, negatively charged silicate oligomers (SiQ^1). These oligomers adsorb onto particle surfaces, significantly enhancing electrostatic inter-particle repulsive forces that prevent close particle approach and delay percolated network development. In contrast, the FA-based reference mix exhibited rapid polymerization with the band gradually shifting towards higher wavenumbers, indicating transition towards polymerized species (SiQ^2). This faster polymerization reduced electrostatic repulsion between particles, allowing attractive colloidal forces to dominate and promoting rapid interparticle bridging.

5. MSWI BA provides equivalent environmental performance to fly ash while offering superior waste valorisation benefits. The negligible environmental burden of BA confirms its suitability as a sustainable precursor for alkali-activated materials.

   Life cycle assessment revealed total shadow costs of €10.6/m^3 for the 20BA-BFS_0.4 mix compared to €10.7/m^3 for 20BA-BFS_0.4 mix, both representing 68% reduction compared to OPC mortar (€33.3/m^3). The environmental impact was dominated by alkali activators (65-70%) and GGBS (25-30%), while both FA and BA contributed less than 5%. The comparable performance between waste-derived precursors, combined with landfill diversion benefits and increasing scarcity of quality fly ash, strongly supports BA utilization in sustainable construction materials.

7.4 Recommendations

- **Comprehensive Rheological Characterization:** Future studies should investigate viscosity evolution and thixotropic behaviour to understand the complete flow response during 3D printing. The influence of shear history on microstructural development should be examined, as varying shear rates during pumping and extrusion may alter particle alignment and gel formation.

- **Contact Force Mechanisms**: Investigation of how particle morphology and water content govern interparticle contact forces in MSWI BA systems would provide fundamental understanding for rheological control. Studies correlating particle shape parameters, water film thickness, and resulting contact mechanics through advanced rheometry could guide mix design optimization.

- **Printing Process Scale-Up:** The printability tests in this research were conducted at laboratory scale (manual mini-extrusion and small specimens). To bridge the gap to practical application, it’s recommended to perform trials using larger scale printing setups.

- **Temperature Effects**: The influence of processing temperature requires investigation as alkali-activated materials show high temperature sensitivity. Heat generation in rotor-stator pumps caused by friction may raise material temperature by few degrees, potentially accelerating reactions. Real-time temperature monitoring and development of temperature-compensated mix designs are needed for consistent performance.

- **Durability and Performance**: Extend the investigation to include shrinkage, creep, and durability under cyclic and environmental loading conditions. This is crucial for validating the long-term structural reliability of MSWI BA-based 3D printed elements.

A.

Appendix

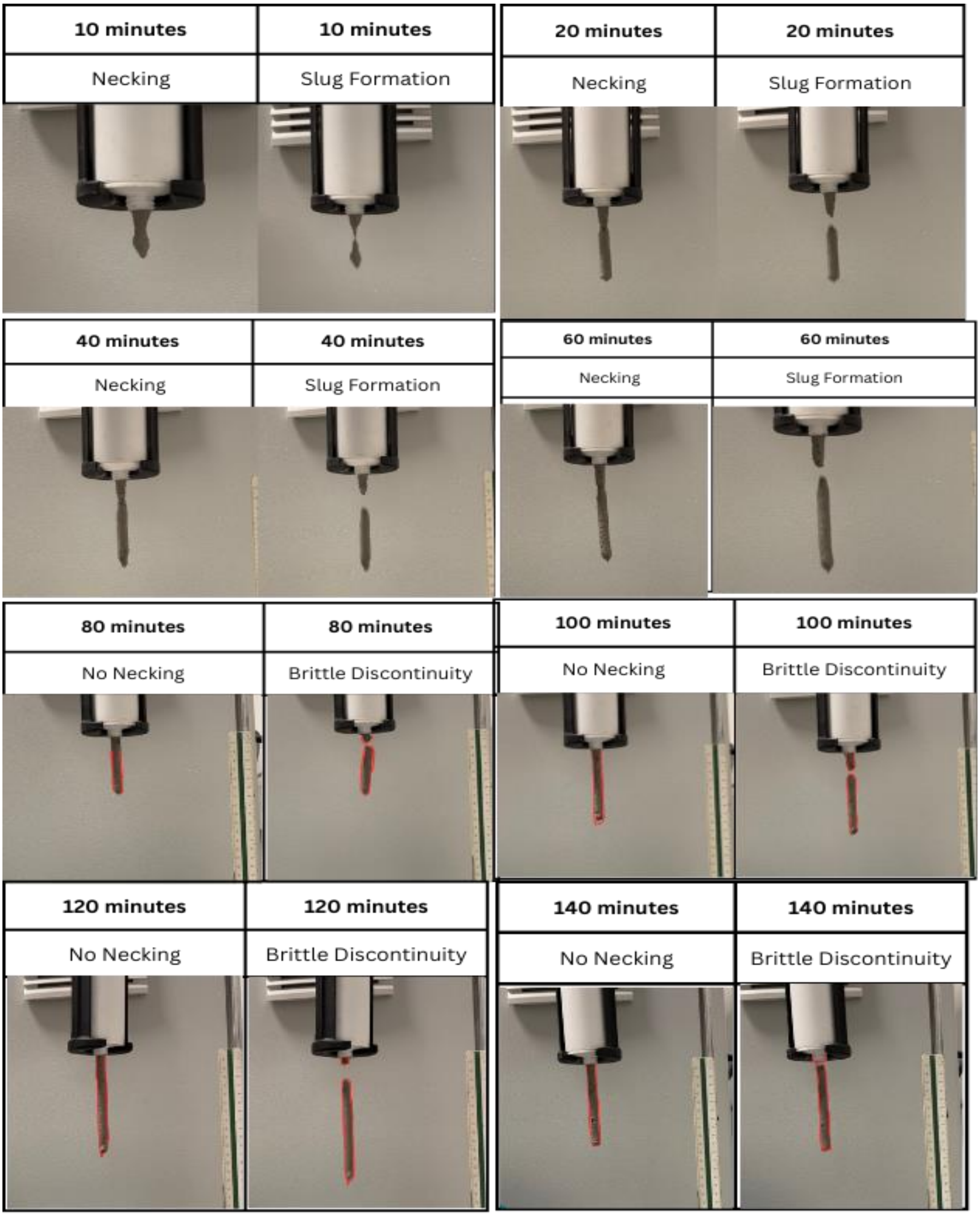

Figure A.1 Slugs test images with respect to time for reference mix (20FA-BFS_0.38).

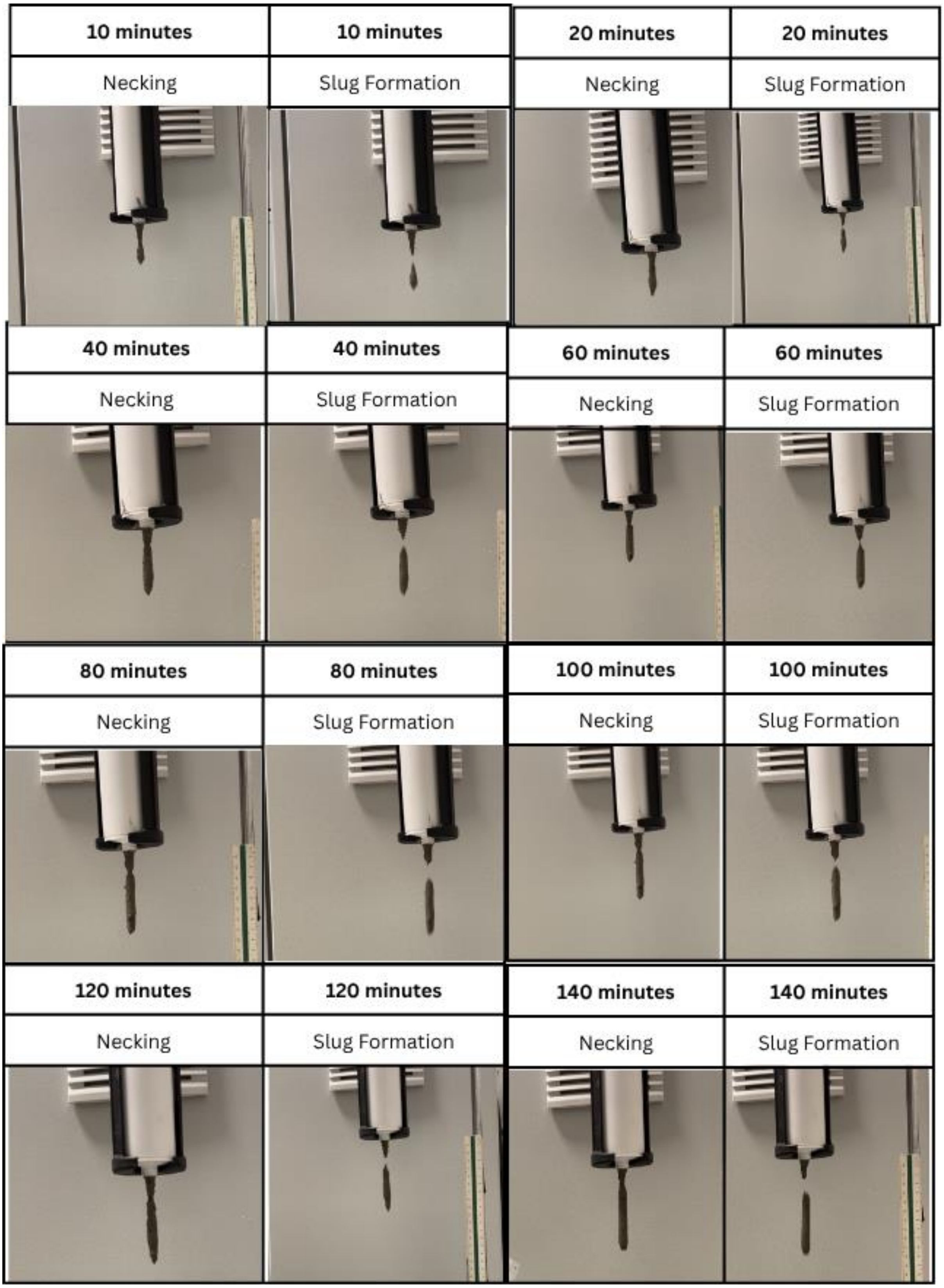

Figure A.2 Slugs test images with respect to time for target mix (20BA-BFS_0.4).

B.

Appendix

Table B.1 Environmental indicator equivalents of the materials [113], [114], [115], [116], [117].

Environmental Impact Indicator	Abbreviation	FA	BFS	MSWI BA	CEM I 42.5N	Silica Fume	Sand
Abiotic Depletion (elements)	ADP-non fuel	1.26E-09	1.94E-04	1.21E-07	6.80E-08	5.60E-08	1.70E-09
Abiotic Depletion (fossil)	ADP-fuel	8.42E-06	2.26E-04	1.35E-05	5.82E-07	3.66E-04	3.50E-05
Global Warming Potential	GWP-100	1.33E-03	3.03E-02	2.01E-03	7.82E-01	5.20E-02	5.08E-03
Ozone Depletion Potential	ODP	1.94E-10	3.47E-09	1.05E-10	9.89E-09	9.60E-09	9.15E-10
Photochemical Ozone Creation Potential	POCP	7.72E-07	5.68E-06	1.01E-06	5.33E-05	0.00E+00	5.12E-06
Acidification Potential	AP	9.57E-06	1.17E-04	1.02E-05	6.08E-04	1.95E-04	3.84E-05
Eutrophication Potential	EP	2.11E-06	1.67E-05	1.16E-06	1.49E-04	5.45E-04	8.61E-06
Human Toxicity Potential	HTP	3.40E-04	1.12E-02	2.50E-03	2.29E-03	0.00E+00	1.80E-03
Freshwater Aquatic Ecotoxicity Potential	FAETP	7.98E-06	2.20E-04	4.24E-05	6.68E-04	0.00E+00	2.51E-05
Marine Aquatic Ecotoxicity Potential	MAETP	2.48E-02	3.97E+00	1.26E-01	2.70E+00	0.00E+00	8.52E-02
Terrestrial Ecotoxicity Potential	TAETP	5.13E-06	2.62E-04	1.18E-04	1.54E-03	0.00E+00	3.00E-06

Table B.1 Environmental indicator equivalents of the materials [113], [114], [115], [116], [117] (Continued).

Environmental Impact Indicator	Abbreviation	NaOH (50% wt%)	Water Glass (45% wt%)
Abiotic Depletion (elements)	ADP-non fuel	1.33E-05	3.24E-05
Abiotic Depletion (fossil)	ADP-fuel	3.12E-03	2.47E-03
Global Warming Potential	GWP-100	4.37E-01	4.29E-01
Ozone Depletion Potential	ODP	4.12E-07	2.93E-08
Photochemical Ozone Creation Potential	POCP	1.41E-04	1.53E-04
Acidification Potential	AP	2.32E-03	2.30E-03
Eutrophication Potential	EP	3.02E-04	2.39E-04
Human Toxicity Potential	HTP	1.96E-01	2.77E-01
Freshwater Aquatic Ecotoxicity Potential	FAETP	3.63E-03	3.88E-03
Marine Aquatic Ecotoxicity Potential	MAETP	1.56E+01	1.54E+01
Terrestrial Ecotoxicity Potential	TAETP	7.15E-03	7.97E-04

References

[1] S. Bhusal and S. Kshirsagar, “Comparison of Construction with Traditional Method and 3D Printing Technology,” *IRE Journals*, vol. 3, no. 11, pp. 93–97, May 2020, Accessed: Aug. 11, 2024. [Online]. Available: https://www.irejournals.com/formatedpaper/1702297.pdf

[2] G. H. Ahmed, N. H. Askandar, and G. B. Jumaa, “A review of largescale 3DCP: Material characteristics, mix design, printing process, and reinforcement strategies,” *Structures*, vol. 43, pp. 508–532, Sep. 2022, doi: 10.1016/j.istruc.2022.06.068.

[3] J. Zhang, J. Wang, S. Dong, X. Yu, and B. Han, “A review of the current progress and application of 3D printed concrete,” *Compos Part A Appl Sci Manuf*, vol. 125, Oct. 2019, doi: 10.1016/j.compositesa.2019.105533.

[4] A. K. Al-Tamimi, H. H. Alqamish, A. Khaldoune, H. Alhaidary, and K. Shirvanimoghaddam, “Framework of 3D Concrete Printing Potential and Challenges,” *Buildings*, vol. 13, no. 3, Mar. 2023, doi: 10.3390/buildings13030827.

[5] H. Zhong and M. Zhang, “3D printing geopolymers: A review,” *Cem Concr Compos*, vol. 128, no. 3, Feb. 2022, doi: 10.1016/j.cemconcomp.2022.104455.

[6] A. U. Rehman and J. H. Kim, “3D Concrete Printing: A Systematic Review of Rheology, Mix Designs, Mechanical, Microstructural, and Durability Characteristics,” *Materials*, vol. 14, no. 14, Jul. 2021, doi: 10.3390/ma14143800.

[7] C. R. Rollakanti and C. V. S. R. Prasad, “Applications, performance, challenges and current progress of 3D concrete printing technologies as the future of sustainable construction – A state of the art review,” in *Materials Today: Proceedings*, Elsevier Ltd, Jan. 2022, pp. 995–1000. doi: 10.1016/j.matpr.2022.03.619.

[8] Silpa Kaza, Lisa C. Yao, Perinaz Bhada-Tata, and Frank Van Woerden, *What a Waste 2.0: A Global Snapshot of Solid Waste Management to 2050*. World Bank, 2018. doi: 10.1596/978-1-4648-1329-0.

[9] B. Chen *et al.*, “Reactivity and leaching potential of municipal solid waste incineration (MSWI) bottom ash as supplementary cementitious material and precursor for alkali-activated materials,” *Constr Build Mater*, vol. 409, Dec. 2023, doi: 10.1016/j.conbuildmat.2023.133890.

[10] A. U. Rehman, S. M. Lee, and J. H. Kim, “Use of municipal solid waste incineration ash in 3D printable concrete,” *Process Safety and Environmental Protection*, vol. 142, pp. 219–228, Oct. 2020, doi: 10.1016/j.psep.2020.06.018.

[11] M. Xia and J. Sanjayan, “Method of formulating geopolymer for 3D printing for construction applications,” *Mater Des*, vol. 110, pp. 382–390, Nov. 2016, doi: 10.1016/j.matdes.2016.07.136.

[12] A. Perrot, *3D printing of concrete : state of the art and challenges of the digital construction revolution*. John Wiley & Sons, 2019. doi: 10.1002/9781119610755.

[13] S. Neudecker *et al.*, “A New Robotic Spray Technology for Generative Manufacturing of Complex Concrete Structures Without Formwork,” in *Procedia CIRP*, Elsevier B.V., 2016, pp. 333–338. doi: 10.1016/j.procir.2016.02.107.

[14] F. Heidarnezhad and Q. Zhang, “Shotcrete based 3D concrete printing: State of art, challenges, and opportunities,” *Constr Build Mater*, vol. 323, Mar. 2022, doi: 10.1016/j.conbuildmat.2022.126545.

[15] J. Burger *et al.*, “Eggshell: Ultra-thin three-dimensional printed formwork for concrete structures,” *3D Print Addit Manuf*, vol. 7, no. 2, pp. 49–59, Apr. 2020, doi: 10.1089/3dp.2019.0197.

[16] E. Lloret *et al.*, “Complex concrete structures: Merging existing casting techniques with digital fabrication,” *CAD Computer Aided Design*, vol. 60, pp. 40–49, 2015, doi: 10.1016/j.cad.2014.02.011.

[17] E. Lloret, E. Zurich, L. Reiter, T. P. Wangler, and R. J. Flatt, “Smart Dynamic Casting Slipforming with Flexible Formwork-Inline Measurement and Control,” in *Second Concrete Innovation Conference (2nd CIC)*, Tromsø, Mar. 2017, p. 27. doi: 10.3929/ethz-b-000219663.

[18] F. Scotto, E. L. Fritschi, F. Gramazio, M. Kohler, and R. J. Flatt, “Adaptive Control System for Smart Dynamic Casting - Defining Fabrication-Informed Design Tools and Process Parameters in Digital Fabrication Processes,” in *CAADRIA 2018 - Learning, Adapting, Prototyping*, Beijing, May 2018, pp. 255–264. doi: 10.52842/conf.caadria.2018.1.255.

[19] P. Pfändler, T. Wangler, J. Mata-Falcón, and W. K. R. J. Flatt, “Potentials of Steel Fibres for Mesh Mould Elements,” in *First RILEM International Conference on Concrete and Digital Fabrication – Digital Concrete 2018*, Timothy Wangler and Robert J. Flatt, Eds., Springer, Cham, Aug. 2018, pp. 207–216. doi: 10.1007/978-3-319-99519-9_19.

[20] A. Yahia, S. Mantellato, and R. J. Flatt, “Concrete rheology: A basis for understanding chemical admixtures,” in *Science and Technology of Concrete Admixtures*, Elsevier Inc., 2016, ch. 7, pp. 97–127. doi: 10.1016/B978-0-08-100693-1.00007-2.

[21] R. Mandal, S. K. Panda, and S. Nayak, “Rheology of Concrete: Critical Review, recent Advancements, and future prospectives,” *Constr Build Mater*, vol. 392, Aug. 2023, doi: 10.1016/j.conbuildmat.2023.132007.

[22] A. R. Arunothayan, B. Nematollahi, K. H. Khayat, A. Ramesh, and J. G. Sanjayan, “Rheological characterization of ultra-high performance concrete for 3D printing,” *Cem Concr Compos*, vol. 136, Feb. 2023, doi: 10.1016/j.cemconcomp.2022.104854.

[23] “Viscosity of Newtonian and Non-Newtonian Fluids.” Accessed: Aug. 15, 2024. [Online]. Available: https://www.rheosense.com/applications/viscosity/newtonian-non-newtonian

[24] P. C. Barman, R. R. Kairi, A. Das, and R. Islam, “An Overview of Non-Newtonian Fluid,” *International Journal of Applied Science and Engineering*, vol. 4, no. 2, p. 97, 2016, doi: 10.5958/2322-0465.2016.00011.3.

[25] C. Zhang *et al.*, “Mix design concepts for 3D printable concrete: A review,” *Cem Concr Compos*, vol. 122, no. 2, Sep. 2021, doi: 10.1016/j.cemconcomp.2021.104155.

[26] Y. Mortada, M. Mohammad, B. Mansoor, Z. Grasley, and E. Masad, “Development of Test Methods to Evaluate the Printability of Concrete Materials for Additive Manufacturing,” *Materials*, vol. 15, no. 18, Sep. 2022, doi: 10.3390/ma15186486.

[27] N. Roussel, A. Lemaître, R. J. Flatt, and P. Coussot, “Steady state flow of cement suspensions: A micromechanical state of the art,” *Cem Concr Res*, vol. 40, no. 1, pp. 77–84, Jan. 2010, doi: 10.1016/j.cemconres.2009.08.026.

[28] X. Dai, S. Aydin, M. Yücel Yardimci, R. E. N. Qiang, K. Lesage, and G. De Schutter, “Rheology, early-age hydration and microstructure of alkali-activated GGBFS-Fly ash-limestone mixtures,” *Cem Concr Compos*, vol. 124, Nov. 2021, doi: 10.1016/j.cemconcomp.2021.104244.

[29] C. Lu, Z. Zhang, J. Hu, Q. Yu, and C. Shi, “Relationship between rheological property and early age-microstructure building up of alkali-activated slag,” *Compos B Eng*, vol. 247, Dec. 2022, doi: 10.1016/j.compositesb.2022.110271.

[30] C. Wang, O. Kayali, and J.-L. Liow, “Effect of electrostatic repulsion induced by superplasticizers on the flow behaviour of fly ash pastes,” in *Fifth International Conference on Sustainable Construction Materials and Technologies*, Jan. 2019. doi: 10.18552/2019/IDSCMT5020.

[31] Z. Li, I. Alfredo Flores Beltran, Y. Chen, B. Šavija, and G. Ye, “Early-age properties of alkali-activated slag and glass wool paste,” *Constr Build Mater*, vol. 291, Jul. 2021, doi: 10.1016/j.conbuildmat.2021.123326.

[32] P. P. Saklecha, R. S. Kedar, and A. Professor, “Review on Ground Granulated Blast-Furnace Slag as a Supplementary Cementitious Material,” in *International Conference on Quality Up-gradation in Engineering, Science and Technology (ICQUEST2015)*, International Journal of Computer Applications, 2015.

[33] I. Yuksel, “Blast-furnace slag,” in *Waste and Supplementary Cementitious Materials in Concrete: Characterisation, Properties and Applications*, Elsevier, 2018, ch. 12, pp. 361–415. doi: 10.1016/B978-0-08-102156-9.00012-2.

[34] J. Skočibušić Pejić, M. Grubor, M. Serdar, M. Schmid, and G. Walenta, “Assessing Chemical Reactivity of Blast Furnace Slags as Supplementary Cementitious,” in *Doctoral Symposium in Civil Engineering*, Sep. 2021. [Online]. Available: https://www.researchgate.net/publication/360567123

[35] F. Hussain, I. Kaur, and A. Hussain, “Reviewing the influence of GGBFS on concrete properties,” in *Materials Today: Proceedings*, Elsevier Ltd, Jan. 2020, pp. 997–1004. doi: 10.1016/j.matpr.2020.07.410.

[36] G. Li *et al.*, “Fly Ash Application as Supplementary Cementitious Material: A Review,” *Materials*, vol. 15, no. 7, Apr. 2022, doi: 10.3390/ma15072664.

[37] S. V. Vassilev and C. G. Vassileva, “A new approach for the classification of coal fly ashes based on their origin, composition, properties, and behaviour,” *Fuel*, vol. 86, no. 10–11, pp. 1490–1512, Jul. 2007, doi: 10.1016/j.fuel.2006.11.020.

[38] A. Bhatt, S. Priyadarshini, A. Acharath Mohanakrishnan, A. Abri, M. Sattler, and S. Techapaphawit, “Physical, chemical, and geotechnical properties of coal fly ash: A global review,” *Case Studies in Construction Materials*, vol. 11, Dec. 2019, doi: 10.1016/j.cscm.2019.e00263.

[39] O. E. Manz, “Coal fly ash: a retrospective and future look,” *Fuel*, vol. 78, no. 2, pp. 133–136, Jan. 1999, doi: 10.1016/s0016-2361(98)00148-3.

[40] B. Chen, P. Perumal, M. Illikainen, and G. Ye, “A review on the utilization of municipal solid waste incineration (MSWI) bottom ash as a mineral resource for construction materials,” *Journal of Building Engineering*, vol. 71, Jul. 2023, doi: 10.1016/j.jobe.2023.106386.

[41] J. Li, “Municipal solid waste incineration ash-incorporated concrete: One step towards environmental justice,” *Buildings*, vol. 11, no. 11, Nov. 2021, doi: 10.3390/buildings11110495.

[42] D. Chen *et al.*, “Municipal solid waste incineration residues recycled for typical construction materials- a review,” *RSC Adv*, vol. 12, no. 10, pp. 6279–6291, Feb. 2022, doi: 10.1039/d1ra08050d.

[43] M. T. Marvila, A. R. G. de Azevedo, and C. M. F. Vieira, “Reaction mechanisms of alkali-activated materials,” *Revista IBRACON de Estruturas e Materiais*, vol. 14, no. 3, 2021, doi: 10.1590/s1983-41952021000300009.

[44] Y. Sun, Z. Liu, S. Ghorbani, G. Ye, and G. De Schutter, “Fresh and hardened properties of alkali-activated slag concrete: The effect of fly ash as a supplementary precursor,” *J Clean Prod*, vol. 370, Oct. 2022, doi: 10.1016/j.jclepro.2022.133362.

[45] B. Sun, G. Ye, and G. de Schutter, “A review: Reaction mechanism and strength of slag and fly ash-based alkali-activated materials,” *Constr Build Mater*, vol. 326, Apr. 2022, doi: 10.1016/j.conbuildmat.2022.126843.

[46] T. Yang, H. Zhu, Z. Zhang, X. Gao, C. Zhang, and Q. Wu, “Effect of fly ash microsphere on the rheology and microstructure of alkali-activated fly ash/slag pastes,” *Cem Concr Res*, vol. 109, pp. 198–207, Jul. 2018, doi: 10.1016/j.cemconres.2018.04.008.

[47] S. M. Laskar and S. Talukdar, “Preparation and tests for workability, compressive and bond strength of ultra-fine slag based geopolymer as concrete repairing agent,” *Constr Build Mater*, vol. 154, pp. 176–190, Nov. 2017, doi: 10.1016/j.conbuildmat.2017.07.187.

[48] L. Ting, W. Qiang, and Z. Shiyu, “Effects of ultra-fine ground granulated blast-furnace slag on initial setting time, fluidity and rheological properties of cement pastes,” *Powder Technol*, vol. 345, pp. 54–63, Mar. 2019, doi: 10.1016/j.powtec.2018.12.094.

[49] F. Collins and J. G. Sanjayan, “Effects of ultra-fine materials on workability and strength of concrete containing alkali-activated slag as the binder,” *Cem Concr Res*, vol. 29, pp. 459–462, 1999, doi: 10.1016/s0008-8846(98)00237-3.

[50] A. Bourliva *et al.*, “Enrichment and oral bioaccessibility of selected trace elements in fly ash-derived magnetic components,” *Environmental Science and Pollution Research*, vol. 24, no. 3, pp. 2337–2349, Jan. 2017, doi: 10.1007/s11356-016-7967-4.

[51] S. Diamond, “Particle morphologies in fly ash,” *Cem Concr Res*, vol. 16, no. 4, pp. 569–579, Jul. 1986, doi: 10.1016/0008-8846(86)90095-5.

[52] F. Goodarzi and H. Sanei, “Plerosphere and its role in reduction of emitted fine fly ash particles from pulverized coal-fired power plants,” *Fuel*, vol. 88, no. 2, pp. 382–386, Feb. 2009, doi: 10.1016/j.fuel.2008.08.015.

[53] J. Ma, D. Wang, S. Zhao, P. Duan, and S. Yang, “Influence of particle morphology of ground fly ash on the fluidity and strength of cement paste,” *Materials*, vol. 14, no. 2, pp. 1–18, Jan. 2021, doi: 10.3390/ma14020283.

[54] T. He, Z. Li, S. Zhao, X. Zhao, and X. Qu, “Study on the particle morphology, powder characteristics and hydration activity of blast furnace slag prepared by different grinding methods,” *Constr Build Mater*, vol. 270, Feb. 2021, doi: 10.1016/j.conbuildmat.2020.121445.

[55] R. Xiao, X. Jiang, M. Zhang, P. Polaczyk, and B. Huang, “Analytical investigation of phase assemblages of alkali-activated materials in CaO-SiO2-Al2O3 systems: The management of reaction products and designing of precursors,” *Mater Des*, vol. 194, Sep. 2020, doi: 10.1016/j.matdes.2020.108975.

[56] S. Kucharczyk, M. Sitarz, M. Zajac, and J. Deja, “The effect of CaO/SiO2 molar ratio of CaO-Al2O3-SiO2 glasses on their structure and reactivity in alkali activated system,” *Spectrochim Acta A Mol Biomol Spectrosc*, vol. 194, pp. 163–171, Apr. 2018, doi: 10.1016/j.saa.2018.01.018.

[57] K. Gong and C. E. White, “Predicting CaO-(MgO)-Al2O3-SiO2 glass reactivity in alkaline environments from force field molecular dynamics simulations,” *Cem Concr Res*, vol. 150, Dec. 2021, doi: 10.1016/j.cemconres.2021.106588.

[58] B. Chen *et al.*, “Reactivity and leaching potential of municipal solid waste incineration (MSWI) bottom ash as supplementary cementitious material and precursor for alkali-activated materials,” *Constr Build Mater*, vol. 409, Dec. 2023, doi: 10.1016/j.conbuildmat.2023.133890.

[59] A. Mary Joseph, R. Snellings, P. Nielsen, S. Matthys, and N. De Belie, “Pre-treatment and utilisation of municipal solid waste incineration bottom ashes towards a circular economy,” *Constr Build Mater*, vol. 260, Nov. 2020, doi: 10.1016/j.conbuildmat.2020.120485.

[60] B. Sun, Y. Sun, G. Ye, and G. De Schutter, “A mix design methodology of slag and fly ash-based alkali-activated paste,” *Cem Concr Compos*, vol. 126, Feb. 2022, doi: 10.1016/j.cemconcomp.2021.104368.

[61] Y. W. D. Tay, Y. Qian, and M. J. Tan, “Printability region for 3D concrete printing using slump and slump flow test,” *Compos B Eng*, vol. 174, Oct. 2019, doi: 10.1016/j.compositesb.2019.106968.

[62] “ASTM C1437-20,” *ASTM International*. doi: 10.1520/C1437.

[63] “ASTM C230/C230M − 20,” *ASTM International*. doi: 10.1520/C0230_C0230M-13.

[64] M. V. Tran, T. H. Vu, and T. H. Y. Nguyen, “Simplified assessment for one-part 3D-printable geopolymer concrete based on slump and slump flow measurements,” *Case Studies in Construction Materials*, vol. 18, Jul. 2023, doi: 10.1016/j.cscm.2023.e01889.

[65] Y. Chen *et al.*, “Improving printability of limestone-calcined clay-based cementitious materials by using viscosity-modifying admixture,” *Cem Concr Res*, vol. 132, Jun. 2020, doi: 10.1016/j.cemconres.2020.106040.

[66] K. Kim, S. Park, W. S. Kim, Y. Jeong, and J. Lee, “Evaluation of shear strength of RC beams with multiple interfaces formed before initial setting using 3D printing technology,” *Materials*, vol. 10, no. 12, Nov. 2017, doi: 10.3390/ma10121349.

[67] A. Antoni *et al.*, “Investigation of the material mixtures and fiber addition for 3D concrete printing,” in *IOP Conference Series: Earth and Environmental Science*, IOP Publishing Ltd, Nov. 2021. doi: 10.1088/1755-1315/907/1/012011.

[68] "NEN-EN 480-2:2006 en", Accessed: Sep. 08, 2024. [Online]. Available: https://www.nen.nl/en/nen-en-480-2-2006-en-108648

[69] "NEN-EN 196-1:2016 en", Accessed: Mar. 01, 2024. [Online]. Available: https://www.nen.nl/en/nen-en-196-1-2016-en-219352

[70] Y. Sun *et al.*, "A conceptual design of two-stream alkali-activated materials," *Cem Concr Compos*, vol. 148, Apr. 2024, doi: 10.1016/j.cemconcomp.2024.105485.

[71] X. Dai, Y. Tao, Y. Zhang, L. Ding, K. Van Tittelboom, and G. De Schutter, "Development of 3D printable alkali-activated slag-metakaolin concrete," *Constr Build Mater*, vol. 444, Sep. 2024, doi: 10.1016/j.conbuildmat.2024.137775.

[72] N. Ducoulombier *et al.*, "The 'Slugs-test' for extrusion-based additive manufacturing: Protocol, analysis and practical limits," *Cem Concr Compos*, vol. 121, Aug. 2021, doi: 10.1016/j.cemconcomp.2021.104074.

[73] F. Caruso, S. Mantellato, M. Palacios, and R. J. Flatt, "ICP-OES method for the characterization of cement pore solutions and their modification by polycarboxylate-based superplasticizers," *Cem Concr Res*, vol. 91, pp. 52–60, Jan. 2017, doi: 10.1016/j.cemconres.2016.10.007.

[74] H. Sallehi, P. Ghods, and O. B. Isgor, "Formation factor of fresh cementitious pastes," *Cem Concr Compos*, vol. 91, pp. 174–188, Aug. 2018, doi: 10.1016/j.cemconcomp.2018.05.011.

[75] B. Lothenbach *et al.*, "Cemdata18: A chemical thermodynamic database for hydrated Portland cements and alkali-activated materials," *Cem Concr Res*, vol. 115, pp. 472–506, Jan. 2019, doi: 10.1016/j.cemconres.2018.04.018.

[76] Y. Chen *et al.*, "Synthesis, solubility and thermodynamic properties of N-A-S-H gels with various target Si/Al ratios," *Cem Concr Res*, vol. 180, Jun. 2024, doi: 10.1016/j.cemconres.2024.107484.

[77] Y. Chen *et al.*, "Thermodynamic modeling of alkali-activated fly ash paste," *Cem Concr Res*, vol. 186, Dec. 2024, doi: 10.1016/j.cemconres.2024.107699.

[78] B. Lothenbach, "Thermodynamic equilibrium calculations in cementitious systems," *Materials and Structures/Materiaux et Constructions*, vol. 43, no. 10, pp. 1413–1433, Dec. 2010, doi: 10.1617/s11527-010-9592-x.

[79] C. Zhang, H. Khorshidi, E. Najafi, and M. Ghasemi, "Fresh, mechanical and microstructural properties of alkali-activated composites incorporating nanomaterials: A comprehensive review," *J Clean Prod*, vol. 384, Jan. 2023, doi: 10.1016/j.jclepro.2022.135390.

[80] J. Zhang, C. Shi, and Z. Zhang, "Carbonation induced phase evolution in alkali-activated slag/fly ash cements: The effect of silicate modulus of activators," *Constr Build Mater*, vol. 223, pp. 566–582, Oct. 2019, doi: 10.1016/j.conbuildmat.2019.07.024.

[81] S. Onutai, T. Osugi, and T. Sone, "Alumino-Silicate Structural Formation during Alkali-Activation of Metakaolin: In-Situ and Ex-Situ ATR-FTIR Studies," *Materials*, vol. 16, no. 3, Feb. 2023, doi: 10.3390/ma16030985.

[82] R. Ylmén, U. Jäglid, B. M. Steenari, and I. Panas, "Early hydration and setting of Portland cement monitored by IR, SEM and Vicat techniques," *Cem Concr Res*, vol. 39, no. 5, pp. 433–439, May 2009, doi: 10.1016/j.cemconres.2009.01.017.

[83] Y. Zuo, M. Nedeljković, and G. Ye, "Pore solution composition of alkali-activated slag/fly ash pastes," *Cem Concr Res*, vol. 115, pp. 230–250, Jan. 2019, doi: 10.1016/j.cemconres.2018.10.010.

[84] "NEN-EN-ISO 14040_2006 en", Accessed: Apr. 11, 2025. [Online]. Available: https://www.nen.nl/nen-en-iso-14040-2006-en-109085

[85] X. Ouyang, Y. Ma, Z. Liu, J. Liang, and G. Ye, "Effect of the sodium silicate modulus and slag content on fresh and hardened properties of alkali-activated fly ash/slag," *Minerals*, vol. 10, no. 1, Jan. 2020, doi: 10.3390/min10010015.

[86] T. Luukkonen *et al.*, "Influence of sodium silicate powder silica modulus for mechanical and chemical properties of dry-mix alkali-activated slag mortar," *Constr Build Mater*, vol. 233, Feb. 2020, doi: 10.1016/j.conbuildmat.2019.117354.

[87] H. Wang, H. Wu, Z. Xing, R. Wang, and S. Dai, “The effect of various si/al, na/al molar ratios and free water on micromorphology and macro-strength of metakaolin-based geopolymer,” *Materials*, vol. 14, no. 14, Jul. 2021, doi: 10.3390/ma14143845.

[88] A. A. Aliabdo, A. E. M. Abd Elmoaty, and H. A. Salem, “Effect of water addition, plasticizer and alkaline solution constitution on fly ash based geopolymer concrete performance,” *Constr Build Mater*, vol. 121, pp. 694–703, Sep. 2016, doi: 10.1016/j.conbuildmat.2016.06.062.

[89] A. Sharma, S. Gupta, M. Noman Husain, and S. Chaudhary, “Factors affecting the rheology of cement-based composites: A review,” *Journal of the American Ceramic Society*, vol. 108, no. 6, Feb. 2025, doi: 10.1111/jace.20429.

[90] B. Panda, C. Unluer, and M. J. Tan, “Extrusion and rheology characterization of geopolymer nanocomposites used in 3D printing,” *Compos B Eng*, vol. 176, Nov. 2019, doi: 10.1016/j.compositesb.2019.107290.

[91] X. Dai, S. Aydin, M. Y. Yardimci, K. Lesage, and G. De Schutter, “Early age reaction, rheological properties and pore solution chemistry of NaOH-activated slag mixtures,” *Cem Concr Compos*, vol. 133, Oct. 2022, doi: 10.1016/j.cemconcomp.2022.104715.

[92] H. Wan, L. Yuan, and Y. Zhang, “Insight Into the Leaching of Sodium Alumino-Silicate Hydrate (N-A-S-H) Gel: A Molecular Dynamics Study,” *Front Mater*, vol. 7, Mar. 2020, doi: 10.3389/fmats.2020.00056.

[93] B. Chen and G. Ye, “The role of water-treated municipal solid waste incineration (MSWI) bottom ash in microstructure formation and strength development of blended cement pastes,” *Cem Concr Res*, vol. 178, Apr. 2024, doi: 10.1016/j.cemconres.2024.107440.

[94] Chen, “Utilization of mswi bottom ash as a mineral resource for low-carbon construction materials Quality-upgrade treatments, mix design method, and microstructure analysis,” Delft University of Technology, 2023. doi: 10.4233/uuid:0793986f-b875-4693-a0f9-568978f2d632.

[95] X. Dai, S. Aydin, M. Yucel Yardimci, and G. De Schutter, “Fresh and hardened state properties, reaction kinetics and microstructure of sodium sulfate/sodium hydroxide – Activated slag mixtures,” *Constr Build Mater*, vol. 401, Oct. 2023, doi: 10.1016/j.conbuildmat.2023.132943.

[96] J. Xing, Y. Zhao, J. Qiu, and X. Sun, “Microstructural and mechanical properties of alkali activated materials from two types of blast furnace slags,” *Materials*, vol. 12, no. 13, Jul. 2019, doi: 10.3390/ma12132089.

[97] S. A. Bernal *et al.*, “MgO content of slag controls phase evolution and structural changes induced by accelerated carbonation in alkali-activated binders,” *Cem Concr Res*, vol. 57, pp. 33–43, Mar. 2014, doi: 10.1016/j.cemconres.2013.12.003.

[98] Y. Zuo, M. Nedeljković, and G. Ye, “Coupled thermodynamic modelling and experimental study of sodium hydroxide activated slag,” *Constr Build Mater*, vol. 188, pp. 262–279, Nov. 2018, doi: 10.1016/j.conbuildmat.2018.08.087.

[99] I. Ismail, S. A. Bernal, J. L. Provis, R. San Nicolas, S. Hamdan, and J. S. J. Van Deventer, “Modification of phase evolution in alkali-activated blast furnace slag by the incorporation of fly ash,” *Cem Concr Compos*, vol. 45, pp. 125–135, 2014, doi: 10.1016/j.cemconcomp.2013.09.006.

[100] Z. Liu, D. wang Zhang, L. LI, J. xiang Wang, N. ning Shao, and D. min Wang, “Microstructure and phase evolution of alkali-activated steel slag during early age,” *Constr Build Mater*, vol. 204, pp. 158–165, Apr. 2019, doi: 10.1016/j.conbuildmat.2019.01.213.

[101] M. F. Zawrah, R. A. Gado, and R. M. Khattab, “Optimization of slag content and properties improvement of metakaolin-slag geopolymer mixes,” *Open Materials Science Journal*, vol. 12, pp. 40–57, 2018, doi: 10.2174/1874088X01812010040.

[102] M. Król, P. Rożek, D. Chlebda, and W. Mozgawa, “Influence of alkali metal cations/type of activator on the structure of alkali-activated fly ash – ATR-FTIR studies,” *Spectrochim*

Acta A Mol Biomol Spectrosc, vol. 198, pp. 33–37, Jun. 2018, doi: 10.1016/j.saa.2018.02.067.

[103] S. K. Tripathy, J. Dasu, Y. R. Murthy, G. Kapure, A. R. Pal, and L. O. Filippov, “Utilisation perspective on water quenched and air-cooled blast furnace slags,” *J Clean Prod*, vol. 262, Jul. 2020, doi: 10.1016/j.jclepro.2020.121354.

[104] S. Dai, H. Wang, S. An, and L. Yuan, “Mechanical Properties and Microstructural Characterization of Metakaolin Geopolymers Based on Orthogonal Tests,” *Materials*, vol. 15, no. 8, Apr. 2022, doi: 10.3390/ma15082957.

[105] Z. Su, Z. Liu, H. Wang, S. Xu, D. Wang, and F. Han, “Reaction kinetics, microstructure and phase evolution of alkali-activated Si-Mn slag during early age,” *Constr Build Mater*, vol. 333, May 2022, doi: 10.1016/j.conbuildmat.2022.127437.

[106] M. Palacios and F. Puertas, “Effect of carbonation on alkali-activated slag paste,” *Journal of the American Ceramic Society*, vol. 89, no. 10, pp. 3211–3221, Oct. 2006, doi: 10.1111/j.1551-2916.2006.01214.x.

[107] Z. Zhang, H. Wang, and J. L. Provis, “Quantitative study of the reactivity of fly ash in geopolymerization by ftir,” *J Sustain Cem Based Mater*, vol. 1, no. 4, pp. 154–166, 2012, doi: 10.1080/21650373.2012.752620.

[108] F. Sha, H. Li, D. Pan, H. Liu, and X. Zhang, “Development of steel slag composite grouts for underground engineering,” *Journal of Materials Research and Technology*, vol. 9, no. 3, pp. 2793–2809, 2020, doi: 10.1016/j.jmrt.2020.01.014.

[109] A. A. Hoyos-Montilla, F. Puertas, J. Molina Mosquera, and J. I. Tobón, “Infrared spectra experimental analyses on alkali-activated fly ash-based binders,” *Spectrochim Acta A Mol Biomol Spectrosc*, vol. 269, Mar. 2022, doi: 10.1016/j.saa.2021.120698.

[110] J. Lin, Y. Zhang, and Z. Yang, “A Review of Recent Advances in Alkali-activated Materials from Silica-rich Wastes Derived Sodium Silicate Activators,” *Journal of Advanced Concrete Technology*, vol. 21, no. 3, pp. 189–203, Mar. 2023, doi: 10.3151/JACT.21.189.

[111] B. Yuan, Q. L. Yu, and H. J. H. Brouwers, “Time-dependent characterization of Na2CO3 activated slag,” *Cem Concr Compos*, vol. 84, pp. 188–197, Nov. 2017, doi: 10.1016/j.cemconcomp.2017.09.005.

[112] G. H. A. Ting, Y. W. D. Tay, and M. J. Tan, “Experimental measurement on the effects of recycled glass cullets as aggregates for construction 3D printing,” *J Clean Prod*, vol. 300, Jun. 2021, doi: 10.1016/j.jclepro.2021.126919.

[113] “NIBE EPD.” Accessed: Apr. 11, 2025. [Online]. Available: https://www.nibe-sustainability- experts.com/nl/epd-tool

[114] E. Benelux, “Environmental Product Declaration Eco2cem GGBS.” [Online]. Available: www.mrpi.nl

[115] “Environmental Product Declaration Coal fly ash (v2).” [Online]. Available: www.mrpi.nl

[116] “Environmental Product Declaration CEM I 42,5 N.” [Online]. Available: www.mrpi.nl

[117] “Environmental Product Declaration Ferroglobe Silica Fume.” [Online]. Available: www.astm.org